ANALYSIS OF DEEP DRAWING PROCESS BY USING HYPO- AND HYPERELASTIC BASED PLASTICITY MODELS

A THESIS SUBMITTED TO
THE GRADUATE SCHOOL OF NATURAL AND APPLIED SCIENCES
OF
MIDDLE EAST TECHNICAL UNIVERSITY

BY

İLKE BARIŞ CANBAKAN

IN PARTIAL FULFILLMENT OF THE REQUIREMENTS
FOR
THE DEGREE OF MASTER OF SCIENCE
IN
MECHANICAL ENGINEERING

AUGUST 2019

Approval of the thesis:

ANALYSIS OF DEEP DRAWING PROCESS BY USING HYPO- AND HYPERELASTIC BASED PLASTICITY MODELS

submitted by **İLKE BARIŞ CANBAKAN** in partial fulfillment of the requirements for the degree of **Master of Science in Mechanical Engineering Department, Middle East Technical University** by,

Prof. Dr. Halil Kalıpçılar
Dean, Graduate School of **Natural and Applied Sciences**

Prof. Dr. Sahir Arıkan
Head of Department, **Mechanical Engineering**

Prof. Dr. Haluk Darendeliler
Supervisor, **Mechanical Engineering, METU**

Examining Committee Members:

Prof. Dr. Süha Oral
Mechanical Engineering, METU

Prof. Dr. Haluk Darendeliler
Mechanical Engineering, METU

Prof. Dr. Suat Kadıoğlu
Mechanical Engineering, METU

Prof. Dr. Can Çoğun
Mechanical Engineering, Çankaya University

Assist. Prof. Dr. Orkun Özşahin
Mechanical Engineering, METU

Date: 06.08.2019

I hereby declare that all information in this document has been obtained and presented in accordance with academic rules and ethical conduct. I also declare that, as required by these rules and conduct, I have fully cited and referenced all material and results that are not original to this work.

Name, Surname: İlke Barış Canbakan

Signature:

ABSTRACT

ANALYSIS OF DEEP DRAWING PROCESS BY USING HYPO- AND HYPERELASTIC BASED PLASTICITY MODELS

Canbakan, İlke Barış
Master of Science, Mechanical Engineering
Supervisor: Prof. Dr. Haluk Darendeliler

August 2019, 103 pages

Estimation of formability is important for sheet metal forming in order to get desired results with minimum amount of experiments. This can be achieved by having a proper constitutive model for the material that can estimate the behavior accurately. In the context of this thesis, two inherently different type of constitutive models, namely hypoelastic and hyperelastic based plasticity models are compared. For both formulations, three different stress-strain relations were created having non-linear isotropic hardening, non-linear kinematic hardening and a combined non-linear isotropic and kinematic hardening adding up to total of six material models. Von Mises Yield criterion was utilized in all six of these models and they were implemented to a commercial finite element program as user material subroutine. Comparison is made by three different deep drawing simulations which are cylindrical, square and round bottom cup drawings.

Keywords: Hyperelastic, Hypoelastic, Plasticity, Finite Element

ÖZ

DERİN ÇEKME İŞLEMİNİN HİPO- VE HİPERELASTİK TEMELLİ PLASTİSİTE MODELLERİ KULLANILARAK ANALİZİ

Canbakan, İlke Barış
Yüksek Lisans, Makina Mühendisliği
Tez Danışmanı: Prof. Dr. Haluk Darendeliler

Ağustos 2019, 103 sayfa

Bir sac malzemenin şekillendirilebilirliğinin önceden kestirilebilmesi arzu edilen sonuçların deneme üretimi sayısını en aza indirilerek elde edilmesini sağlar. Bu durum malzemenin davranışını doğru bir şekilde ifade eden bir bünye modeli ile elde edilebilir. Bu tezde, farklı şekilde geliştirilen iki bünye modeli; hipoelastik ve hiperelastik bazlı plastisite modelleri karşılaştırılmıştır. İki temel formülasyon için de, gerilme-gerinim denklemleri lineer olmayan izotropik pekleşme, lineer olmayan kinematik pekleşme ve lineer olmayan birleşik izotropik ve kinematik pekleşme için elde edilerek toplamda altı farklı model oluşturulmuştur. Bütün modellerde von Mises akma kriteri kullanılmıştır ve modeller kullanıcı malzeme altprogramı aracılığı ile ticari bir sonlu elemanlar programına eklenmiştir. Karşılaştırma silindirik, kare ve yarı küresel olmak üzere üç farklı derin çekme işleminin simüle edilmesi ile yapılmıştır.

Anahtar Kelimeler: Hiperelastik, Hipoelastik, Plastisite, Sonlu Eleman

To my beloved family

ACKNOWLEDGEMENTS

First of all, I would like to mention my sincerest thanks to my supervisor Haluk Darendeliler, for his guidance, suggestions and will to share his knowledge without hesitation. Also, I cannot deny the help and support I got from my ever so invaluable family, Cansu Canbakan, Sema Canbakan and Başol Canbakan.

TABLE OF CONTENTS

CHAPTERS

LIST OF TABLES

TABLES

LIST OF FIGURES

FIGURES

CHAPTER 1

INTRODUCTION

1.1. Background and Motivation

Plastic (permanent) deformation occurs in materials after their yield stress is exceeded. This phenomenon is common in industrial forming operations such as deep drawing and leads to large deformations. To better predict material behavior during the plastic deformation, use of a proper constitutive relation is crucial. There are extensive number of constitutive models in the literature for large deformation ranges such as in the case of these elastoplastic deformations. While these elastoplastic models boil down to same expressions in the small strain regime, they are founded on completely different plastic flow descriptions. Two of the more popular of these models are named hypo- and hyperelastic based plasticity models.

Hypoelastic based approach is the earliest and most common approach when it comes to large deformation analysis. It is based on the assumption of additive split of rate of deformation tensor into elastic and plastic parts. This additive split first suggested by Hill [1, 2] implicitly and then it is stated in a paper by Prager [3]. Its implementation on numerical analysis is pioneered by Hibbitt [4] followed the need of incrementally objective integration algorithms such as the popular Hughes-Winget algorithm [5]. Hypoelastic based plasticity models exhibit energy dissipation issues which leads to residual stresses in elastic cyclic shear loading. This problem lead to development of hyperelastic-plastic material models.

Hyperelastic based plasticity models are formed with assumption of multiplicative split of deformation gradient into elastic and plastic parts which is first suggested by a multitude of researchers including Eckart [6], Lee and Liu [7] and further conceptualized by Freund [8], Rice [9]. Aforementioned problems with hypoelastic based models do not emerge with hyperelastic-based models, since stress is obtained directly from a free-energy potential. Its implementation as a numerical algorithmic method is first suggested by Simo [10] and its use has been widened since. Nowadays its implementation on anisotropic materials has been accomplished as well i.e. Vladimirov [11,12]

1.2. Objective of the Thesis

Better prediction of outcomes of the industrial forming operations such as deep drawing is key in reducing scrap materials and producing products that are close to perfect. For this purpose, usage of a proper constitutive model gains utmost importance. Keeping that in mind, the thesis aims to compare two inherently different types of plasticity models being hypoelastic based and hyperelastic based models and give a conclusion about their applicability to industrial forming operations.

1.3. Scope of the Thesis

The thesis compares isotropic hypo- and hyperelastic based plasticity models in their application to a variety of deep drawing processes. The models have three variants for isotropic hardening, kinematic hardening and combined isotropic and kinematic hardening adding up to total of six models. The models use Von Mises yield criterion with non-linear kinematic hardening of Armstrong-Frederick type [13] and isotropic hardening of Voce type [14]. Material models were implemented to a commercial finite element software by user material subroutine.

Verification of the models is done first, by comparing obtained results to Brepols et al.’s [15] cylindrical cup drawing results using DP600 sheet metal properties. Then using data for SS304 and DKP6112 three additional deep drawing operations are simulated, cylindrical, square and round bottom cup drawing. Thickness strain distributions obtained from these simulations are compared.

1.4. Outline of the Thesis

The thesis is composed of seven chapters. First chapter intends to give brief information and background knowledge to the reader about hypoelastic and hyperelastic plastic materials, as well as describing the aim of the thesis. Second chapter focuses on giving information about work done previously on the subjects that has similarities with the one in the thesis. Third chapter is where theoretical background of the material models implemented is given. In fourth chapter, brief information about finite element method used in the thesis is given and models formed in commercial finite element analysis program is explained. Chapter five is composed to give information about materials and determination of the material constants that were used in material models discussed in chapter four. Chapter six contains all results of the simulations done using the mentioned material models and after that chapter seven mentions concluding remarks and future work to be done on the subject of the thesis. One appendix is present in the thesis. It gives information about Newton's method that is used in finding the unknown update variables in the material models implemented.

CHAPTER 2

LITERATURE SURVEY

This part of the thesis is composed to give information about previous work done related to the thesis subject. Although there is substantial literature available on comparison of hypo- and hyperelastic based plasticity models on its theoretical aspect (i.e. Xiao [16]), there are far less examples on comparison of the models for their finite element simulation performance. Some work done on numerical implementation of these material models into finite element simulations are summarized in this section. Since hypoelastic based materials are much more common and they form the foundation of many commercial finite element programs for large deformations, this section focuses on work done on comparison of hypoelastic and hyperelastic based models and work done on implementation of only hyperelastic based models.

2.1. Comparison of Hypoelastic and Hyperelastic Based Plasticity Models

As an example of comparison of hyperelastic and hypoelastic based plasticity models article by Chatti [17] can be given. In the paper a comparison of a hypoelastic based plastic material referred to as hypoelastoplastic (HEP) to hyperelastic based plastic material which is stated as elastoplastic (EP) is made in terms of their springback predictions. Both materials were subjected to a shear test in which HEP material came out to show oscillatory behavior for stress and strain for substantial amounts of loading. Next a bending simulation is performed. No substantial differences are found in the results, but EP material lead to superior computational time, around one fourth of that of HEP material. Lastly, a thermoforming operation is simulated and quite different results (up to 50%) for material thickness are found especially in the area where there is high amount of plastic deformation. It is concluded in paper that EP materials require less computational time and present more accurate results compared to HEP materials.

In the work of Brepols et al [15], general comparison of isotropic hyperelastic and hypoelastic based plasticity models is made using von Mises yield criterion, Armstrong-Frederick type kinematic hardening [13], and Voce type isotropic hardening [14] for both cases. The implementation of material models to ABAQUS is done using Umat interface. For hypoelastic model three different sub-models for three different objective stress rates are compared. These objective stress rates namely are Jaumann [18], Green-Naghdi [19] and logarithmic stress [20] rates. For hyperelastic model Neo-Hookean type energy function is utilized. In the work, comparison of the models regarding cyclic shear loading using one element model and regarding some industrial forming operations are presented. For cyclic loading even though the material model is only elastic there are residual strain values obtained for Jaumann and Green-Naghdi objective stress rates which is expected since these rates does not utilize a potential function for energy conservation. Three different industrial forming operations are compared also in the paper. These are cup drawing, draw bending of a sheet metal strip and thermoforming. Even though plastic deformations in these operations are very high, results came out to be very close for each material model which concludes that usage of hypoelastic or hyperlastic models for defining metal materials in industrial forming operations does create much difference.

In the work of Careglio et al. [21] vicoplastic hypoelastic and vicoplastic hyperelastic materials are compared. The hypoelastic based model is proposed by Ponthot [22] and the hyperelastic based model is proposed by Garcia Garino et al. [23]. Three different simulations tests with different viscoplasticity parameters from purely elastic to elastoplastic is compared resulting in very good agreement of both models in many of the cases.

2.2. Hyperelastic Based Plasticity Models

In the work of Vladimirov et al. [24], isotropic hyperelastic plasticity model is used to predict springback of DP600 sheet metal strips in draw bending operation. The material constants are determined through fitting material parameters to uniaxial test data for only isotropic hardening, only kinematic hardening and combined hardening models. Different parameters are found for different thicknesses of the specimen. Then comparison between these models (isotropic, kinematic and combined) are conducted for 1mm thick specimen. Combined hardening model came out to be the best model in prediction of springback by quite a margin. After this point using combined hardening only, more simulations were performed for combination of different values of bending radius (5mm, 10mm, 15mm) and sheet thickness (0.6mm, 1mm, 2mm). Results came out to be pretty close to experimental data for most of the cases. Simulations of S-rail forming and thermoforming operations were also performed and compared with the experimental results which suggests excellent prediction of springback by the hyperelastic-plastic combined hardening model.

In the work of Vladimirov et al. [25] again a hyperelastic plastic material model using classical rheological Armstrong-Frederick [13] type kinematic hardening and Voce [14] type isotropic hardening is utilized. The model is implemented to ABAQUS through Umat. Different integration algorithm methods namely classical backward Euler [26, 27, 28], modified backward Euler, second modified backward Euler and exponential map algorithm are compared. Firstly, comparison of models in terms of convergence efficiency is performed in which classical backward Euler algorithm showed results that are quite inaccurate when time increment is increased. Exponential map algorithm was the most accurate one with increased time steps. Further, a comparison of springback estimation on draw bending of sheet metal strip is presented with using different algorithms and again exponential map algorithm came out to be the best integration algorithm to predict the springback.

Another work of Vladimirov et al. [11] is composed of derivation of an anisotropic model for a hyperelastic based model. Again, kinematic hardening model used in derivation is Armstrong-Frederick [13] type, whereas, yield criterion utilized is of Hill-48 type. Derived mathematical model is implemented to ABAQUS through Umat subroutine. Three different forming processes namely cup drawing, square cup drawing and s-rail forming are simulated and the results are compared with experimental data. Good correlation between experiments and proposed material model is found.

Vladimirov et al. [29] this time proposed a ductile damage model for hyperelastic anisotropic plastic material that uses same combined hardening model as in their previous works. The model is implemented to ABAQUS and LS-DYNA through user material subroutine Umat. Finite element simulation of Nakazima test [30] is performed on different types of aluminum alloys and results are compared to experimental tests. Finite element results show fair agreement of model with experimental data in prediction of rupture failure.

Study of Wallin and Ristinmaa [31], presents a hyperelastic based kinematic hardening model accompanied by von Mises type yield function. In the model plastic velocity gradient is assumed to split into dissipative and non-dissipative parts additively and non-dissipative quantities are introduced in the model which are considered to be material constants. Time integration is done by exponential update equations for different forms of deformation gradient associated with plastic flow and kinematic hardening. As numerical examples, extension of a thin walled cylinder under torsion, a notched specimen under cyclic loading and unsymmetric membrane (Cook's) subjected to cyclic loading are considered. In conclusion, effect of non-dissipative quantities on the Cook's membrane came out to be insignificant whereas, integration algorithm used is commented to be a robust one.

Recently, Sanz et al [32] introduced a hyperelastic based anisotropic mixed hardening model that uses logarithmic elastic strains with corrector instead of common plastic ones in their evolution equations. Kinematic hardening used in the constitutive equations differs from classical kinematic hardening theories that requires separate integration of back stress tensor. This approach further explained by Zhang et al. [33]. The proposed model is implemented to commercial finite element program ADINA. Four different finite element simulations performed (drawing of a thin circular flange, cylindrical cup drawing, square cup drawing and s-rail forming). The results are compared to the results of other proposed anisotropic plasticity models (i.e. Vladimirov [11]). As a result, it is concluded that the model in the paper is comparable to other models available, producing similar results and is suitable for usage in simulations of industrial forming operations.

CHAPTER 3

THEROETICAL BACKGROUND

3.1. Elasticity

Numerous different models were proposed for modeling elastic deformation of materials. Hypoelastic and hyperelastic models are among these and they are commonly employed when deformations are large. This section gives information about fundamentals of these two approaches.

3.1.1. Hypoelasticity

In continuum mechanics constitutive equations are needed to be frame indifferent [34]. An objective rate of any tensor must be used in constitutive equations to satisfy this need. This is true for stress as well. There arise hypoelasticity [35].

It is first suggested by Truesdell and Rivlin that this objective rate for stress is dependent on current stress state and rate of deformation.

$$\check{\boldsymbol{\tau}} = f(\boldsymbol{\tau}, \boldsymbol{D}) \tag{3.1}$$

where $\check{\boldsymbol{\tau}}$ is an objective rate of Kirchhoff stress $\boldsymbol{\tau}$ and $\boldsymbol{D}$ is the rate of deformation tensor. Considering elastic isotropic materials particularly, and assuming elastic properties of the material remaining unchanged throughout the deformation process constitutive relation for a hypoelastic material can be formed as follows [36]:

$$\check{\boldsymbol{\tau}} = \lambda \, tr(\boldsymbol{D})\boldsymbol{I} + 2\mu\boldsymbol{D} \tag{3.2}$$

In this equation, λ and μ are Lame parameters. In a general form objective stress rate is defined as:

$$\check{\boldsymbol{\tau}} = \dot{\boldsymbol{\tau}} - \boldsymbol{\Omega}\boldsymbol{\tau} + \boldsymbol{\tau}\boldsymbol{\Omega} \tag{3.3}$$

$\boldsymbol{\Omega}$ here is called the spin tensor and stress rate takes a different name for different forms of $\boldsymbol{\Omega}$. Two of the more common forms used as spin tensor are Jaumann rate [18] and Green-Naghdi rate [19], given by following equations, respectively.

$$\boldsymbol{\Omega} = \mathbf{w} \tag{3.4}$$

$$\boldsymbol{\Omega} = \dot{\boldsymbol{R}}\boldsymbol{R}^{\boldsymbol{T}} \tag{3.5}$$

where $\mathbf{w}$ is skew-symmetric part of the velocity gradient and $\boldsymbol{R}$ is rotation tensor from polar decomposition.

3.1.2. Hyperelasticity

When work done on the material by the stresses induced is only dependent on initial and final states of the material (path independent), material is termed hyperelastic or Green elastic. This leads to existence of a potential function, ψ. This function is called as “stored strain energy function” or “elastic potential” [37]. It relates deformation to stress through its derivative with respect to deformation gradient or any other deformation measure. In general:

$$\boldsymbol{P} = \frac{\partial \psi}{\partial \boldsymbol{F}} \tag{3.6}$$

Here $\boldsymbol{P}$ is first Piola-Kirchhoff stress tensor. Elastic potential ψ should remain unchanged during a rigid body motion, but $\boldsymbol{F}$ is dependent on the rigid body rotation tensor $\boldsymbol{R}$ through polar decomposition:

$$\boldsymbol{F} = \boldsymbol{R}\boldsymbol{U} = \boldsymbol{V}\boldsymbol{R} \tag{3.7}$$

This shows ψ should only be a function of stretch $\boldsymbol{U}$ or $\boldsymbol{V}$. For this reason, most often elastic potential function is described as:

$$\psi = \psi(\boldsymbol{F}(\boldsymbol{X}), \boldsymbol{X}) = \psi(\boldsymbol{C}(\boldsymbol{X}), \boldsymbol{X}) \tag{3.8}$$

where

$$\boldsymbol{C} = \boldsymbol{F}^T\boldsymbol{F} = \boldsymbol{U}^2 \tag{3.9}$$

and $\boldsymbol{X}$ is position vector in initial configuration. Using this definition second Piola-Kirchhoff stress tensor ($\boldsymbol{S}$) can be defined as:

$$\boldsymbol{S} = 2\frac{\partial \psi}{\partial \boldsymbol{C}} \tag{3.10}$$

These are the most general equations for hyperelastic materials. When isotropic materials are of concern, ψ is needed to be independent of direction. This brings forth the requirement of ψ to be function of only invariants of $\boldsymbol{C}$ noted as, $I_{\boldsymbol{C}}, II_{\boldsymbol{C}}, III_{\boldsymbol{C}}$. These invariants are defined as:

$$I_{\boldsymbol{C}} = tr(\boldsymbol{C}) = \boldsymbol{C} : \boldsymbol{I} \tag{3.11}$$

$$II_{\boldsymbol{C}} = \boldsymbol{C} : \boldsymbol{C} \tag{3.12}$$

$$III_{\boldsymbol{C}} = \det(\boldsymbol{C}) = J^2 \tag{3.13}$$

Then $\boldsymbol{S}$ can be defined through partial derivatives of these invariants as:

$$\boldsymbol{S} = 2\frac{\partial \psi}{\partial I_{\boldsymbol{C}}}\frac{\partial I_{\boldsymbol{C}}}{\partial \boldsymbol{C}} + 2\frac{\partial \psi}{\partial II_{\boldsymbol{C}}}\frac{\partial II_{\boldsymbol{C}}}{\partial \boldsymbol{C}} + 2\frac{\partial \psi}{\partial III_{\boldsymbol{C}}}\frac{\partial III_{\boldsymbol{C}}}{\partial \boldsymbol{C}} \tag{3.14}$$

and derivatives of invariants are found to be as follows:

$$\frac{\partial I_{\boldsymbol{C}}}{\partial \boldsymbol{C}} = \boldsymbol{I} \tag{3.15}$$

$$\frac{\partial II_{\boldsymbol{C}}}{\partial \boldsymbol{C}} = 2\boldsymbol{C} \tag{3.16}$$

$$\frac{\partial III_{\boldsymbol{C}}}{\partial \boldsymbol{C}} = J^2\boldsymbol{C}^{-1} \tag{3.17}$$

These formulae lead to

$$\boldsymbol{S} = 2\psi_I\boldsymbol{I} + 4\psi_{II}\boldsymbol{C} + 2J^2\psi_{III}\boldsymbol{C}^{-1} \tag{3.18}$$

where $\psi_I = \partial\psi/\partial I_{\boldsymbol{C}}$, $\psi_{II} = \partial\psi/\partial II_{\boldsymbol{C}}$, $\psi_{III} = \partial\psi/\partial III_{\boldsymbol{C}}$. Lastly, for the spatial description, $\boldsymbol{S}$ will be pushed forward for getting the expression for Cauchy stress $\boldsymbol{\sigma}$ using

$$\boldsymbol{\sigma} = J^{-1}\boldsymbol{F}\boldsymbol{S}\boldsymbol{F}^{\boldsymbol{T}} \tag{3.19}$$

Hyperelastic material used for the simulations in the thesis was of Neo-Hookean type for which strain energy density function is defined as:

$$\begin{aligned}\psi &= \frac{\mu}{2}[tr(\boldsymbol{C}) - 3] - \mu\, ln\left[\sqrt{det(\boldsymbol{C})}\right] \\ &+ \frac{\lambda}{4}\left\{det(\boldsymbol{C}) - 1 - 2\ln\left[\sqrt{det(\boldsymbol{C})}\right]\right\}\end{aligned} \tag{3.20}$$

which leads through 3.10 to

$$\boldsymbol{S} = \mu(\boldsymbol{I} - \boldsymbol{C}^{-1}) + \frac{\lambda}{2}[\det(\boldsymbol{C}) - 1]\boldsymbol{C}^{-1} \tag{3.21}$$

3.2. Plasticity

In this section constitutive models for describing plastic deformation for both hypoelastic and hyperelastic based models are explained.

3.2.1. Yield Condition

Von Mises yield criterion in combination with isotropic, kinematic and combined hardening is used for material models that are used in the context of this thesis.

Von Mises yield criterion is based on distortion energy induced in the material due to deformation. It suggests yielding of the material occurs if distortion energy per unit volume of the material exceeds that of a tensile test specimen of that material. [38]

The condition is described by the equation:

$$\Phi = \sqrt{J_2'} - \sigma_Y = 0 \tag{3.22}$$

where J_2' is the second invariant of the deviatoric stress tensor and σ_Y is yield stress of the material, and Φ is the yield equation. J_2' is defined as

$$\begin{aligned}J_2' = \frac{1}{6}&[(\sigma_{11} - \sigma_{22})^2 + (\sigma_{11} - \sigma_{33})^2 + (\sigma_{22} - \sigma_{33})^2] \\ &+ (\sigma_{12}^2 + \sigma_{31}^2 + \sigma_{23}^2)\end{aligned} \tag{3.23}$$

Yield surfaces for 3-D and 2-D cases are shown in figures 3.1 and 3.2, respectively.

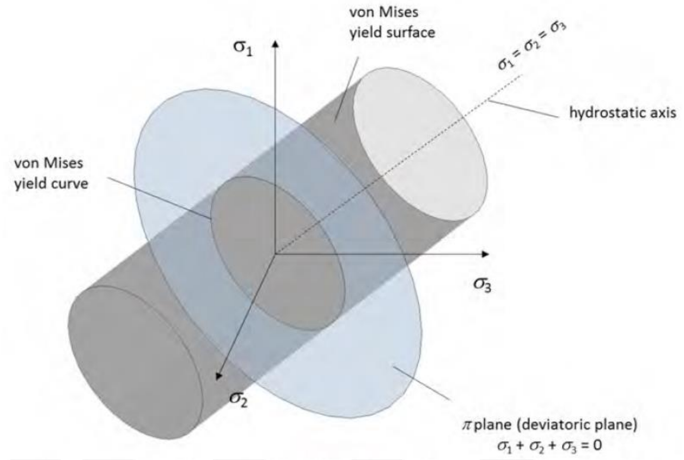

Figure 3.1 Von Mises yield surface in 3-D [39]

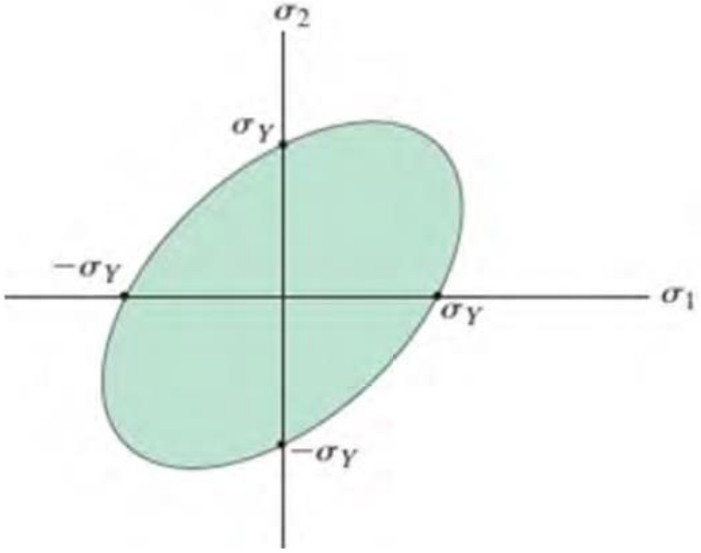

Figure 3.2. Von Mises yield surface in 2-D [39]

3.2.2. Hypoelastic Based Plasticity

In hypoelastic based plasticity, rate of deformation tensor $\boldsymbol{D}$ is assumed to be additively decomposable into elastic and plastic parts

$$\boldsymbol{D} = \boldsymbol{D}^e + \boldsymbol{D}^p \tag{3.24}$$

This additive separation of rate of deformation tensor is starting point of classical theories of elastoplasticity for finite deformations. It is an extension of additive separation of elastic and plastic strains that is applicable in small strain regime. [16]

$$\boldsymbol{\varepsilon} = \boldsymbol{\varepsilon}^e + \boldsymbol{\varepsilon}^p \tag{3.25}$$

This additive decomposition is backed up by additive decomposition of work increment into elastic (reversible) and inelastic (irreversible) parts. [40]

Then stress can be formulated in a corotational frame by the following

$$\check{\boldsymbol{\tau}} = \ \boldsymbol{\mathcal{C}} : \boldsymbol{D}^e \tag{3.26}$$

Leading to

$$\check{\boldsymbol{\tau}} = \ \boldsymbol{\mathcal{C}} : (\ \boldsymbol{D} - \boldsymbol{D}^p) \tag{3.27}$$

Here $\mathcal{C}$ is fourth order elastic modulus tensor [41]. ":" operation is called double contraction and between a fourth (B) and second order tensor (C). For example, Equation 3.26 can be shown in indicial notation as $\check{\boldsymbol{\tau}}_{ij} = \mathcal{C}_{ijkl}\boldsymbol{D}^{\boldsymbol{e}}_{kl}$.

Yield condition requires:

$$\Phi = \Phi(\boldsymbol{\tau}, \alpha) = 0 \tag{3.28}$$

where α is any other variable that Φ can be dependent on. Using the flow rule described below $\boldsymbol{D}^p$ can be found.

$$\boldsymbol{D}^p = \dot{\gamma}\frac{\partial\Phi}{\partial\boldsymbol{\tau}} \tag{3.29}$$

In this equation $\dot{\gamma}$ is the plastic multiplier. Second part of the equation involving partial derivative of yield function Φ with respect to stress is true for associative flow rules. In other flow rules Φ should be replaced with an appropriate plastic potential function.

Together with these equations Kuhn-Tucker conditions which are shown below should be satisfied to define the material's plastic deformation.

$$\dot{\gamma} > 0, \qquad \Phi \leq 0, \qquad \dot{\gamma}\Phi = 0 \tag{3.30}$$

In the aforementioned equations, commonly α is effective accumulated plastic strain and $\dot{\gamma}$ is defined as:

$$\dot{\gamma} = \dot{\alpha} = \dot{\bar{\varepsilon}}^{p} \tag{3.31}$$

The effective plastic strain denoted as $\bar{\varepsilon}_p$ is defined as:

$$\bar{\varepsilon}^{p} = \int \dot{\bar{\varepsilon}}^{p} \tag{3.32}$$

$$\dot{\bar{\varepsilon}}^{p} = \sqrt{\frac{2}{3}\dot{\boldsymbol{\varepsilon}}^{p} : \dot{\boldsymbol{\varepsilon}}^{p}} \tag{3.33}$$

3.2.2.1. Hypoelastic Isotropic Hardening Model

For hypoelastic isotropic hardening Voce model is used [14]. The model has the form:

$$\sigma_Y = \sigma_Y^0 + Q\left(1 - e^{-\beta\bar{\varepsilon}^{p}}\right) \tag{3.34}$$

Here Q and β are material parameters to be determined from uniaxial test data of the specimen and σ_Y^0 is the initial yield strength. This formula leads to yield function of von Mises type:

$$\Phi = \sqrt{\frac{3}{2}}|\boldsymbol{\tau}'| - \left[\sigma_Y^0 + Q\left(1 - e^{-\beta\bar{\varepsilon}_{p}}\right)\right] = 0 \tag{3.35}$$

Where $\boldsymbol{\tau}'$ is deviatoric part of the Kirchhoff stress tensor defined in indicial notation as

$$\boldsymbol{\tau}' = \boldsymbol{\tau} - \frac{1}{3}(\tau_{ii}) \tag{3.36}$$

and term $|\boldsymbol{\tau}'|$ defined as

$$|\boldsymbol{\tau}'| = \sqrt{(\boldsymbol{\tau}'):(\boldsymbol{\tau}')^T} \tag{3.37}$$

Double contraction between two second order tensors $\boldsymbol{B}$ and $\boldsymbol{C}$ such as $\boldsymbol{\tau}^D$ is defined in indicial notation to be $A = B_{ij}C_{ij}$, where A is a scalar and, also from using Equation 3.30 plastic flow rule can be specified as:

$$\boldsymbol{D}^p = \dot{\gamma}\frac{\partial\Phi}{\partial\boldsymbol{\tau}} = \dot{\gamma}\sqrt{\frac{3}{2}}\frac{\boldsymbol{\tau}'}{|\boldsymbol{\tau}'|} \tag{3.38}$$

Along with these equations, Equation 3.27 for determination of the stress completes the definition of hypoelastic isotropic hardening model.

3.2.2.2. Hypoelastic Kinematic Hardening Model

For kinematic hardening von Mises yield function is defined as:

$$\Phi = \sqrt{\frac{3}{2}}|\boldsymbol{\tau}' - \boldsymbol{\alpha}| - (\sigma_Y^0) = 0 \tag{3.39}$$

where $\boldsymbol{\alpha}$ is defined as back stress. Again, through Equation 3.30 flow rule is found to be:

$$\boldsymbol{D}^p = \dot{\gamma}\frac{\partial\Phi}{\partial\boldsymbol{\tau}} = \dot{\gamma}\sqrt{\frac{3}{2}}\frac{\boldsymbol{\tau}' - \boldsymbol{\alpha}}{|\boldsymbol{\tau}' - \boldsymbol{\alpha}|} \tag{3.40}$$

Kinematic hardening is defined to be of Armstrong-Frederick type [13]. Update equations for back stress is given by:

$$\breve{\boldsymbol{\alpha}} = \dot{\gamma}\sqrt{\frac{3}{2}}\left(c\frac{\boldsymbol{\tau}' - \boldsymbol{\alpha}}{|\boldsymbol{\tau}' - \boldsymbol{\alpha}|} - b\boldsymbol{\alpha}\right) \tag{3.41}$$

"∨" symbol above $\boldsymbol{\alpha}$ implies that update equation for back stress is also defined in corotational frame. c and b in Equation 3.41 are material constants related to Armstrong-Frederick [13] type kinematic hardening. Again, with the use of Equation 3.27 hypoelastic based kinematic hardening model is fully defined.

3.2.2.3. Hypoelastic Combined Hardening Model

As in the case of isotropic hardening, using Voce [14] model, yield function is found in the form:

$$\Phi = \sqrt{\frac{3}{2}}|\boldsymbol{\tau}' - \boldsymbol{\alpha}| - \left[\sigma_Y^0 + Q\left(1 - e^{-\beta\bar{\varepsilon}^p}\right)\right] = 0 \tag{3.42}$$

Evolution equations for plastic rate of deformation ($\boldsymbol{D}^p$) and that for back stress ($\boldsymbol{X}$) are same as those for kinematic hardening that are given in the Equations 3.40, 3.41 respectively.

Finally, model is completed again with the usage of Equation 3.27 which defines the Kirchhoff stress.

3.2.2.4. Algorithmic Implementation

Stress rate used in the constitutive equation must be objective (satisfied by the use of corotational stress rate) and also constitutive update is needed to be performed on a rotation free frame. To achieve that Equation 3.27 is to be rotated to such a frame by a proper orthogonal rotation matrix denoted here as $\boldsymbol{\Lambda}$ for fixed $\boldsymbol{X}$. $\boldsymbol{\Lambda}$ is defined in terms of any spatial skew symmetric tensor, $\boldsymbol{\Omega}$, that is used in corotational stress formulation [27]

$$\dot{\boldsymbol{\Lambda}} = \boldsymbol{\Omega}\boldsymbol{\Lambda} \tag{3.43}$$

$$\boldsymbol{\Lambda}^T \check{\boldsymbol{\tau}} \boldsymbol{\Lambda} = \boldsymbol{C} : (\boldsymbol{\Lambda}^T \boldsymbol{D} \boldsymbol{\Lambda} - \boldsymbol{\Lambda}^T \boldsymbol{D}^p \boldsymbol{\Lambda}) \tag{3.44}$$

Defining the rotated tensors as:

$$\boldsymbol{\Lambda}^T \boldsymbol{\tau} \boldsymbol{\Lambda} = \tilde{\boldsymbol{\tau}}, \qquad \boldsymbol{\Lambda}^T \boldsymbol{D} \boldsymbol{\Lambda} = \widetilde{\boldsymbol{D}}, \qquad \boldsymbol{\Lambda}^T \boldsymbol{D}^p \boldsymbol{\Lambda} = \widetilde{\boldsymbol{D}}^p \tag{3.45}$$

$\boldsymbol{\Lambda}^T\check{\boldsymbol{\tau}}\boldsymbol{\Lambda}$ in equation is actually $\dot{\tilde{\boldsymbol{\tau}}}$ which can be shown as in the box below

$$\dot{\tilde{\boldsymbol{\tau}}} = \dot{\overline{\boldsymbol{\Lambda}^T\boldsymbol{\tau}\boldsymbol{\Lambda}}} = \dot{\boldsymbol{\Lambda}}^T\boldsymbol{\tau}\boldsymbol{\Lambda} + \boldsymbol{\Lambda}^T\dot{\boldsymbol{\tau}}\boldsymbol{\Lambda} + \boldsymbol{\Lambda}^T\boldsymbol{\tau}\dot{\boldsymbol{\Lambda}} = \boldsymbol{\Lambda}^T\left(\dot{\boldsymbol{\tau}} + \boldsymbol{\Lambda}\dot{\boldsymbol{\Lambda}}^T\boldsymbol{\tau} + \boldsymbol{\tau}\dot{\boldsymbol{\Lambda}}\boldsymbol{\Lambda}^T\right)\boldsymbol{\Lambda} \qquad (3.46)$$

Using 3.3, 3.46 and proper orthogonality of $\boldsymbol{\Omega}$ it can be shown that

$$\boldsymbol{\Lambda}^T\left(\dot{\boldsymbol{\tau}} + \boldsymbol{\Lambda}\dot{\boldsymbol{\Lambda}}^T\boldsymbol{\tau} + \boldsymbol{\tau}\dot{\boldsymbol{\Lambda}}\boldsymbol{\Lambda}^T\right)\boldsymbol{\Lambda} = \boldsymbol{\Lambda}^T(\dot{\boldsymbol{\tau}} - \boldsymbol{\Omega}\boldsymbol{\tau} + \boldsymbol{\tau}\boldsymbol{\Omega})\boldsymbol{\Lambda} = \boldsymbol{\Lambda}^T(\check{\boldsymbol{\tau}})\boldsymbol{\Lambda} \qquad (3.47)$$

So, the following equation is obtained

$$\dot{\tilde{\boldsymbol{\tau}}} = \boldsymbol{\mathcal{C}} : \left(\widetilde{\boldsymbol{D}} - \widetilde{\boldsymbol{D}}^p\right) \qquad (3.48)$$

From now on notation $n+1$ is used for material property for current time step and n for previous time step. Using backward Euler Integration, below equation is reached.

$$\tilde{\boldsymbol{\tau}}_{n+1} = \tilde{\boldsymbol{\tau}}_n + \boldsymbol{\mathcal{C}} : \left(\widetilde{\boldsymbol{D}}_{n+1} - \widetilde{\boldsymbol{D}}^p_{n+1}\right) \qquad (3.49)$$

It should be noted that to rotate $\boldsymbol{\tau}_n$ to rotation free frame the rotation tensor from the previous time step, $\boldsymbol{\Lambda}_n$ should be used. For other tensors in the equation $\boldsymbol{\Lambda}_{n+1}$ should be used.

After constitutive update is performed the properties must be returned back to current configuration, i.e. they should be multiplied from left with $\boldsymbol{\Lambda}_{n+1}$and from right with $\boldsymbol{\Lambda}^T_{n+1}$ which gives

$$\boldsymbol{\tau}_{n+1} = \boldsymbol{\Lambda}_{n+1}\boldsymbol{\Lambda}^T_n\boldsymbol{\tau}_n\boldsymbol{\Lambda}_n\boldsymbol{\Lambda}^T_{n+1} + \boldsymbol{\mathcal{C}} : \boldsymbol{D}_{n+1} - \boldsymbol{\mathcal{C}} : \boldsymbol{D}^p_{n+1} \qquad (3.50)$$

The $\boldsymbol{\Lambda}_{n+1}\boldsymbol{\Lambda}^T_n\boldsymbol{\tau}_n\boldsymbol{\Lambda}_n\boldsymbol{\Lambda}^T_{n+1}$ term that appears in the update equation is already provided at the start of each step as the old stress so in ABAQUS/VUMAT one does not need to account for rigid body motion. The objective stress rate used is the Green-Naghdi rate by default [42].

$\boldsymbol{\Lambda}_{n+1}\boldsymbol{\Lambda}^T_n\boldsymbol{\tau}_n\boldsymbol{\Lambda}_n\boldsymbol{\Lambda}^T_{n+1} + \boldsymbol{\mathcal{C}} : \boldsymbol{D}_{n+1}$ term appearing in the Equation 3.50 is named trial stress. This stress is obtained by assuming $\boldsymbol{D}$ in the step to be purely elastic. It will be shown as $\boldsymbol{\tau}^{trial}_{n+1}$ after this point. This term is then corrected by the term $-\boldsymbol{\mathcal{C}} : \boldsymbol{D}^p_{n+1}$ which makes sure the stress is on the yield surface.

This $\boldsymbol{\tau}^{trial}_{n+1}$ is compared with σ^0_Y at the beginning of the increment. If $\sigma^0_Y \geq \boldsymbol{\tau}^{trial}_{n+1}$ yielding has not occurred and material is within the elastic limit so, $\boldsymbol{\tau}_{n+1} = \boldsymbol{\tau}^{trial}_{n+1}$. If $\sigma^0_Y \geq \boldsymbol{\tau}^{trial}_{n+1}$ is not satisfied it is said that material has yielded and stress has to be corrected to be kept on the yield surface. This is where plastic update equations are used.

Using Equations, 3.40, 3.41, 3.50 for the combined case update equations are obtained as

$$\boldsymbol{\tau}_{n+1} = \boldsymbol{\tau}^{trial}_{n+1} - \boldsymbol{C} : \Delta\gamma \sqrt{\frac{3}{2}} \frac{\boldsymbol{\tau}'_{n+1} - \boldsymbol{\alpha}_{n+1}}{|\boldsymbol{\tau}'_{n+1} - \boldsymbol{\alpha}_{n+1}|} \tag{3.51}$$

where $\Delta\gamma$ is incremental change in plastic multiplier. Similarly starting with Equation 3.41 update equations for back stress are obtained.

$$\boldsymbol{\alpha}_{n+1} = \boldsymbol{\Lambda}_{n+1}\boldsymbol{\Lambda}^T_n\boldsymbol{\alpha}_n\boldsymbol{\Lambda}_n\boldsymbol{\Lambda}^T_{n+1} + \Delta\gamma \sqrt{\frac{3}{2}} \left(c \frac{\boldsymbol{\tau}'_{n+1} - \boldsymbol{\alpha}_{n+1}}{|\boldsymbol{\tau}'_{n+1} - \boldsymbol{\alpha}_{n+1}|} - b\boldsymbol{\alpha}_{n+1} \right) \tag{3.52}$$

For the implementation of the constitutive formulation to ABAQUS/Vumat it can be said that term $\boldsymbol{\Lambda}_{n+1}\boldsymbol{\Lambda}^T_n\boldsymbol{\alpha}_n\boldsymbol{\Lambda}_n\boldsymbol{\Lambda}^T_{n+1}$ is also provided by the program when components of back stress is stored as a state variable. Update equation for equivalent plastic strain:

$$\bar{\varepsilon}^p_{n+1} = \bar{\varepsilon}^p_n + \Delta\gamma \tag{3.53}$$

and finally yield equation

$$\Phi = \sqrt{\frac{3}{2}} |\boldsymbol{\tau}'_{n+1} - \boldsymbol{\alpha}_{n+1}| - \left(\sigma^0_Y + Q \left(1 - e^{-\beta \bar{\varepsilon}^p_{n+1}} \right) \right) = 0 \tag{3.54}$$

These equations complete the definition of hypoelastic-plastic combined hardening model. Specifying $\bar{\varepsilon}^p_{n+1}$ to be the dependent variable and six elements of $\boldsymbol{\tau}(\tau_{11}, \tau_{22}, \tau_{33}, \tau_{12}, \tau_{23}, \tau_{31})$, six elements of $\boldsymbol{\alpha}(\alpha_{11}, \alpha_{22}, \alpha_{33}, \alpha_{12}, \alpha_{23}, \alpha_{31})$ and $\Delta\gamma$ to be the independent variables. These equations provide 13 equations for 13 unknowns (6 equations from Equation 3.51, 6 equations from Equation 3.52 and yield equation 3.54) which are to be solved using Newton's method (See Appendix A).

For isotropic hardening case back stress $\boldsymbol{\alpha}$ is not defined so, Equation 3.52 is not used and 3.51 and 3.54 are updated as follows, respectively:

$$\boldsymbol{\tau}_{n+1} = \boldsymbol{\tau}_{n+1}^{trial} - \mathcal{C} : \Delta\gamma\sqrt{\frac{3}{2}}\frac{\boldsymbol{\tau}'_{n+1}}{|\boldsymbol{\tau}'_{n+1}|} \tag{3.55}$$

$$\Phi = \sqrt{\frac{3}{2}}|\boldsymbol{\tau}'_{n+1}| - \left(\sigma_Y^0 + Q\left(1 - e^{-\beta\bar{\varepsilon}_{n+1}^{p}}\right)\right) = 0 \tag{3.56}$$

Equation 3.53 is the same for isotropic hardening.

For kinematic hardening only the yield Equation 3.56 is changed in the manner showed below.

$$\Phi = \sqrt{\frac{3}{2}}|\boldsymbol{\tau}'_{n+1} - \boldsymbol{\alpha}_{n+1}| - \sigma_Y^0 = 0 \tag{3.57}$$

It should be noted that for metals, elasto-plastic volume changes are so small that Kirchhoff stress is almost equal to Cauchy stress. [15]

$$\boldsymbol{\tau} \cong \boldsymbol{\sigma} \tag{3.58}$$

Because of that reason in all the equations above Cauchy stress can be used directly instead of Kirchhoff stress

3.2.3. Hyperelastic Based Plasticity

Hyperelastic based plasticity assumes multiplicative split of deformation gradient into elastic and plastic parts as [43]

$$\boldsymbol{F} = \boldsymbol{F}^{e}\boldsymbol{F}^{p} \tag{3.59}$$

The split can be shown schematically as in Figure 4.3. This separation leads to definitions of elastic and plastic right Cauchy-Green tensors:

$$\boldsymbol{C}^{e} = \boldsymbol{F}^{e^{T}}\boldsymbol{F}^{e} \tag{3.60}$$

$$\boldsymbol{C}^p = \boldsymbol{F}^{p^T}\boldsymbol{F}^p \tag{3.61}$$

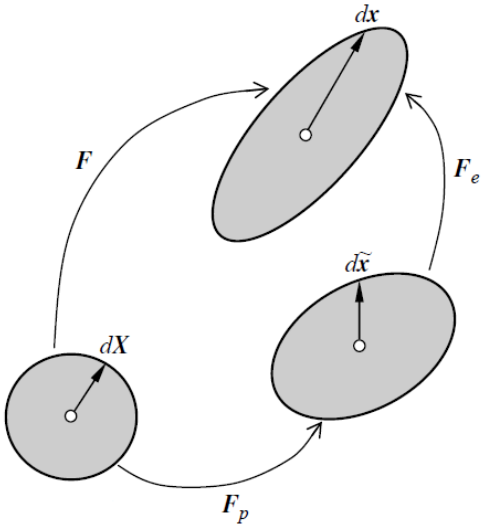

Figure 4.3 Schematic view of multiplicative split of deformation gradient [37]

Elastic potential referred to as Helmholtz free energy function has now two parts. Related to elastic deformation, ψ_e, and elastic part of the plastic deformation due to hardening ψ_{hard}. Hardening part can be further split into other parts depending on the hardening model. Elastic part is only dependent on elastic part of right Cauchy-Green tensor.

$$\psi = \psi_e(\boldsymbol{C}^e) + \psi_{hard} \tag{3.62}$$

Clausius-Duhem inequality which is an extension of the second law of thermodynamics to continuum mechanics is to be used in derivation of hyperelastic plastic model. It is stated as below:

$$-\dot{\psi} + \frac{1}{2}\boldsymbol{S} : \dot{\boldsymbol{C}} \geq 0 \tag{3.63}$$

where $\boldsymbol{S}$ is the second Piola-Kirchhoff stress tensor. Regardless of the hardening method used, Equation 3.63 can be written as

$$-\left(\frac{\partial\psi}{\partial\boldsymbol{C_e}}:\dot{\boldsymbol{C}}^e+\dot{\psi}_{hard}\right)+\frac{1}{2}\boldsymbol{S}:\ \dot{\boldsymbol{C}}\geq 0 \tag{3.64}$$

Using Equations 3.9, 3.59, 3.60, 3.61 right Cauchy-Green tensor $\boldsymbol{C}=\boldsymbol{F}^T\boldsymbol{F}$ can be written as

$$\boldsymbol{C}={\boldsymbol{F}^p}^T\boldsymbol{C}^e\boldsymbol{F}^p \tag{3.65}$$

and

$$\boldsymbol{C}^e={\boldsymbol{F}^p}^{-T}\boldsymbol{C}{\boldsymbol{F}^p}^{-1} \tag{3.66}$$

and taking its derivative using product rule gives:

$$\dot{\boldsymbol{C}}^e={\dot{\boldsymbol{F}}^p}{}^{-T}\boldsymbol{C}{\boldsymbol{F}^p}^{-1}+{\boldsymbol{F}^p}^{-T}\dot{\boldsymbol{C}}{\boldsymbol{F}^p}^{-1}+{\boldsymbol{F}^p}^{-T}\boldsymbol{C}{\dot{\boldsymbol{F}}^p}{}^{-1} \tag{3.67}$$

Making use of

$$\boldsymbol{F}^p{\boldsymbol{F}^p}^{-1}=\boldsymbol{I} \tag{3.68}$$

$$\dot{\boldsymbol{F}}^p{\boldsymbol{F}^p}^{-1}+\boldsymbol{F}^p{\dot{\boldsymbol{F}}^p}{}^{-1}=\boldsymbol{0} \tag{3.69}$$

Gives

$${\dot{\boldsymbol{F}}^p}{}^{-1}=-{\boldsymbol{F}^p}^{-1}\dot{\boldsymbol{F}}^p{\boldsymbol{F}^p}^{-1} \tag{3.70}$$

and from that it can be found that

$${\dot{\boldsymbol{F}}^p}{}^{-T}=-{\boldsymbol{F}^p}^{-T}{\dot{\boldsymbol{F}}^p}{}^T{\boldsymbol{F}^p}^{-T} \tag{3.71}$$

Plugging in equations 3.70 and 3.71 into Equation 3.67 together with Equation 3.66 gives

$$\dot{\boldsymbol{C}}^e=-{\boldsymbol{F}^p}^{-T}{\dot{\boldsymbol{F}}^p}{}^T\boldsymbol{C}^e+{\boldsymbol{F}^p}^{-T}\dot{\boldsymbol{C}}{\boldsymbol{F}^p}^{-1}-\boldsymbol{C}^e\dot{\boldsymbol{F}}^p{\boldsymbol{F}^p}^{-1} \tag{3.72}$$

$\dot{\boldsymbol{F}}^p{\boldsymbol{F}^p}^{-1}$ term in the above equation can be defined as plastic spatial velocity gradient and denoted as $\boldsymbol{L}^p$.

So, Equation 3.72 becomes

$$\dot{\boldsymbol{C}}^e = -\boldsymbol{L}^{p^T}\boldsymbol{C}^e + \boldsymbol{F}^{p^{-T}}\dot{\boldsymbol{C}}\boldsymbol{F}^{p^{-1}} - \boldsymbol{C}^e\boldsymbol{L}^p \tag{3.73}$$

Putting this equation into Equation 3.64 and rearranging gives:

$$\frac{\partial\psi}{\partial\boldsymbol{C}^e}:\boldsymbol{L}^{p^T}\boldsymbol{C}^e - \frac{\partial\psi}{\partial\boldsymbol{C}^e}:\boldsymbol{F}^{p^{-T}}\dot{\boldsymbol{C}}\boldsymbol{F}^{p^{-1}} + \frac{\partial\psi}{\partial\boldsymbol{C}^e}:\boldsymbol{C}^e\boldsymbol{L}^p + \frac{1}{2}\boldsymbol{S}:\dot{\boldsymbol{C}} - \dot{\psi}_{hard} \geq 0 \tag{3.74}$$

It should be noted here that ψ is an isotropic function of $\boldsymbol{C}^e$ [25] that ensures symmetry of the product $\boldsymbol{C}^e(\partial\psi/\partial\boldsymbol{C}^e)$ besides $\boldsymbol{C}^e$ and $\partial\psi/\partial\boldsymbol{C}^e$ so that skew symmetric part of the velocity gradient $\boldsymbol{L}^p$ produces zero when it goes into a ":" operation with $\boldsymbol{C}^e(\partial\psi/\partial\boldsymbol{C}^e)$. This leads to below simplifications.

$$\frac{\partial\psi}{\partial\boldsymbol{C}^e}:\boldsymbol{C}^e\boldsymbol{L}^p = \boldsymbol{C}^e\frac{\partial\psi}{\partial\boldsymbol{C}^e}:\boldsymbol{L}^p = \boldsymbol{C}^e\frac{\partial\psi}{\partial\boldsymbol{C}^e}:\boldsymbol{D}^p \tag{3.75}$$

$$\frac{\partial\psi}{\partial\boldsymbol{C}^e}:\boldsymbol{L}^{p^T}\boldsymbol{C}^e = \boldsymbol{C}^e\frac{\partial\psi}{\partial\boldsymbol{C}^e}:\boldsymbol{L}^{p^T} = \boldsymbol{C}^e\frac{\partial\psi}{\partial\boldsymbol{C}^e}:\boldsymbol{D}^p \tag{3.76}$$

Also, since both $\partial\psi/\partial\boldsymbol{C}^e$ and $\dot{\boldsymbol{C}}$ are symmetric the middle term in Equation 3.74 can be written as:

$$\frac{\partial\psi}{\partial\boldsymbol{C}^e}:\boldsymbol{F}^{p^{-T}}\dot{\boldsymbol{C}}\boldsymbol{F}^{p^{-1}} = \boldsymbol{F}^{p^{-1}}\frac{\partial\psi}{\partial\boldsymbol{C}^e}\boldsymbol{F}^{p^{-T}}:\dot{\boldsymbol{C}} \tag{3.77}$$

Applying Equations 3.75, 3.76, 3.77 to Equation 3.74. Clausius Duhem inequality takes the form:

$$\left(\boldsymbol{S} - 2\boldsymbol{F}^{p^{-1}}\frac{\partial\psi}{\partial\boldsymbol{C}^e}\boldsymbol{F}^{p^{-T}}\right):\frac{1}{2}\dot{\boldsymbol{C}} + \left(2\boldsymbol{C}^e\frac{\partial\psi}{\partial\boldsymbol{C}^e}\right):\boldsymbol{D}^p - \dot{\psi}_{hard} \geq 0 \tag{3.78}$$

Term $2\boldsymbol{C}^e(\partial\psi/\partial\boldsymbol{C}^e)$ is a stress like quantity and it is called Mandel stress. It will be shown as $\boldsymbol{M}$ from now on. Using [25]

$$\boldsymbol{S} = 2\boldsymbol{F}^{p^{-1}}\frac{\partial\psi}{\partial\boldsymbol{C}^e}\boldsymbol{F}^{p^{-T}} \tag{3.79}$$

Clausius-Duhem inequality reduces to:

$$\boldsymbol{M}:\boldsymbol{D}^p - \dot{\psi}_{hard} \geq 0 \tag{3.80}$$

This equation can be satisfied when flow rule is selected as:

$$\boldsymbol{D}^p = \dot{\gamma}\frac{\partial \Phi}{\partial \boldsymbol{M}} \tag{3.81}$$

3.2.3.1. Hyperelastic Based Plasticity with Isotropic Hardening Model

When only isotropic hardening is concerned Equation 3.62 becomes as follows:

$$\psi = \psi_e(\boldsymbol{C}^e) + \psi_{iso}(\bar{\varepsilon}^p) \tag{3.82}$$

Then Clausius-Duhem inequality gives:

$$-\left(\frac{\partial \psi_e}{\partial \boldsymbol{C}^e} : \dot{\boldsymbol{C}}^e + \frac{\partial \psi_{iso}}{\partial \bar{\varepsilon}^p}\dot{\bar{\varepsilon}}^p\right) + \frac{1}{2}\boldsymbol{S} : \dot{\boldsymbol{C}} \geq 0 \tag{3.83}$$

Following a similar procedure as in the previous section, after simplifications the equation given below is reached.

$$\left(\boldsymbol{S} - 2\boldsymbol{F}^{p^{-1}}\frac{\partial \psi}{\partial \boldsymbol{C}^e}\boldsymbol{F}^{p^{-T}}\right) : \frac{1}{2}\dot{\boldsymbol{C}} + \left(2\boldsymbol{C}^e\frac{\partial \psi}{\partial \boldsymbol{C}^e}\right) : \boldsymbol{D}^p - \frac{\partial \psi_{iso}}{\partial \bar{\varepsilon}^p}\dot{\bar{\varepsilon}}^p \geq 0 \tag{3.84}$$

To achieve analogous isotropic hardening type to that of in the case of hypoelastic based isotropic hardening model, this model is of Voce type isotropic hardening as well. For this reason, ψ_{iso} is selected as [25]:

$$\psi_{iso} = Q\left(\bar{\varepsilon}^p + \frac{e^{-\beta\bar{\varepsilon}^p}}{\beta}\right) \tag{3.85}$$

Von Mises type yield equation at the intermediate configuration becomes:

$$\Phi = \sqrt{\frac{3}{2}}|\boldsymbol{M}'| - \left[\sigma_Y^0 + Q\left(1 - e^{-\beta\bar{\varepsilon}^p}\right)\right] = 0 \tag{3.86}$$

where $\boldsymbol{M}'$ is the deviatoric Mandel stress tensor. Then using Equation 3.81, flow equation in the intermediate configuration becomes

$$\boldsymbol{D}^p = \dot{\gamma}\sqrt{\frac{3}{2}}\frac{\boldsymbol{M}'}{|\boldsymbol{M}'|} \tag{3.87}$$

Note here that tensors $\boldsymbol{M}$ and $\boldsymbol{M}'$ defined previously are in the intermediate configuration. Considering convenience for kinematic hardening, which is to be mentioned in the upcoming part, constitutive updates will be performed in the reference configuration. So, tensors $\boldsymbol{M}$ and $\boldsymbol{M}'$ should be pulled back to reference configuration with utilizing the equation below.

$$\dot{\boldsymbol{C}}^p = 2\boldsymbol{F}^{p^T}\boldsymbol{D}^p\boldsymbol{F}^p \tag{3.88}$$

Introducing Equation 3.87 and definition of $\boldsymbol{M}$ into Equation 3.88.

$$\dot{\boldsymbol{C}}^p = 2\sqrt{\frac{3}{2}}\dot{\gamma}\boldsymbol{F}^{p^T}\frac{\boldsymbol{M}'}{|\boldsymbol{M}'|}\boldsymbol{F}^p = 2\sqrt{\frac{3}{2}}\dot{\gamma}\frac{\mathbf{Y}'\boldsymbol{C}^p}{\sqrt{\mathbf{Y}':(\mathbf{Y}')^T}} \tag{3.89}$$

where $\mathbf{Y}'$ is the deviatoric part of non-symmetric stress like tensor $\mathbf{Y}$ which is defined as

$$\mathbf{Y} = \boldsymbol{C}\boldsymbol{S} \tag{3.90}$$

And yield equation in terms of $\mathbf{Y}$ is

$$\Phi = \sqrt{\frac{3}{2}}\sqrt{\mathbf{Y}':(\mathbf{Y}')^T} - \left[\sigma_Y^0 + Q\left(1 - e^{-\beta\bar{\varepsilon}^p}\right)\right] = 0 \tag{3.91}$$

with selection of ψ_e to be of Neo-Hookean type as

$$\begin{aligned}\psi_e = &\frac{\mu}{2}[tr(\boldsymbol{C}^e) - 3] - \mu\, ln\left[\sqrt{det(\boldsymbol{C}^e)}\right] \\ &+ \frac{\lambda}{4}\left\{det(\boldsymbol{C}^e) - 1 - 2\ln\left[\sqrt{det(\boldsymbol{C}^e)}\right]\right\}\end{aligned} \tag{3.92}$$

$\boldsymbol{S}$ can be determined using 3.79 to be

$$\boldsymbol{S} = \mu\left(\boldsymbol{C}^{p^{-1}} - \boldsymbol{C}^{-1}\right) + \frac{\lambda}{2}\left[\det(\boldsymbol{C})\det\left(\boldsymbol{C}^{p^{-1}}\right) - 1\right]\boldsymbol{C}^{-1} \tag{3.93}$$

After $\boldsymbol{S}$ is determined Cauchy-stress can be found using Equation 3.19, which is defined under the elasticity part.

3.2.3.2. Hyperelastic Kinematic Hardening Model

According to [44], plastic part of the deformation gradient $\boldsymbol{F}^p$ is needed to be split into additional two parts named as plastic elastic and plastic inelastic parts which creates an additional intermediate step of kinematic hardening in deformation.

$$\boldsymbol{F}^p = \boldsymbol{F}^{p_e}\boldsymbol{F}^{p_i} \tag{3.94}$$

Helmholtz free energy function and Clausius-Duhem inequality takes the following forms:

$$\psi = \psi_e(\boldsymbol{C}^e) + \psi_{kin}(\boldsymbol{C}^{p_e}) \tag{3.95}$$

$$-\left(\frac{\partial\psi_e}{\partial\boldsymbol{C}^e}:\dot{\boldsymbol{C}}^e + \frac{\partial\psi_{kin}}{\partial\boldsymbol{C}^{p_e}}:\dot{\boldsymbol{C}}^{p_e}\right) + \frac{1}{2}\boldsymbol{S}:\ \dot{\boldsymbol{C}} \geq 0 \tag{3.96}$$

This time using the definition

$$\boldsymbol{C}^{p_e} = (\boldsymbol{F}^{p_e})^T\boldsymbol{F}^{p_e} = (\boldsymbol{F}^{p_i})^{-T}\boldsymbol{C}^p(\boldsymbol{F}^{p_i})^{-1} \tag{3.97}$$

and separation defined in Equation 3.94, an equation similar to 3.73 is obtained as below

$$\dot{\boldsymbol{C}}^{p_e} = -(\boldsymbol{L}^{p_i})^T\boldsymbol{C}^{p_e} + (\boldsymbol{F}^{p_i})^{-T}\dot{\boldsymbol{C}}^p(\boldsymbol{F}^{p_i})^{-1} - \boldsymbol{C}^{p_e}\boldsymbol{L}^{p_i} \tag{3.98}$$

where, $\boldsymbol{L}^{p_i}$ is defined to be

$$\boldsymbol{L}^{p_i} = \dot{\boldsymbol{F}}^{p_i}(\boldsymbol{F}^{p_i})^{-1} \tag{3.99}$$

Putting Equation 3.99 into Equation 3.96, the term $-(\partial\psi_{kin}/\partial\boldsymbol{C}^{p_e}):\dot{\boldsymbol{C}}^{p_e}$ gives

$$\frac{\partial\psi_{kin}}{\partial\boldsymbol{C}^{p_e}}:(\boldsymbol{L}^{p_i})^T\boldsymbol{C}^{p_e} - \frac{\partial\psi_{kin}}{\partial\boldsymbol{C}^{p_e}}:(\boldsymbol{F}^{p_i})^{-T}\dot{\boldsymbol{C}}^p(\boldsymbol{F}^{p_i})^{-1} + \frac{\partial\psi_{kin}}{\partial\boldsymbol{C}^{p_e}}:\boldsymbol{C}^{p_e}\boldsymbol{L}^{p_i} \tag{3.100}$$

First and third terms in the above equation are simplified to

$$2\boldsymbol{C}^{p_e}\frac{\partial\psi_{kin}}{\boldsymbol{C}^{p_e}}:\boldsymbol{D}^{p_i} \tag{3.101}$$

where $\boldsymbol{D}^{p_i}$ is the symmetric part of $\boldsymbol{L}^{p_i}$. A similar stress like quantity to $\boldsymbol{M}$ emerges here which is defined as

$$\boldsymbol{M}_{kin} = 2\boldsymbol{C}^{p_e}\frac{\partial\psi_{kin}}{\boldsymbol{C}^{p_e}} \tag{3.102}$$

Middle term in Equation 3.100 found out to be

$$-\frac{\partial\psi_{kin}}{\partial\boldsymbol{C}^{p_e}}:(\boldsymbol{F}^{p_i})^{-T}\dot{\boldsymbol{C}}^{p}(\boldsymbol{F}^{p_i})^{-1} = -2\boldsymbol{F}^{p_e}\frac{\partial\psi_{kin}}{\partial\boldsymbol{C}^{p_e}}(\boldsymbol{F}^{p_e})^{T}:\boldsymbol{D}^{p} \tag{3.103}$$

That is reached with use of symmetry of the tensors $\partial\psi_{kin}/\partial\boldsymbol{C}^{p_e}$ and $\dot{\boldsymbol{C}}^{p}$ and the identity that is introduced in the following equation

$$\dot{\boldsymbol{C}}^{p} = 2\boldsymbol{F}^{p^T}\boldsymbol{D}^{p}\boldsymbol{F}^{p} \tag{3.104}$$

So, Equation 3.96 can be reassembled with this information to give

$$\begin{aligned}&\left(\boldsymbol{S} - 2\boldsymbol{F}^{p^{-1}}\frac{\partial\psi}{\partial\boldsymbol{C}^{e}}\boldsymbol{F}^{p^{-T}}\right):\frac{1}{2}\dot{\boldsymbol{C}}\\ &+\left[2\boldsymbol{C}^{e}\frac{\partial\psi}{\partial\boldsymbol{C}^{e}} - 2\boldsymbol{F}^{p_e}\frac{\partial\psi_{kin}}{\partial\boldsymbol{C}^{p_e}}(\boldsymbol{F}^{p_e})^{T}\right]:\boldsymbol{D}^{p}\\ &+2\boldsymbol{C}^{p_e}\frac{\partial\psi_{kin}}{\boldsymbol{C}^{p_e}}:\boldsymbol{D}^{p_i} \geq 0\end{aligned} \tag{3.105}$$

Term $2\boldsymbol{F}^{p_e}(\partial\psi_{kin}/\partial\boldsymbol{C}^{p_e})(\boldsymbol{F}^{p_e})^{T}$ is defined to be the back stress in the intermediate configuration shown as $\boldsymbol{\alpha}^{int}$. Simplifying the Clausius-Duhem inequality with the definitions of $\boldsymbol{M}$, $\boldsymbol{M}_{\boldsymbol{kin}}$ and $\boldsymbol{\alpha}^{int}$.

$$\left(\boldsymbol{M} - \boldsymbol{\alpha}^{int}\right):\boldsymbol{D}^{p} + \boldsymbol{M}_{kin}:\boldsymbol{D}^{p_i} \geq 0 \tag{3.106}$$

To satisfy the inequality the evolution equations are determined to be [25]

$$\boldsymbol{D}^{p} = \dot{\gamma}\sqrt{\frac{3}{2}}\frac{\boldsymbol{M}' - \boldsymbol{\alpha}^{int'}}{\left|\boldsymbol{M}' - \boldsymbol{\alpha}^{int'}\right|} \tag{3.107}$$

$$\boldsymbol{D}^{p_i} = \dot{\gamma}\sqrt{\frac{3}{2}\frac{b}{c}}\boldsymbol{M}'_{kin} \tag{3.108}$$

where $\boldsymbol{M}'_{kin}$ is the deviatoric kinematic Mandel stress tensor. Lastly, yield function of von Mises type is defined as

$$\Phi = \sqrt{\frac{3}{2}}\left|\boldsymbol{M}' - \boldsymbol{\alpha}^{int'}\right| - \sigma_Y^0 = 0 \tag{3.109}$$

As $\boldsymbol{M}$ is defined in the plastic intermediate step and $\boldsymbol{M}_{kin}$ is defined in the plastic inelastic intermediate step all equation should be pulled back to reference configuration to be updated which provides the following set of equations

$$\begin{aligned}\boldsymbol{\alpha} = \boldsymbol{F}^{p-1}\boldsymbol{\alpha}^{int}\boldsymbol{F}^{p-T} &= 2\boldsymbol{F}^{p-1}\boldsymbol{F}^{p_e}\frac{\partial\psi_{kin}}{\partial\boldsymbol{C}^{p_e}}(\boldsymbol{F}^{p_e})^T\boldsymbol{F}^{p-T} \\ &= 2(\boldsymbol{F}^{p_i})^{-1}\frac{\partial\psi_{kin}}{\partial\boldsymbol{C}^{p_e}}(\boldsymbol{F}^{p_i})^{-T}\end{aligned} \tag{3.110}$$

Using Equations 3.106 and 3.109

$$\dot{\boldsymbol{C}}^p = 2\sqrt{\frac{3}{2}}\dot{\gamma}\boldsymbol{F}^{p^T}\frac{\boldsymbol{M}' - \boldsymbol{\alpha}^{int'}}{\left|\boldsymbol{M}' - \boldsymbol{\alpha}^{int'}\right|}\boldsymbol{F}^p = 2\dot{\gamma}\sqrt{\frac{3}{2}}\frac{\mathbf{Y}'\boldsymbol{C}^p}{\sqrt{\mathbf{Y}':(\mathbf{Y}')^T}} \tag{3.111}$$

This time $\mathbf{Y}$ is defined to be

$$\mathbf{Y} = \boldsymbol{C}\boldsymbol{S} - \boldsymbol{C}^p\boldsymbol{\alpha} \tag{3.112}$$

Pulling back $\boldsymbol{D}^{p_i}$ with

$$\dot{\boldsymbol{C}}^{p_i} = 2(\boldsymbol{F}^{p_i})^T\boldsymbol{D}^{p_i}\boldsymbol{F}^{p_i} \tag{3.113}$$

$$\dot{\boldsymbol{C}}^{p_i} = 2\sqrt{\frac{3}{2}\frac{b}{c}}(\boldsymbol{F}^{p_i})^T\boldsymbol{M}'_{kin}\boldsymbol{F}^{p_i} = 2\dot{\gamma}\sqrt{\frac{3}{2}\frac{b}{c}}\mathbf{Y}'_{kin}\boldsymbol{C}^{p_i} \tag{3.114}$$

where $\boldsymbol{Y}_{kin}$ is defined to be

$$\boldsymbol{Y}_{kin} = \boldsymbol{C}^p\boldsymbol{\alpha} \tag{3.115}$$

Yield function of von Mises type takes the form

$$\Phi = \sqrt{\frac{3}{2}}\sqrt{\mathbf{Y}':(\mathbf{Y}')^{\boldsymbol{T}}} - (\sigma_Y^0) = 0 \tag{3.116}$$

ψ_e is again of Neo-Hookean type and can be taken as in Equation 3.92. So that expression for $\boldsymbol{S}$ is the same as that for isotropic hardening which is given in equation 3.93. For determination of $\boldsymbol{\alpha}$ free energy potential ψ_{kin} is selected to be [15]

$$\psi_{kin} = \frac{c}{4}\left[tr(\boldsymbol{C}^{p_e}) - 3\right] - \frac{c}{2} ln\left[\sqrt{det(\boldsymbol{C}^{p_e})}\right] \tag{3.117}$$

which gives $\boldsymbol{\alpha}$ through Equation 3.110 to be

$$\boldsymbol{\alpha} = \frac{c}{2}\left[(\boldsymbol{C}^{p_i})^{-1} - \boldsymbol{C}^{p^{-1}}\right] \tag{3.118}$$

These equations define hyperelastic kinematic hardening material together with the equation for second Piola-Kirchhoff stress defined as in Equation 3.95. After all the parameters are calculated Cauchy stress can be again found by pushing forward the second Piola-Kirchhoff stress using Equation 3.19.

3.2.3.3. Hyperelastic Combined Hardening Model

Hyperelastic combined hardening model is very similar to kinematic hardening model. There is an additional term for Helmholtz free energy function and that brings an additional term into Clausius-Duhem inequality. Free energy function:

$$\psi = \psi_e(\boldsymbol{C}^e) + \psi_{kin}(\boldsymbol{C}^{p_e}) + \psi_{iso}(\bar{\varepsilon}^p) \tag{3.119}$$

Clausius-Duhem inequality:

$$\begin{aligned} &\left(\boldsymbol{S} - 2\boldsymbol{F}^{p^{-1}}\frac{\partial\psi}{\partial\boldsymbol{C}^e}\boldsymbol{F}^{p^{-T}}\right):\frac{1}{2}\dot{\boldsymbol{C}} \\ &+ \left[2\boldsymbol{C}^e\frac{\partial\psi}{\partial\boldsymbol{C}^e} - 2\boldsymbol{F}^{p_e}\frac{\partial\psi_{kin}}{\partial\boldsymbol{C}^{p_e}}(\boldsymbol{F}^{p_e})^T\right]:\boldsymbol{D}^p \\ &+ 2\boldsymbol{C}^{p_e}\frac{\partial\psi_{kin}}{\boldsymbol{C}^{p_e}}:\boldsymbol{D}^{p_i} - \frac{\partial\psi_{iso}}{\partial\bar{\varepsilon}^p}\bar{\varepsilon}^p \geq 0 \end{aligned} \tag{3.120}$$

Equations 3.93, 3.111, 3.118 are valid for combined hardening only the yield function changes to be in the intermediate configuration

$$\Phi = \sqrt{\frac{3}{2}}\left|\boldsymbol{M}' - \boldsymbol{\alpha}^{int'}\right| - \left[\sigma_Y^0 + Q\left(1 - e^{-\beta\bar{\varepsilon}^p}\right)\right] = 0 \tag{3.121}$$

and at the reference configuration

$$\Phi = \sqrt{\frac{3}{2}}\sqrt{\mathbf{Y}' : (\mathbf{Y}')^{\boldsymbol{T}}} - \left[\sigma_Y^0 + Q\left(1 - e^{-\beta\bar{\varepsilon}^p}\right)\right] \tag{3.122}$$

These equations define hyperelastic combined hardening material completely.

3.2.3.4. Algorithmic Implementation

First, an explanation for algorithmic implementation for combined hardening will be made. At the beginning of the step material has to be checked for yielding, so first $\boldsymbol{C}$ is assumed to be fully elastic

$$\boldsymbol{C} = \boldsymbol{C}^e \tag{3.123}$$

$$\boldsymbol{C}^p = \boldsymbol{I} \tag{3.124}$$

Then a trial stress $\boldsymbol{S}^{trial}$ is calculated using Equation 3.93. This trial stress is used to find $\mathbf{Y}$ from Equation 3.112 and put into yield function 3.121 for yield check similar to the hypoelastic case. If $\sigma_Y \geq \sqrt{\frac{3}{2}}\sqrt{\mathbf{Y}' : (\mathbf{Y}')^{\boldsymbol{T}}}$ is satisfied, yielding has not occurred and found value for $\boldsymbol{S}^{trial}$ is to be used for $\boldsymbol{S}$, if not, plastic update equations should be used.

For integration backward Euler method is used, so equations for $\boldsymbol{C}^p$ and $\boldsymbol{C}^{p_i}$ can be updated by using Equations 3.111 and 3.114. From now on tensors obtained in the previous time step is to be shown with a superscript n and that belong to current time step is to be shown with a superscript $n + 1$.

$$\boldsymbol{C}^{p}_{n+1} = \boldsymbol{C}^{p}_{n} + 2\Delta\gamma\sqrt{\frac{3}{2}}\frac{\boldsymbol{Y}'_{n+1}\boldsymbol{C}^{p}_{n+1}}{\sqrt{\boldsymbol{Y}'_{n+1}\colon(\boldsymbol{Y}'_{n+1})^{T}}} \tag{3.125}$$

$$\boldsymbol{C}^{p_i}_{n+1} = \boldsymbol{C}^{p_i}_{n} + 2\Delta\gamma\sqrt{\frac{3}{2}}\frac{b}{c}\boldsymbol{Y}'_{kin_{n+1}}\boldsymbol{C}^{p_i}_{n+1} \tag{3.126}$$

Then the yield function can be obtained from 3.122 as:

$$\Phi = \sqrt{\frac{3}{2}}\sqrt{\boldsymbol{Y}'_{n+1}\colon(\boldsymbol{Y}'_{n+1})^{\boldsymbol{T}}} - \left[\sigma^{0}_{Y} + Q\left(1 - e^{-\beta\bar{\varepsilon}^{p}_{n+1}}\right)\right] \tag{3.127}$$

and update for equivalent plastic strain is performed in the same manner as in the hypoelastic case

$$\bar{\varepsilon}^{p}_{n+1} = \bar{\varepsilon}^{p}_{n} + \Delta\gamma \tag{3.128}$$

$\Delta\gamma$, components of the symmetric tensors $\boldsymbol{C}^{p}_{n+1}$, $\boldsymbol{C}^{p_i}_{n+1}$ are selected to be the update variables. $\bar{\varepsilon}^{p}_{n+1}$ is a dependent variable since it is directly related to $\Delta\gamma$ through Equation 3.128. Equations 3.125, 3.126, 3.127 and 3.128 completely define hyperelastic combined hardening material producing 13 equations for 13 unknowns. These set of equations can again be solved using Newton's Method (Appendix A).

Considering ABAQUS/Vumat, for updating stress equation $\boldsymbol{\sigma} = J^{-1}\boldsymbol{USU}^{T}$ should be used instead of $\boldsymbol{\sigma} = J^{-1}\boldsymbol{FSF}^{T}$ since it is stated that the rotation is already taken into account by the program automatically. $\boldsymbol{U}$ is the stretch tensor defined in Equation 3.9.

For isotropic hardening case, $\mathbf{Y}$ is defined through Equation 3.90 and Equation 3.126 is omitted. Update variables are $\boldsymbol{C}^{p}_{n+1}$ and $\Delta\gamma$ giving a total of 7 equations for 7 unknowns.

Lastly for kinematic hardening, only the yield function needed to be changed as follows:

$$\Phi = \sqrt{\frac{3}{2}}\sqrt{\boldsymbol{Y}'_{n+1} : (\boldsymbol{Y}'_{n+1})^{\boldsymbol{T}}} - \sigma_Y^0 \tag{3.128}$$

Equations 3.125, 3.126 and 3.12.7 are still valid giving again 13 equations for 13 unknowns to be solved.

CHAPTER 4

FINITE ELEMENT METHOD

Finite element method is a common method encountered in analyzing engineering problems. It is a numerical approach that solves differential equations arising from physical problem, approximately [45]. Generally finite element method is applied onto bodies by subdividing them into smaller and simpler regions which are referred to as mesh.

The problem is solved by formulating the equations for each of these sub-elements (mesh) and combining the solution after, rather than solving the problem for the whole geometry in one go [46]. This method greatly simplifies the solution since these elements have much simpler geometry (tetrahedron, hexahedron etc.) than the whole structure.

Two different basic approaches in finite element method are present, linear and non-linear methods. Linear methods are applicable when there is a linear relation between stress and strain is present. For example, in elastic deformation of metals modulus of elasticity is used to describe this linear relation. On the other hand, when deformations are large (geometrical non-linearity, material non-linearity), or system has kinematic constraints (contact non-linearity) non-linear solution methods are applied to solve the problem

Generally, a linear finite element problem can be solved in four steps which are presented in Figure 3.2. Firstly, differential equations describing the problem are formed. These equations involve boundary conditions as well which describe the behavior of the model at the boundaries. Obtained equations are referred to as “strong form” of the governing equations which are than simplified into an equivalent set of equation that is called “weak form”. This “weak form” is composed of integral equations which are more convenient for finite element approach than “strong form” equations. After “weak form” is obtained, finite element approximation is applied to these equations that make way for transforming the problem into a set of linear equations.

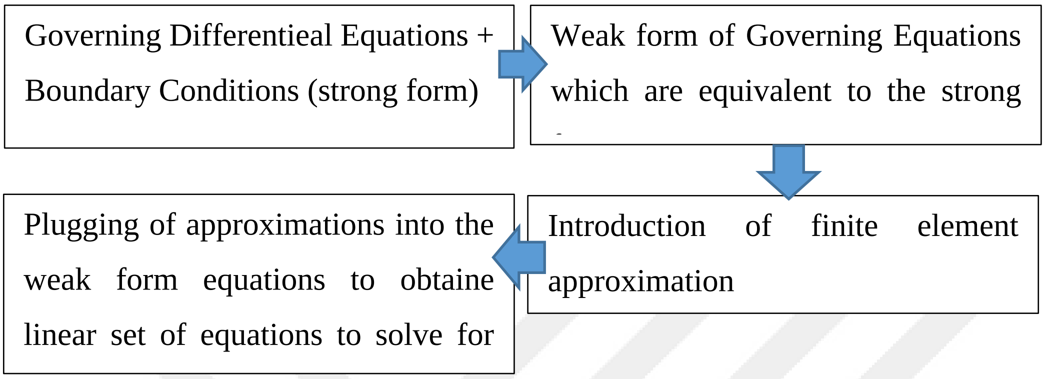

Figure 4.1 Solving steps of a linear finite element problem [46]

4.1. Method Used in the Thesis

In the thesis commercial finite element program ABAQUS/Explicit (Version 2016.HF.2) is used to simulate axisymmetric cylindrical cup drawing, square cup drawing and axisymmetric round bottom cup drawing processes. Since deep drawing processes involve large amounts of plastic deformation, which is highly non-linear in nature, formulation used is based on non-linear solution method of ABAQUS software (NLGEOM (geometric nonlinearity effects) option selected as on) ABAQUS/Explicit.

ABAQUS/Explicit uses direct integration of equation of motion considering inertial effects. It uses explicit integration central difference integration rule (forward Euler, dynamic integration method) with lumped element mass matrices. Equation used to calculate local acceleration at the nodes is based on Newton’s Second Law of Motion and is as below [42].

$$\ddot{u}|_{(t)} = M^{-1}(P - I)|_{(t)} \tag{4.1}$$

Here $\ddot{u}$ is acceleration, M is lumped mass P is external load vector and I is internal load vector. The value of acceleration is used to calculate velocity of the node at the current time step through integration from previous time step from which displacements are calculated.

A stable time increment is calculated by ABAQUS/Explicit depending on the effective size of the smallest element in the model using the following formula.

$$\Delta t = \frac{L_e}{c_d} \tag{4.2}$$

where L_e is effective element size and c_d is current dilatational wave speed of the element. The problem is solved explicitly by discretizing the simulation time into these small time steps which are also updated during the simulation as well.

The hypo- and hyperelastic, isotropic, kinematic and combined hardening models are implemented to ABAQUS/Explicit by use of material subroutine called VUMAT. Microsoft Visual Studio 2010, in combination with Intel Parallel Studio 2015 are linked to ABAQUS 2016.HF2 for compilation of subroutine codes written in Fortran coding language.

4.2. Finite Element Models

Models of cylindrical, square and round bottom cup drawings are formed within the finite element package ABAQUS. Considering the isotropy of the models cylindrical and round bottom drawings are modelled axisymmetrically, whereas one fourth of the square model is modelled due to symmetry conditions. Punch, holder and die are modelled to be rigid parts.

4.2.1. Cylindrical Cup Drawing

Two different cylindrical cup drawing simulations are performed. The first one is to verify the model using the parameters taken from work of Brepols et al. [15]. Parameters of the second one is taken from Çoğun’s study [47]. All of these values are presented in the table below.

Table 4.1 Cylindrical cup drawing parameters

	Brepols et al. [15]	Çoğun [47]	
Punch diameter	50 mm	50 mm	
Punch shoulder radius	5 mm	4.5 mm	
Die opening diameter	52.8 mm	53 mm	
Die shoulder radius	5 mm	13.5 mm	
Blank diameter	100 mm	110 mm	
Sheet thickness	1 mm	1 mm	
Friction coefficient	0.02	0.06	
Blankholder force	5 kN	SS304	900 N
		DKP6112	500 N

In figures 4.2 and 4.3 assemblies of the models of cylindrical cup drawing can be seen. Both of them are modelled axisymmetrically. Punch, holder and die are modelled as analytical rigid, whereas blank is formed with quadrilateral elements having type CAX4 having 372 elements in the simulations that uses the parameters of Brepols et al. [15] and 220 elements in the ones using Çoğun's [47] parameters. Both models have four elements through thickness of blank.

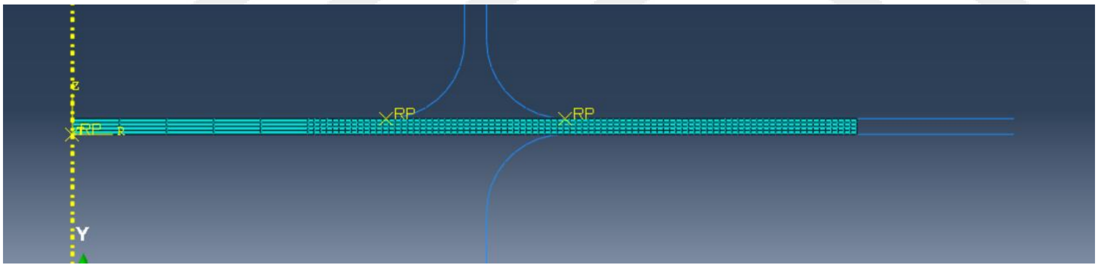

Figure 4.2 Cylindrical cup drawing assembly and mesh of the blank with parameters of Brepols et al. [15]

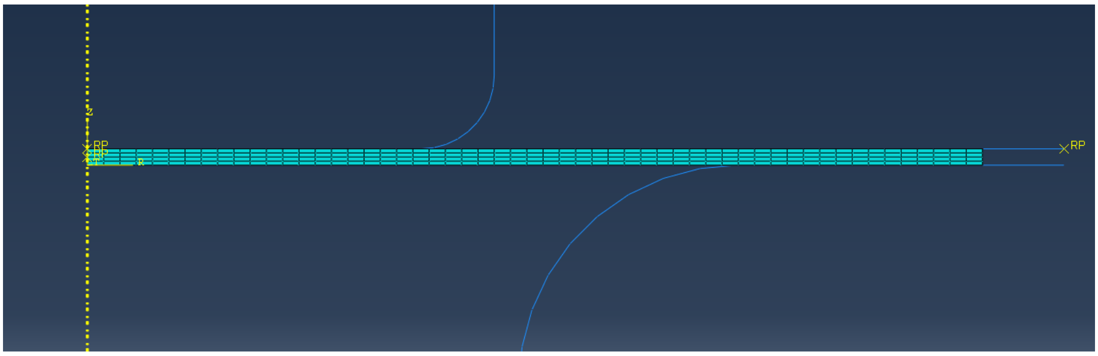

Figure 4.3. Cylindrical cup drawing assembly and mesh of the blank with parameters of Çoğun [47]

4.2.2. Square Cup Drawing

Parameters for square cup drawing is taken from the work of Çoğun [47] again. They are presented in the table below.

Table 4.2 Square cup drawing parameters

Punch dimensions	40 x 40 mm	
Punch edge radius	4.5 mm	
Punch shoulder radius	10 mm	
Die opening dimensions	42 x 42 mm	
Die shoulder radius	4.5 mm	
Blank dimensions	80 x 80 mm	
Sheet thickness	1 mm	
Friction coefficient	0.06	
Blankholder force	SS304	900 N
	DKP6112	500 N

Figure 4.4 shows the simulation setup of the square cup drawing process. Punch, holder and the die again modelled to be discrete rigid. The blank in the model is deformable, 3-D and discretized by 4096 linear hexahedral elements of C3D8R type having four elements in the thickness direction.

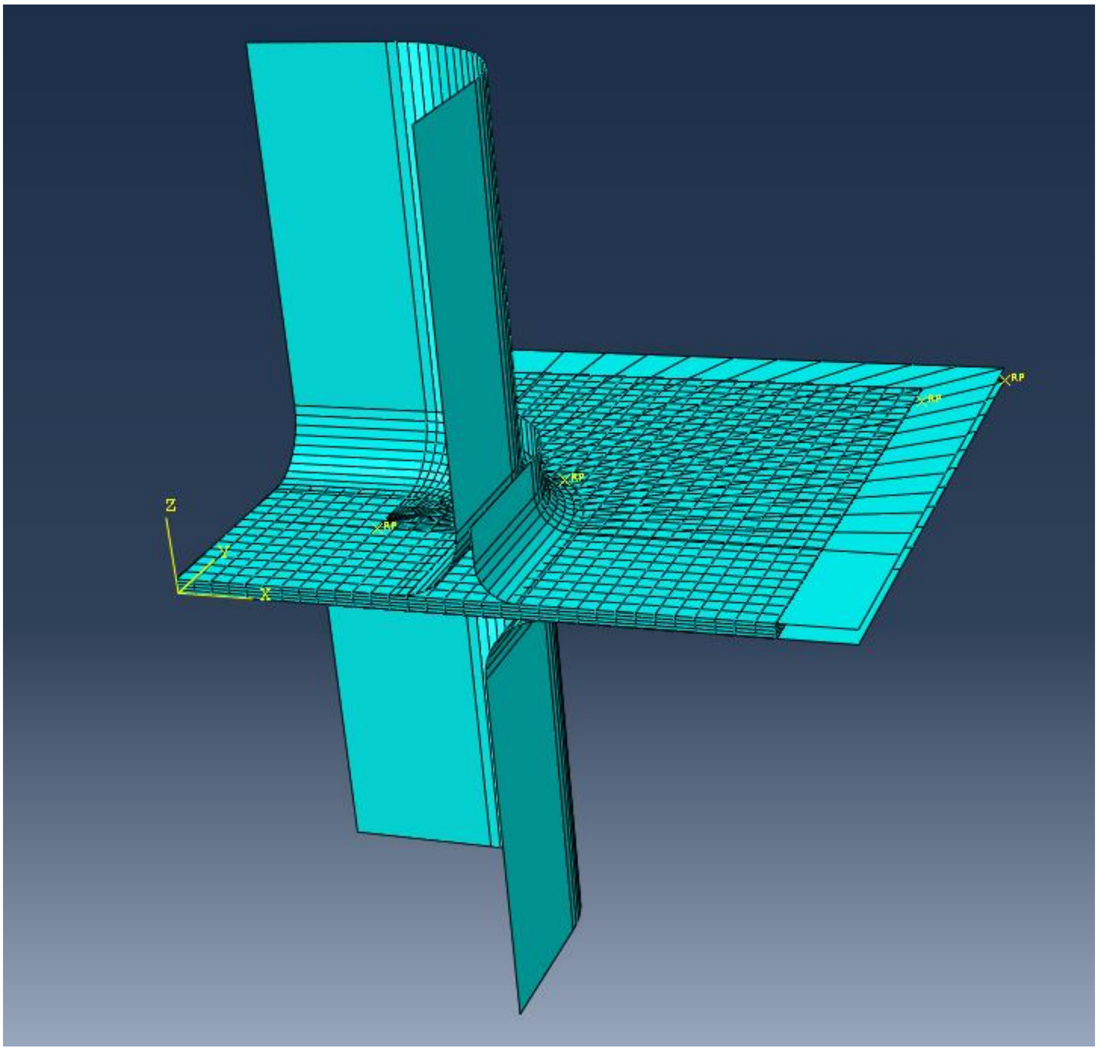

Figure 4.4. Square cup drawing assembly

4.2.3. Round Bottom Cup Drawing

Assembly of the round bottom cup drawing simulation can be seen in Figure 4.5. The setup is quite similar to that of cylindrical cup drawing having punch, holder and die modelled as analytical rigid elements. Blank has the same mesh as in the cylindrical one. Parameters of the set up taken from [47] are given in Table 4.3.

Table 4.3 Round bottom cup drawing parameters

Punch diameter	50 mm
Die opening diameter	53 mm
Die shoulder radius	13.5 mm

Blank diameter	110 mm	
Sheet thickness	1 mm	
Friction coefficient	0.06	
Blankholder force	SS304	1400 N
	DKP6112	900 N

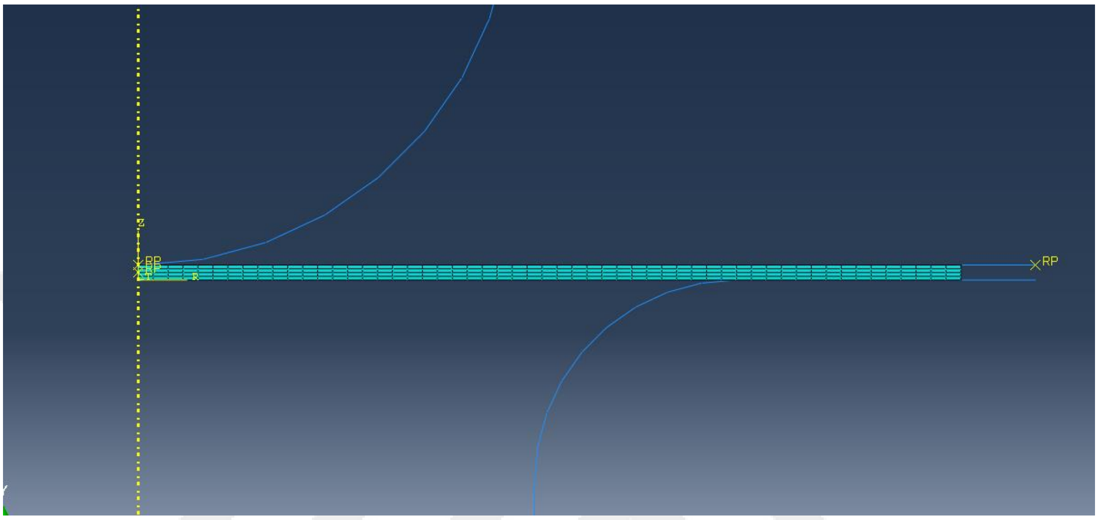

Figure 4.5 Round bottom cup drawing assembly and mesh of the blank

CHAPTER 5

MATERIAL DATA

To verify the model implemented in ABAQUS/Vumat cylindrical cup drawing results of Brepols et al. [15] are used. Material data used in the study is for DP600 sheet metal and it is from the work of Vladimirov et al. [24]. Furthermore, two additional material data, namely SS304 and DKP6112 are used in the thesis. Information related to this is taken from Çoğun's study [47].

5.1. Determination of Material Constants

In this part procedure for determination of material constants is explained. Hypoelastic based plastic material model is used for fitting the data and same constants is used for both hypoelastic and hyperelastic based analysis. This procedure is carried out in MATLAB R2017a.

5.1.1. Isotropic Hardening

Voce type isotropic hardening model [14] has only two constants Q and β. To determine the set of constants Q and β are varied between a certain range and they are used in the yield equation given in 5.2. Strain values taken from average uniaxial data are used together with Q and β in Equation 5.2 to find estimated true stress (σ_{est}) values. Then these estimated true stresses obtained are subtracted from those taken from uniaxial data $\left(\sigma_{exp}\right)$ to find the error in the estimated value (σ_{err}). Since there is only uniaxial loading

$$\bar{\varepsilon}^p = \varepsilon_{11} \tag{5.1}$$

$$\sigma_{est} = \sigma_Y^0 + Q\left(1 - e^{-\beta\bar{\varepsilon}^p}\right) \tag{5.2}$$

$$\sigma_{err} = \sigma_{est} - \sigma_{exp} \tag{5.3}$$

Q and β that give the least amount of error is to be determined next. This is done by finding root mean square (rms) of the error. Dataset that results in the least rms value is selected and used in the material model. For n number of data points rms is defined as:

$$\text{rms} = \sqrt{\frac{(\sigma_{err}^{1})^2 + (\sigma_{err}^{2})^2 + ..(\sigma_{err}^{n})^2}{n}} \tag{5.4}$$

where σ_{err}^{n} is error for n$^{\text{th}}$ data point.

5.1.2. Kinematic Hardening

For non-linear Armstrong and Frederick type kinematic hardening [13] there are two constants to be determined; b and c. A similar procedure to isotropic hardening case is followed, however, this time, even though there is loading only in one direction, there are back stress components in every primary coordinate direction. This results in having four unknowns ($\sigma_{est}, \alpha_{11},\ \alpha_{22},\ \alpha_{33}$) to be determined at each step for the guess of b and c. Through Equation 3.36

$$\sigma_{11}' = \frac{2}{3}\sigma_{est} \tag{5.5}$$

$$\sigma_{22}' = \sigma_{33}' = -\frac{1}{3}\sigma_{est} \tag{5.6}$$

and by using update equation of back stress for hypoelastic kinematic hardening (Equation 3.41) three equations is formed as:

$$\alpha_{11} = \alpha_{11_n} + \Delta\gamma\sqrt{\frac{3}{2}}\left(c\frac{\sigma_{11}' - \alpha_{11}}{|\boldsymbol{\sigma}' - \boldsymbol{\alpha}|} - b\alpha_{11}\right) \tag{5.7}$$

$$\alpha_{\mathbf{22}} = \alpha_{22_n} + \Delta\gamma\sqrt{\frac{3}{2}}\left(c\frac{\sigma_{22}' - \alpha_{22}}{|\boldsymbol{\sigma}' - \boldsymbol{\alpha}|} - b\alpha_{22}\right) \tag{5.8}$$

$$\alpha_{\mathbf{33}} = \alpha_{33_n} + \Delta\gamma\sqrt{\frac{3}{2}}\left(c\frac{\sigma'_{33} - \alpha_{\mathbf{33}}}{|\boldsymbol{\sigma}' - \boldsymbol{\alpha}|} - b\alpha_{\mathbf{33}}\right) \tag{5.9}$$

In these equations quantities which are not labeled with subscript n belong to current step $n+1$.

Note that $\Delta\gamma$ which is calculated from uniaxial data, is a known quantity for every calculation step. It is defined for consecutive steps as

$$\Delta\gamma_{n+1} = \bar{\varepsilon}^p_{n+1} - \bar{\varepsilon}^p_n \tag{5.10}$$

and using yield condition

$$\sqrt{\frac{3}{2}}|\boldsymbol{\sigma}'_{n+1} - \boldsymbol{\alpha}_{n+1}| - \sigma^0_Y = 0 \tag{5.11}$$

These equations result in four unknowns $(\sigma_{11}, \alpha_{11}, \alpha_{\mathbf{22}}, \alpha_{\mathbf{33}})$ in four equations which can be solved using Newton's Method (Appendix A).

After σ_{11} is determined for the step a similar procedure as in the isotropic case is followed to compare the value of it to that of σ_{exp}. Equations 5.3 and 5.4 are used for kinematic hardening case as well. b and c values whose rms value is the smallest selected as material parameters.

5.1.3. Combined Hardening

Combined hardening requires four parameters (Q, β, b, c) to be varied and determined for the least amount of rms. For combined hardening case Equations 5.7, 5.8 and 5.9 can be used exactly. Only the yield equation is to be changed to

$$\sqrt{\frac{3}{2}}|\boldsymbol{\sigma}'_{n+1} - \boldsymbol{\alpha}_{n+1}| - \left[\sigma^0_Y + Q\left(1 - e^{-\beta\bar{\varepsilon}^p_{n+1}}\right)\right] = 0 \tag{5.12}$$

5.2. Material Properties and Constants

Elastic (Lame constants λ and μ) and plastic characteristics (yield stress σ_Y^0) of materials were determined by uniaxial tension test. These are summarized in the table below

Table 5.1 Elastic properties of materials

Material	λ [MPa]	μ [MPa]	Yield Strength from Rolling Direction [MPa]			Average Yield Strength (σ_Y^0)
			0°	45°	90°	
DP600	140753.5	72509.4	325	-	-	325
SS304	62470	79510	339	325	342	332.75
DKP6112	95210	53560	245	258	238	256

Data for SS304 and DKP6112 given in above table account for anisotropy in the undeformed sheets caused by rolling operation implemented beforehand to give material the desired thickness. These two materials show slight anisotropy and so they can be modeled as isotropic, but this anisotropic data set must be converted into an isotropic data set. To achieve this, equation given below is used.

$$\sigma_m = \frac{\sigma_{0^\circ} + 2\sigma_{45^\circ} + \sigma_{90^\circ}}{4} \tag{5.13}$$

This equation is applied to every point that determines the uniaxial stress-strain curve of SS304 and DKP6112 that is direction dependent available in [47].

Constants that determine plastic characteristic of materials are given in the table below. For DP600 sheet metal constants are directly taken from the study of Vladimirov et al. [24], while for SS304 and DKP6112 they are determined through procedure explained in section 5.1 together with average uniaxial data calculated by using Equation 5.13.

Table 5.2 Plastic constants of materials

Material	Hardening rule	Q [MPa]	β [-]	b [-]	c [MPa]

DP600	Isotropic	420	20	-	-
	Kinematic	-	-	7.75	2750
	Combined	215	8	12.5	2600
SS304	Isotropic	1190	2.2	-	-
	Kinematic	-	-	1.8	1765
	Combined	1185	0.1	1.9	1685
DKP6112	Isotropic	200	11.7	-	-
	Kinematic	-	-	10.1	1665
	Combined	150	3	15	1490

Comparison of the uniaxial experimental data with the models formed by using the parameters determined for three hardening models for SS304 and DKP6112 are presented in figures 5.1 and 5.2.

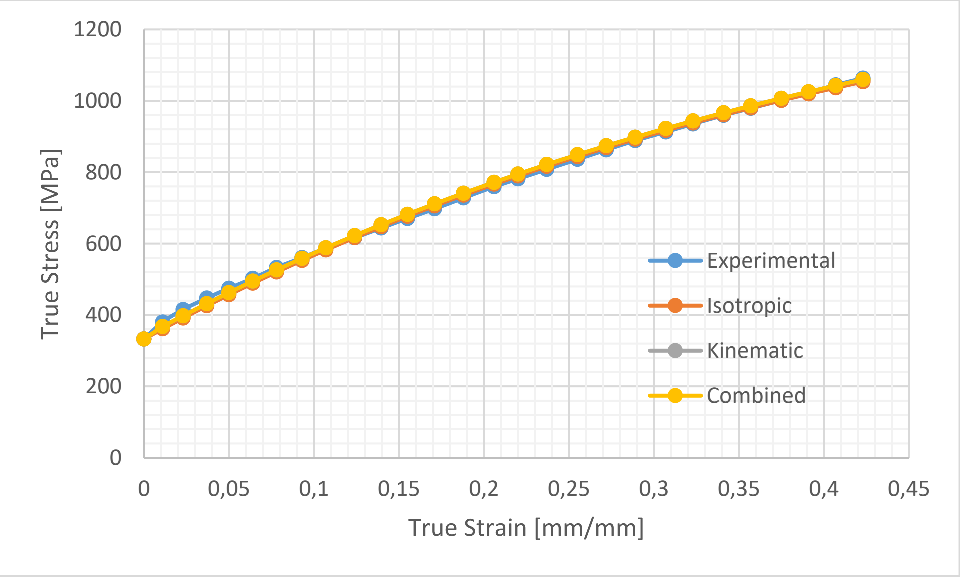

Figure 5.1 Fit of material models to experimental data for SS304

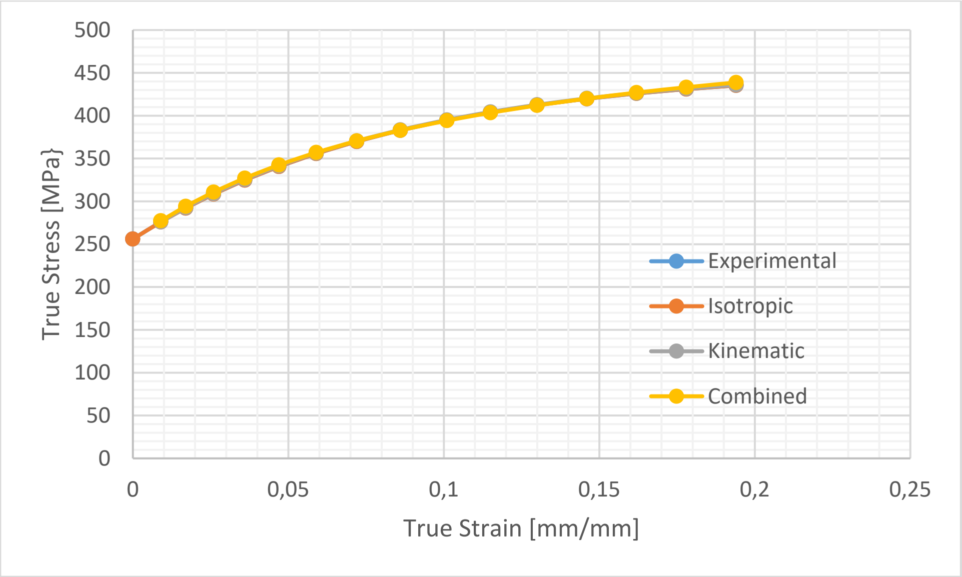

Figure 5.2 Fit of material models to experimental data for DKP6112

CHAPTER 6

NUMERICAL RESULTS

In this part of the thesis numerical results obtained by using the material models discussed in Chapter 3 will be presented. Firstly, a verification of the model is done by comparing the prepared model to a similar one from the literature. After that a general comparison of the different hardening models coupled with hypoelastic and hyperelastic type material models is accomplished by using their punch force estimation. Lastly, same models are compared in terms of their thickness strain distribution for three different types of deep drawing operations namely, cylindrical, square and round bottom with two different material types, SS304 and DKP6112.

6.1. Cylindrical Cup Drawing of DP600

Data used in this part is taken from the work of Brepols et al. [15]. Material properties used in simulations are taken from the study of Vladimirov et al. [24]. For this section, simulation of a cylindrical cup drawing process is made, by using DP600 material and the dimensions of the die, blank and blank holder together are given in Table 4.1.

6.1.1. Verification of the Model

In this section, the results obtained by Brepols et al. [15] who used a combined hardening model in their work are compared to the results obtained by the combined hardening model that is developed in this study. Comparison of the results is made in terms of punch force determined with respect to punch displacement during the forming operation (Figure 6.1)

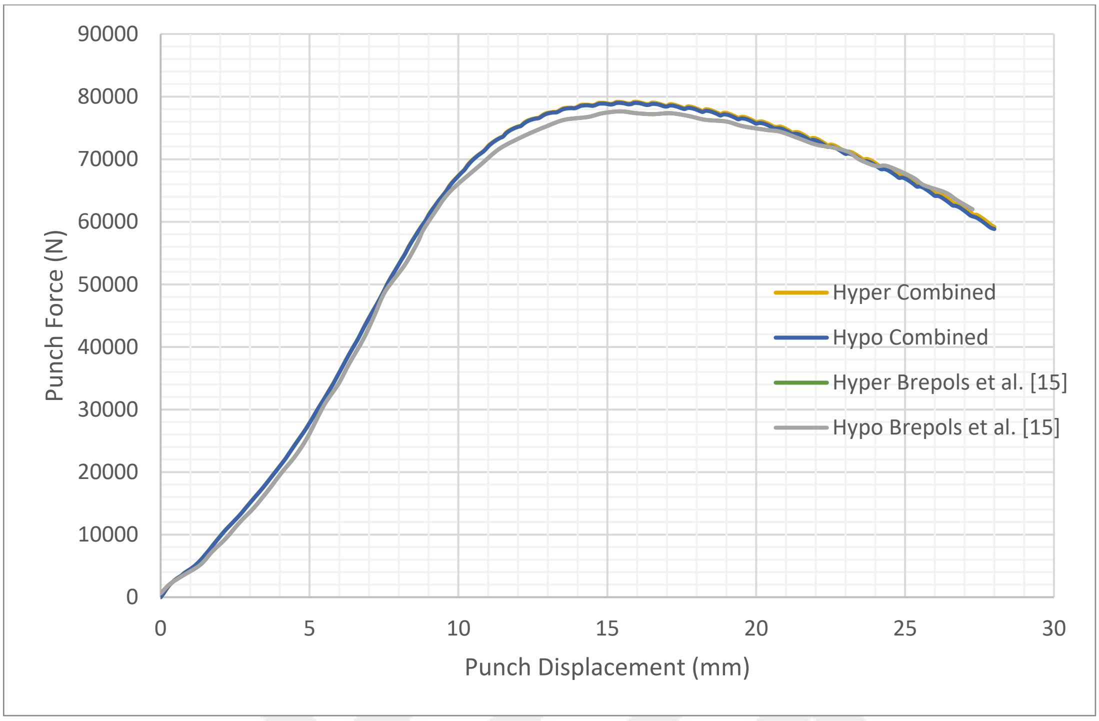

Figure 6.1. Comparison of combined hardening results to results of Brepols et al. [15]

Results obtained are very close to the results of Brepols et al. slightly overestimating the maximum punch force. At most 2.5% difference in the results can be seen which is achieved around 12 mm punch displacement. Nevertheless, these results confirm the validity of the developed Vumat code.

6.1.2. Comparison of Different Hardening Models

In figure 6.2 below the results obtained by the developed model for isotropic, kinematic and combined hardening models for both hypoelastic and hyperelastic cases are given.

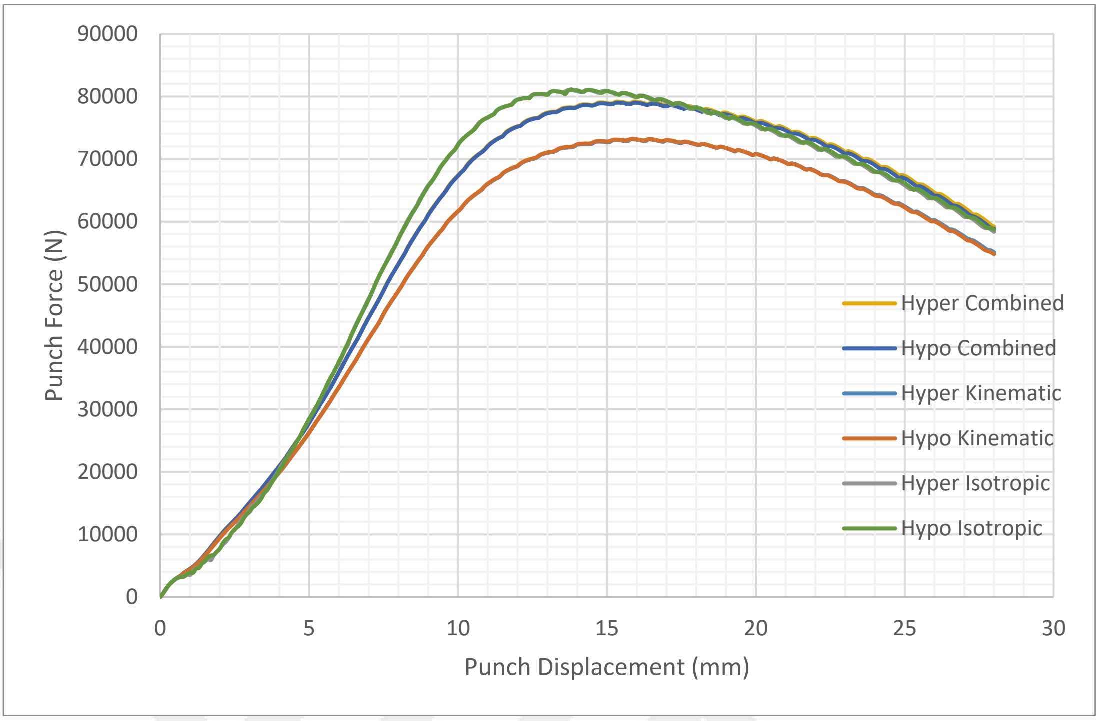

Figure 6.2. Comparison of hypo- and hyperelastic models with combination of different hardening models in terms of punch force estimation in cylindrical cup drawing process

As it can be seen from the Figure 6.2 isotropic hardening model overestimates the punch force compared to the combined hardening model, whereas, kinematic hardening model underestimates it. There is almost no difference in results obtained between hypoelastic and hyperelastic models.

6.2. Results of SS304

In this section numerically found thickness strain distributions of the deformed sheets at different punch displacements are presented.

6.2.1. Cylindrical Cup Drawing Results

In this section, the results obtained for different punch height in cylindrical cup drawing of SS304 are given

6.2.1.1. 20 mm Punch Displacement

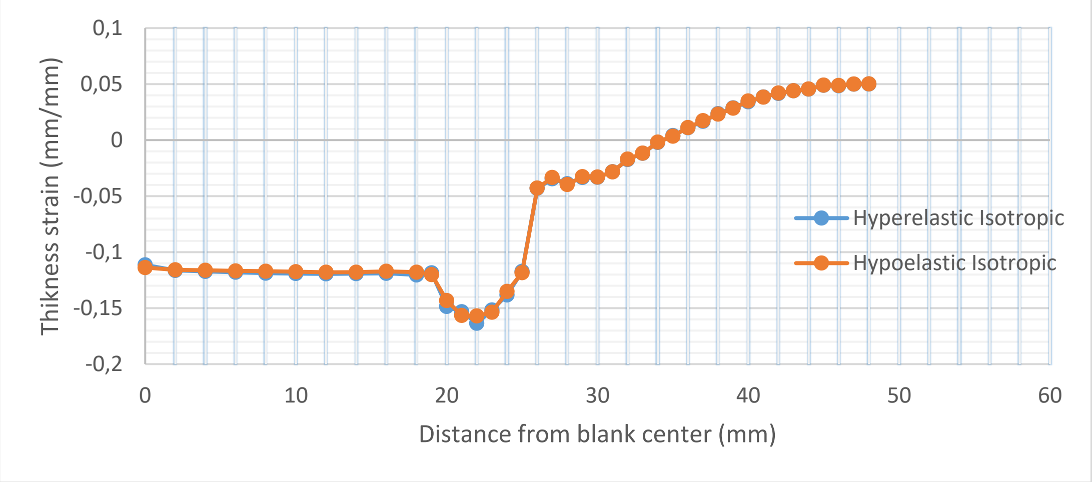

Figure 6.3. Thickness strain distributions estimated by hyperelastic and hypoelastic isotropic hardening models (20 mm punch displacement, cylindrical, SS304)

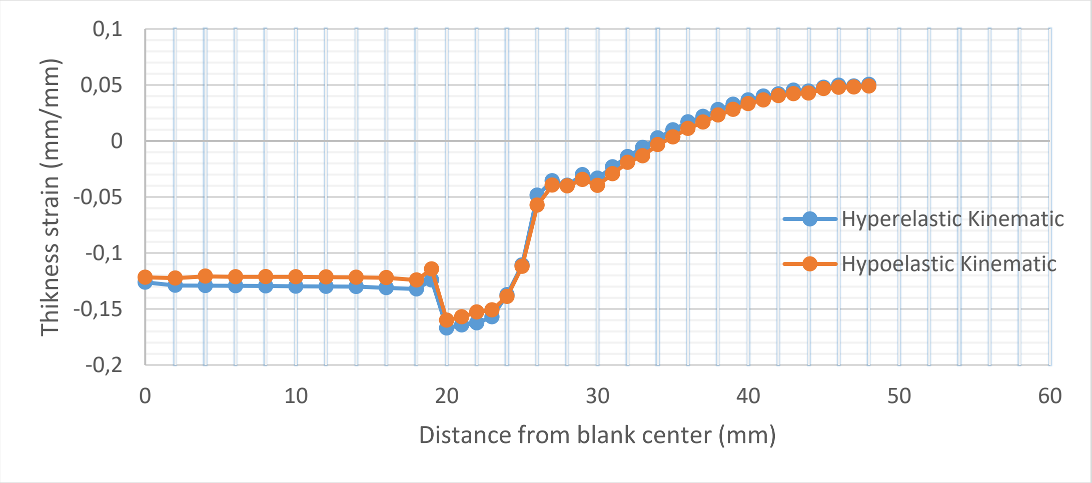

Figure 6.4. Thickness strain distributions estimated by hyperelastic and hypoelastic kinematic hardening models (20 mm punch displacement, cylindrical, SS304)

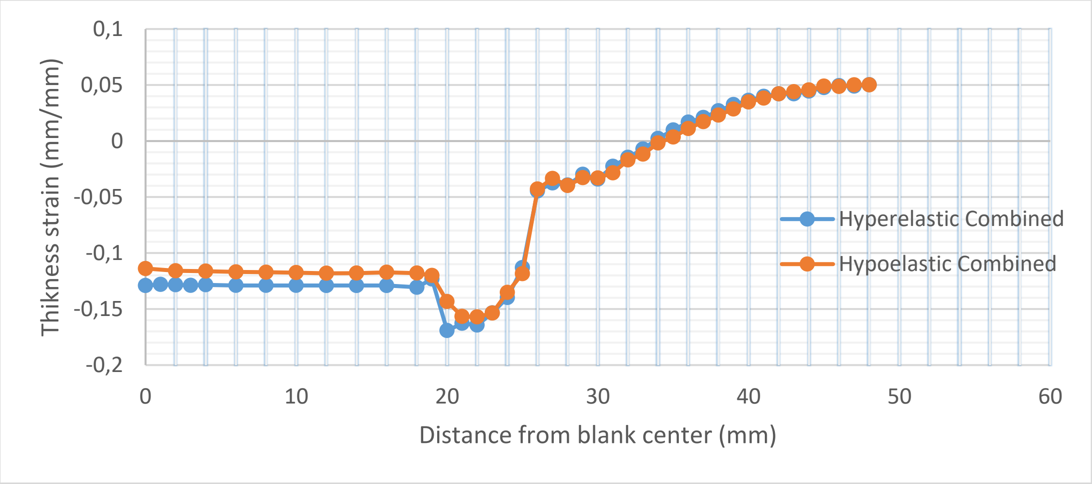

Figure 6.5 Thickness strain distributions estimated by hyperelastic and hypoelastic combined hardening models (20 mm punch displacement, cylindrical, SS304)

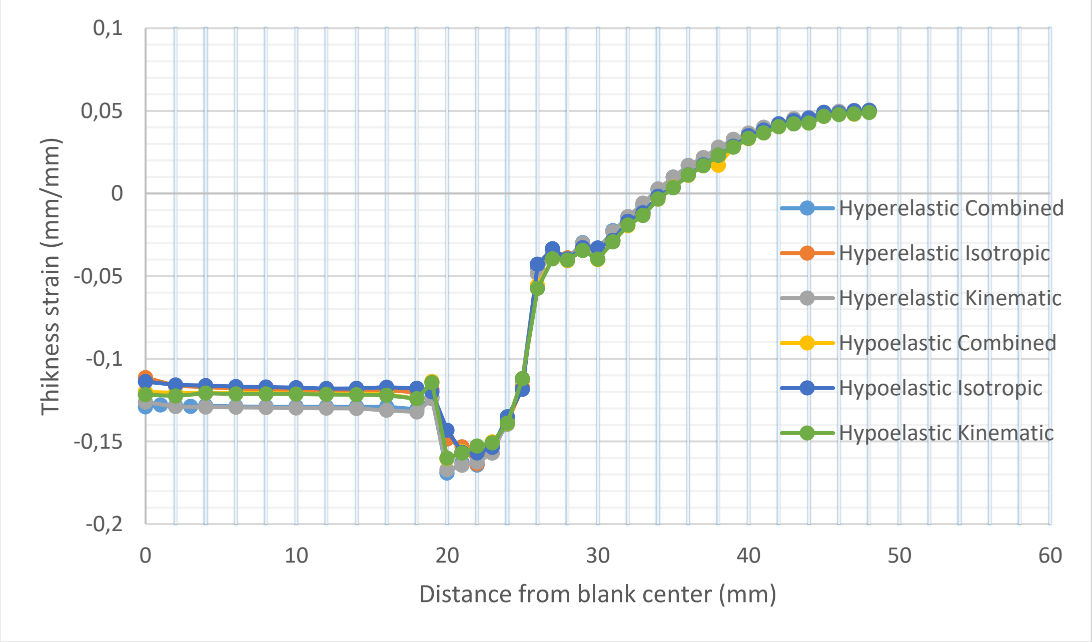

Figure 6.6 Comparison of all of the results (20 mm punch displacement, cylindrical, SS304)

At 20 mm punch displacement hypoelastic based and hyperelastic based materials give close results to each other. Slight differences in results can be seen towards the sheet center for kinematic and combined hardening cases, but towards the mid and edge of the sheets results become very close. Results come out to be similar to each other for different hardening models as well. Again, small differences present towards to center of the sheet.

6.2.1.2. 35 mm Punch Displacement

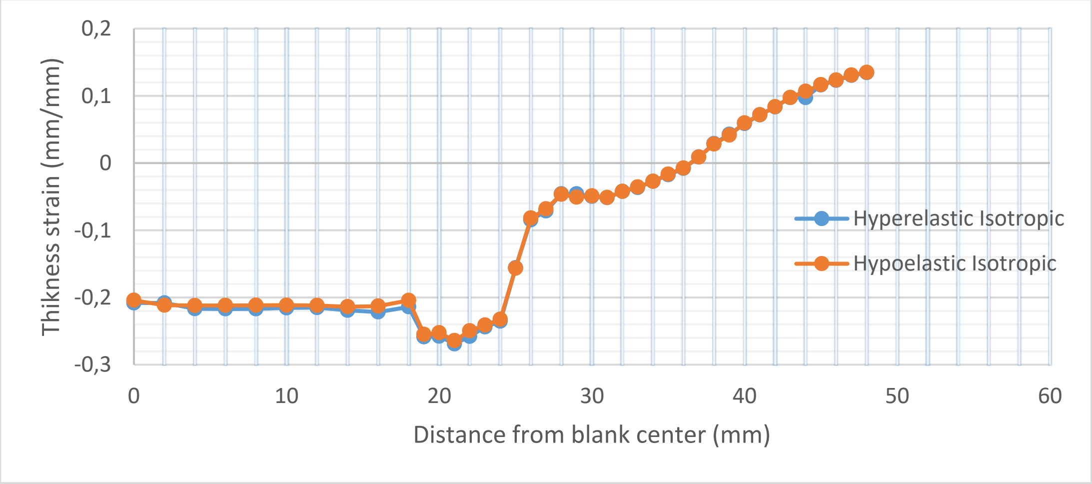

Figure 6.7. Thickness strain distributions estimated by hyperelastic and hypoelastic isotropic hardening models (35 mm punch displacement, cylindrical, SS304)

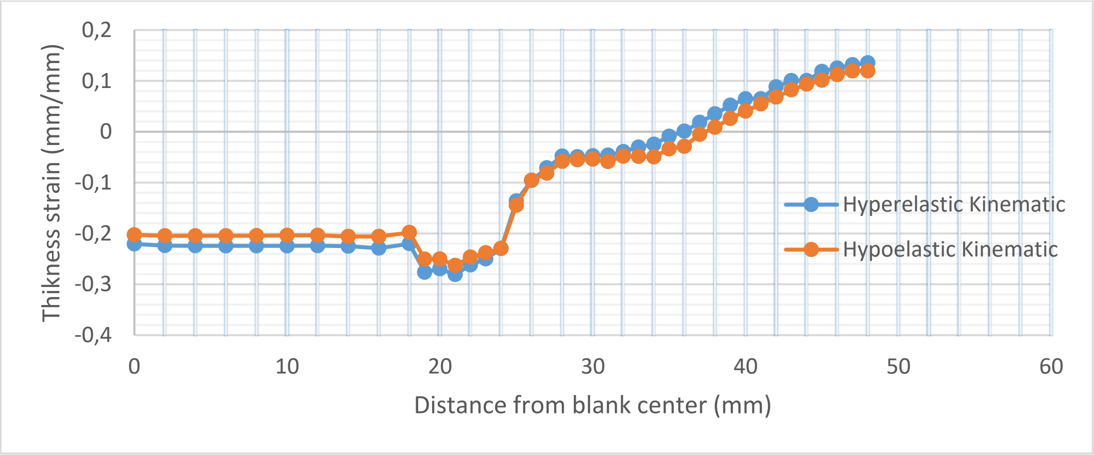

Figure 6.8. Thickness strain distributions estimated by hyperelastic and hypoelastic kinematic hardening models (35 mm punch displacement, cylindrical, SS304)

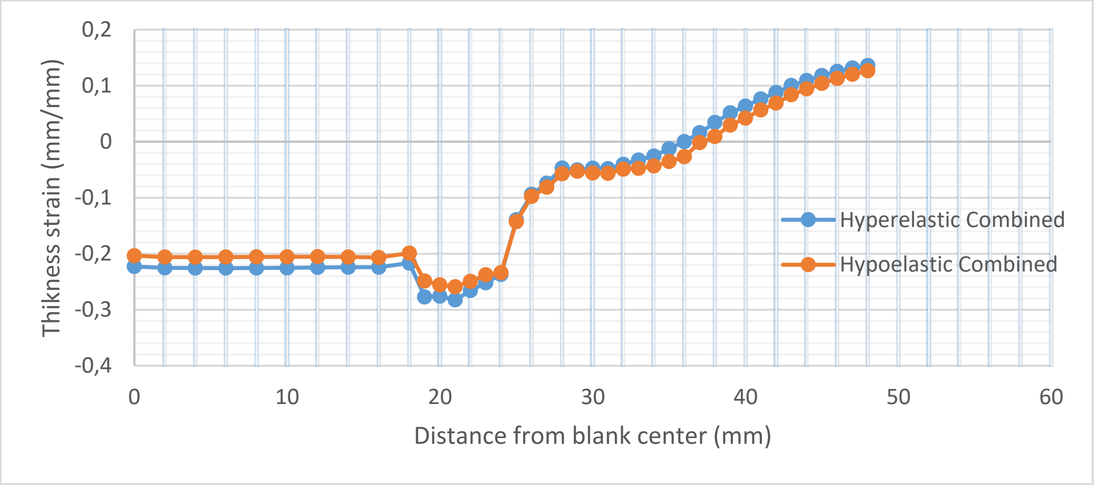

Figure 6.9. Thickness strain distributions estimated by hyperelastic and hypoelastic combined hardening models (35 mm punch displacement, cylindrical, SS304)

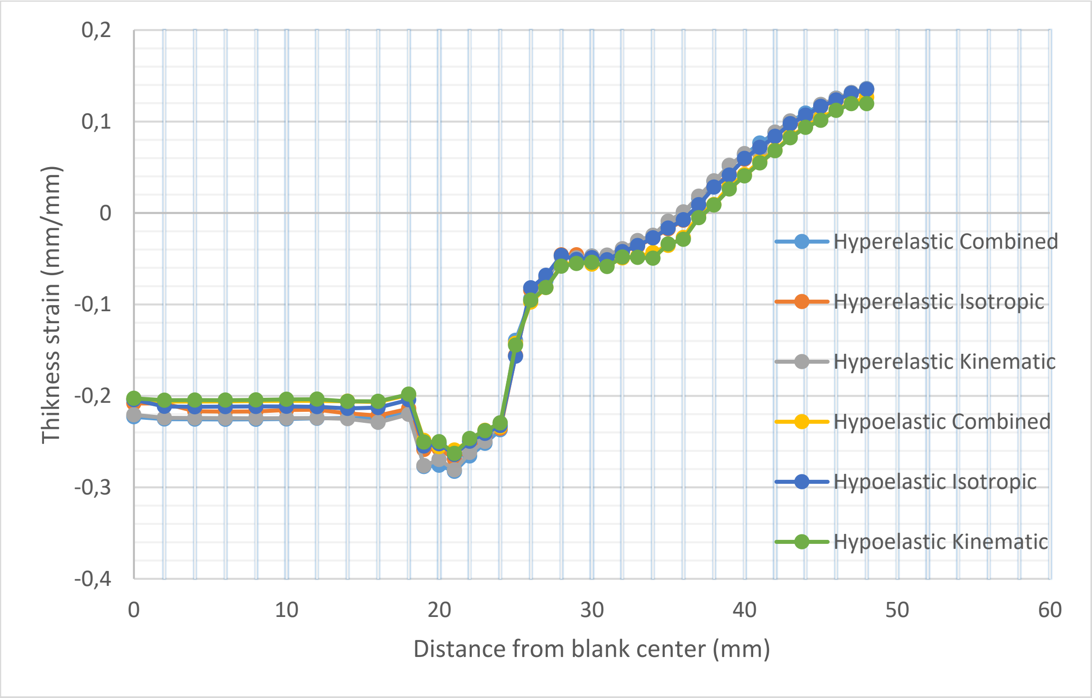

Figure 6.10. Comparison of all of the results (35 mm punch displacement, cylindrical, SS304)

Similar trends can be seen for 35 mm punch displacement except this time small differences in the results obtained emerge towards the edge of the sheet for hypoelastic and hyperelastic cases having combined and kinematic hardening models. In the case of isotropic hardening results still does not differ even slightly.

6.2.1.3. 45 mm Punch Displacement

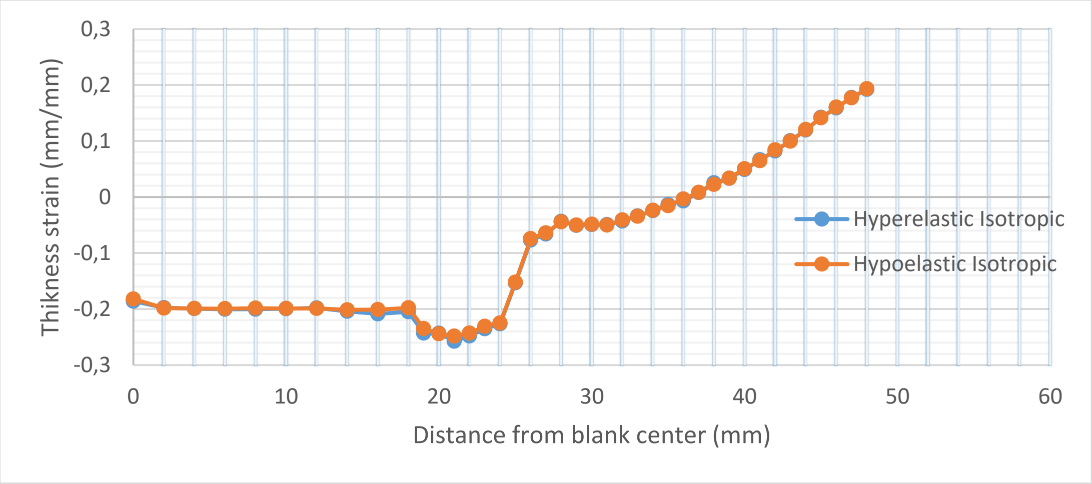

Figure 6.11. Thickness strain distributions estimated by hyperelastic and hypoelastic isotropic hardening models (45 mm punch displacement, cylindrical, SS304)

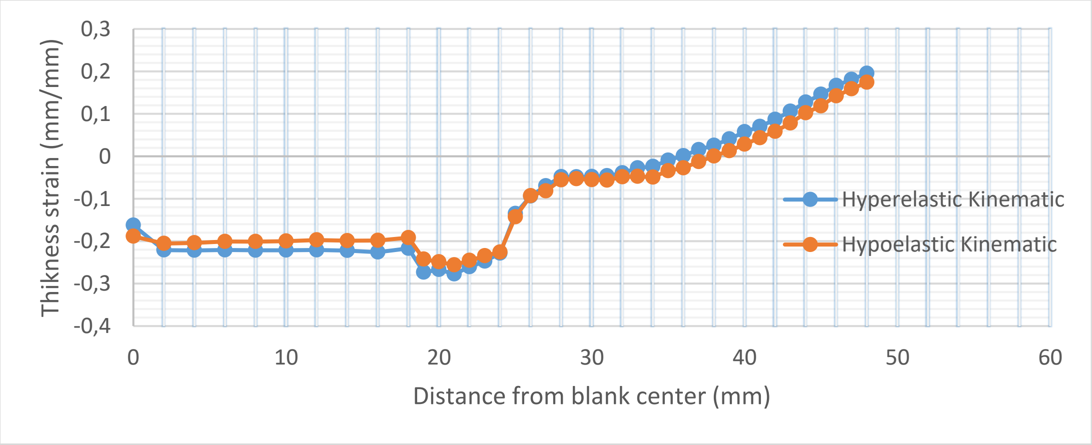

Figure 6.12. Thickness strain distributions estimated by hyperelastic and hypoelastic kinematic hardening models (45 mm punch displacement, cylindrical, SS304)

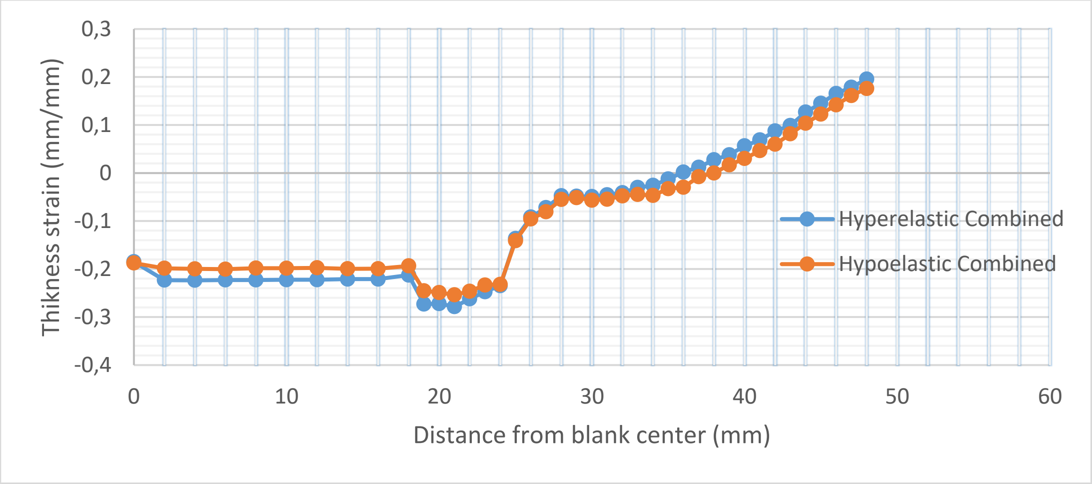

Figure 6.13. Thickness strain distributions estimated by hyperelastic and hypoelastic combined hardening models (45 mm punch displacement, cylindrical, SS304)

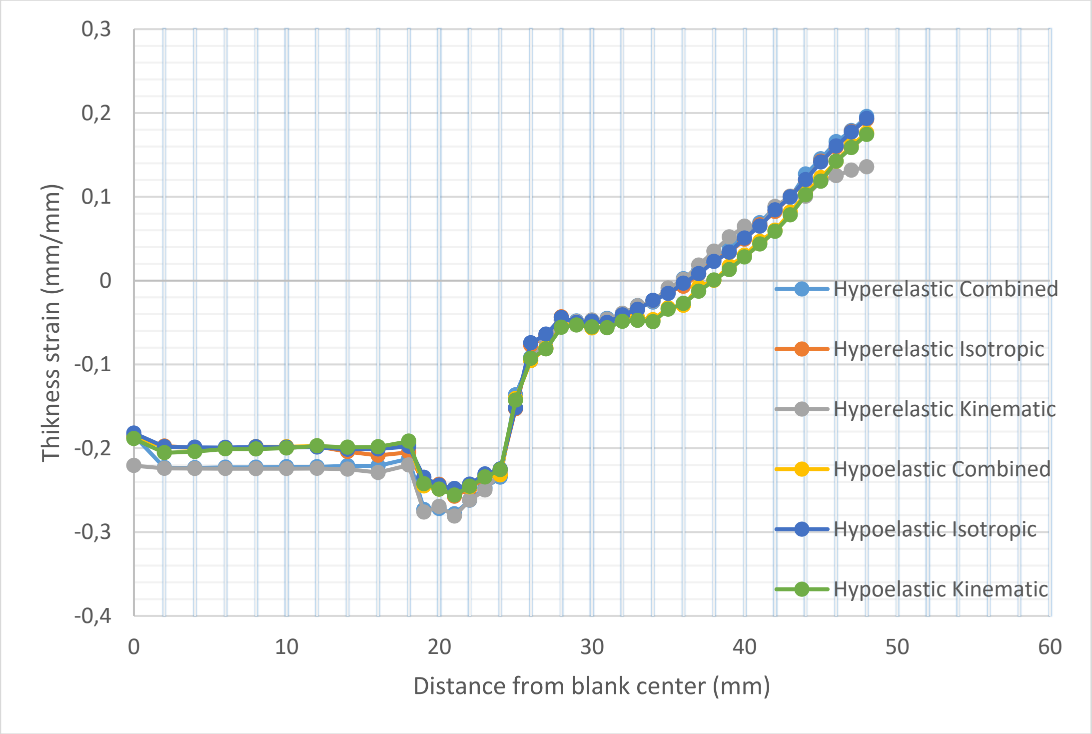

Figure 6.14 Comparison of all of the results (45 mm punch displacement, cylindrical SS304)

The results at 45 mm punch displacement is almost same as the results of 35 mm punch displacement. Identical comments can be made for this case.

6.2.2. Square Cup Drawing Results

Thickness strain distributions of material models at different punch displacements for square cup drawing of SS304 material is presented in this section.

6.2.2.1. 15 mm Punch Displacement - Rolling Direction

The results in rolling direction is presented in figures 6.15-6.18.

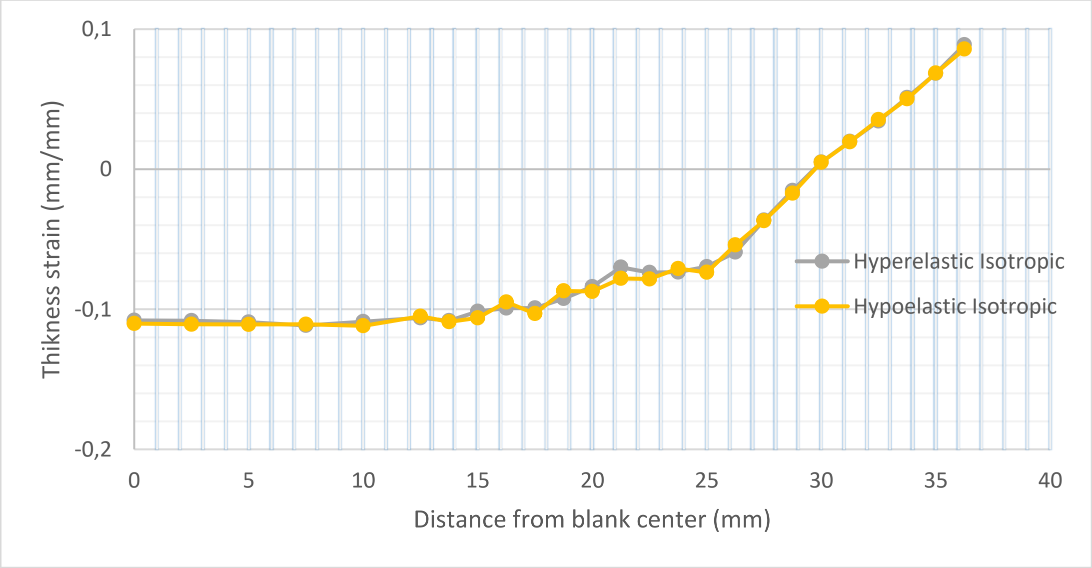

Figure 6.15 Thickness strain distributions estimated by hyperelastic and hypoelastic isotropic hardening models in rolling direction (15 mm punch displacement, square, SS304)

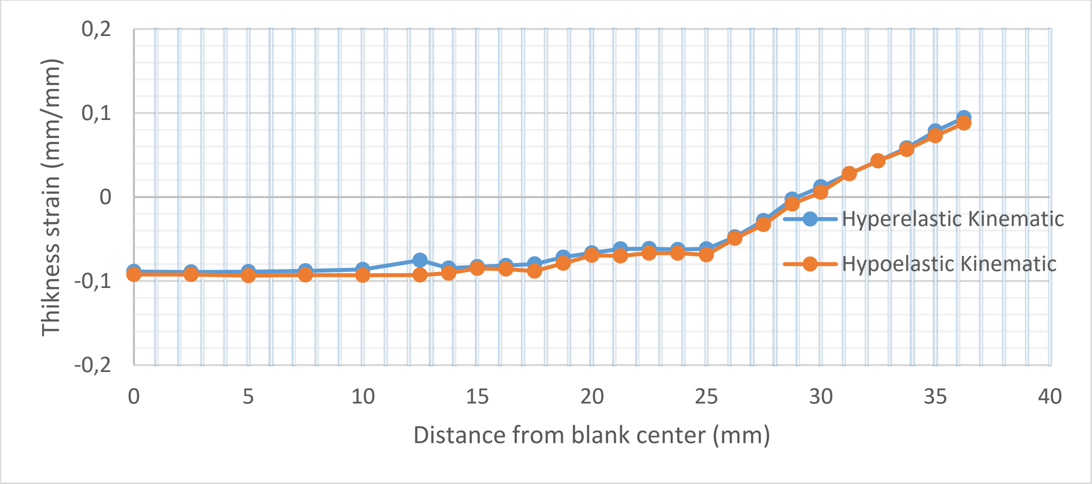

Figure 6.16 Thickness strain distributions estimated by hyperelastic and hypoelastic kinematic hardening models in rolling direction (15 mm punch displacement, square, SS304)

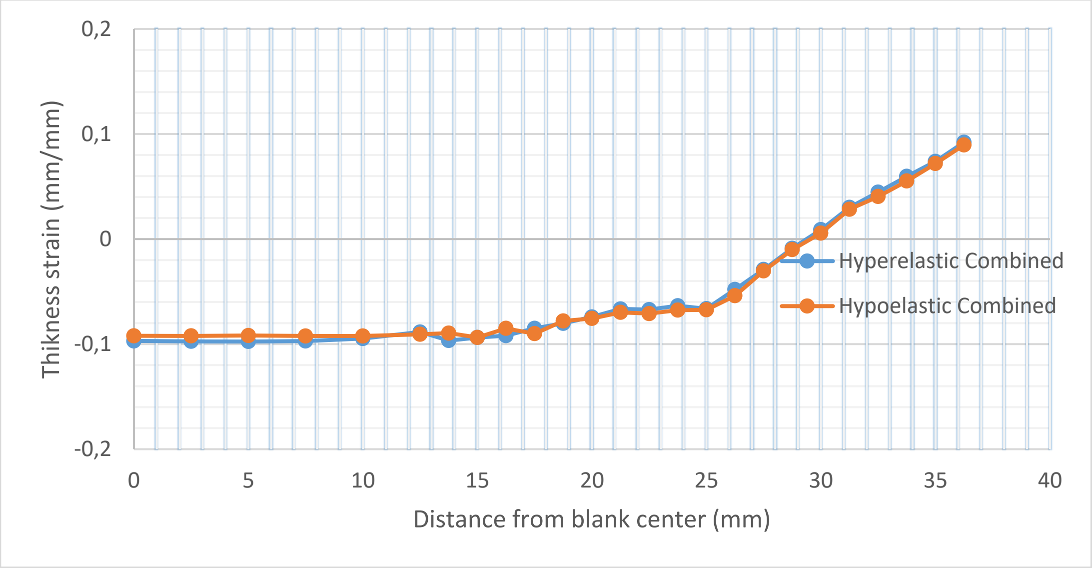

Figure 6.17. Thickness strain distributions estimated by hyperelastic and hypoelastic combined hardening models in rolling direction (15 mm punch displacement, square, SS304)

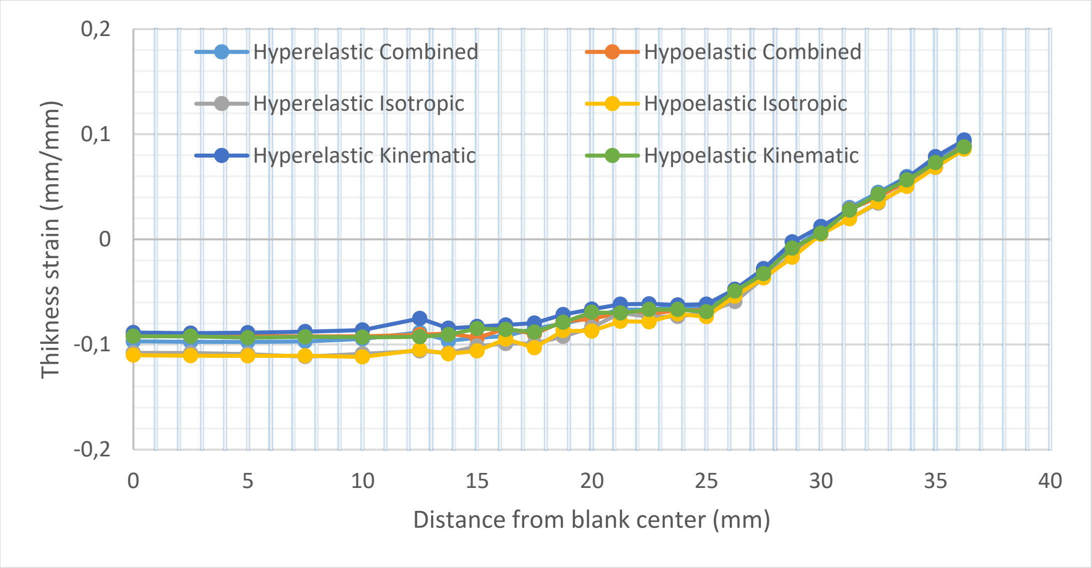

Figure 6.18 Comparison of all of the results in rolling direction (15 mm punch displacement, square, SS304)

For rolling direction, thickness strains estimated by hyperelastic and hypoelastic models are in agreement throughout the sheet except some local deviations.

6.2.2.2. 15 mm Punch Displacement - Diagonal Direction

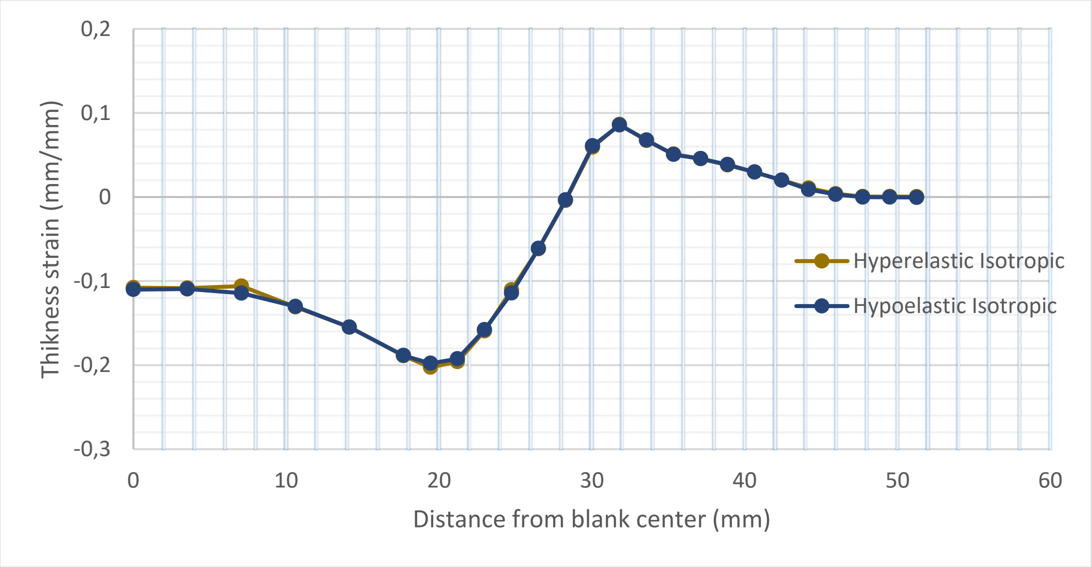

Figure 6.19 Thickness strain distributions estimated by hyperelastic and hypoelastic isotropic hardening models in diagonal direction (15 mm punch displacement, square, SS304)

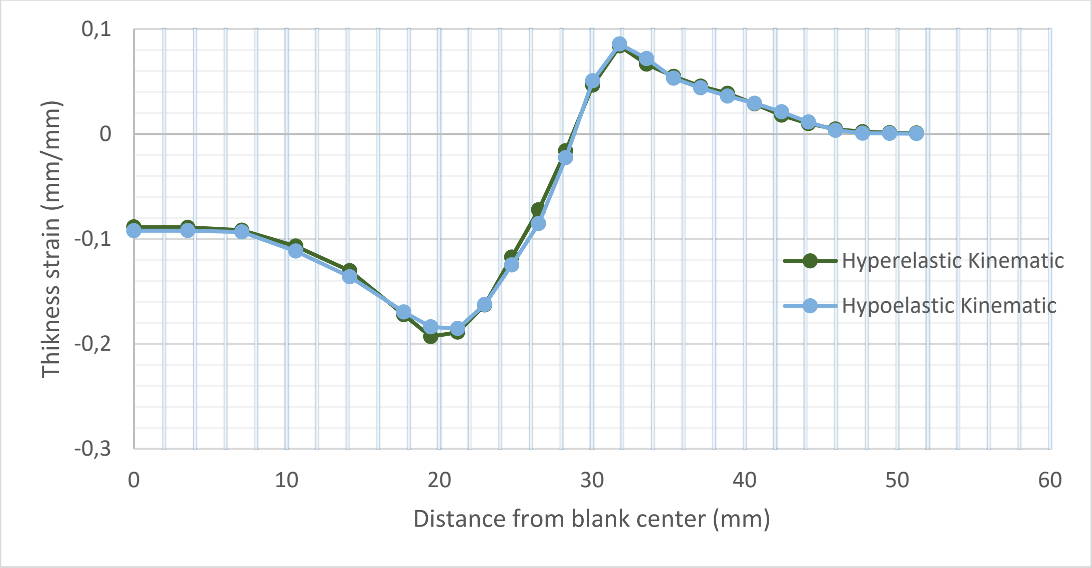

Figure 6.20 Thickness strain distributions estimated by hyperelastic and hypoelastic kinematic hardening models in diagonal direction (15 mm punch displacement, square, SS304)

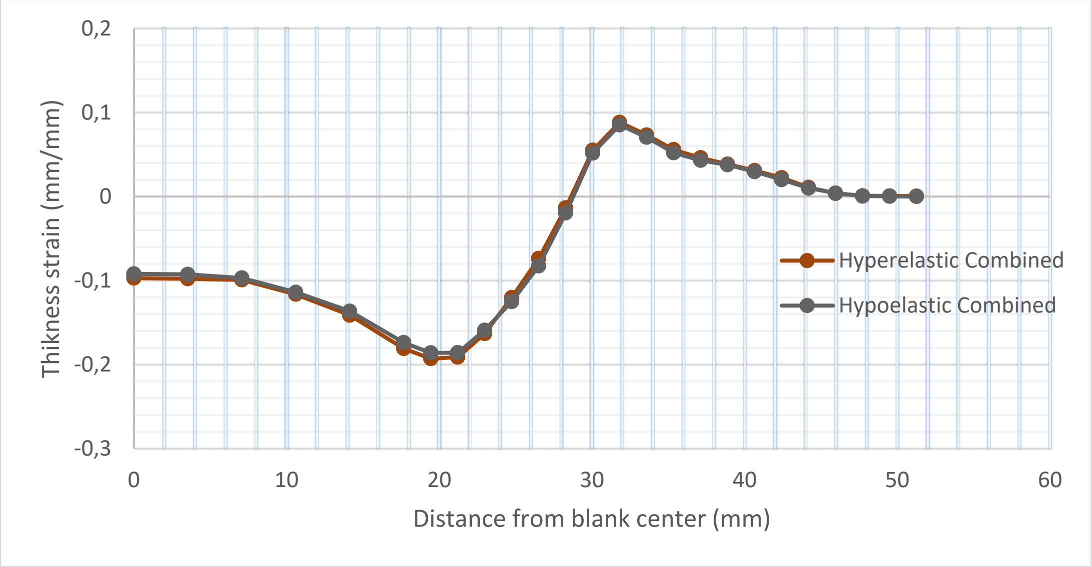

Figure 6.21. Thickness strain distributions estimated by hyperelastic and hypoelastic combined hardening models in diagonal direction (15 mm punch displacement, square, SS304)

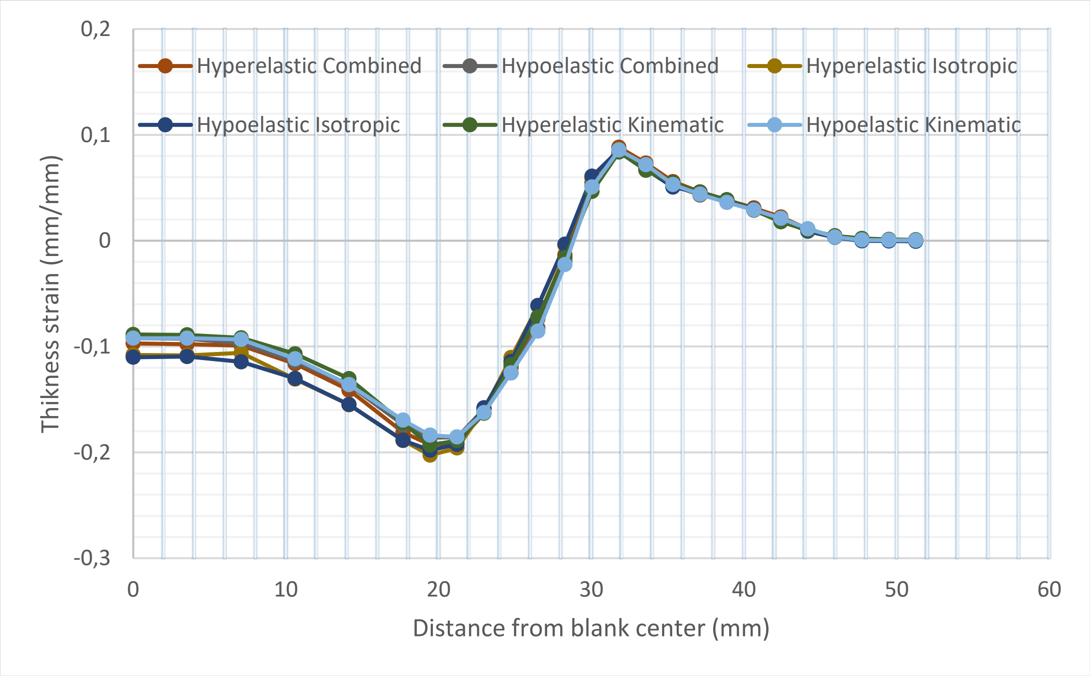

Figure 6.22 Comparison of all of the results in diagonal direction (15 mm punch displacement, square, SS304)

In diagonal direction thickness strains estimated by hyperelastic and hypoelastic models are in almost total agreement throughout the sheet.

6.2.2.3. 20 mm Punch Displacement - Rolling Direction

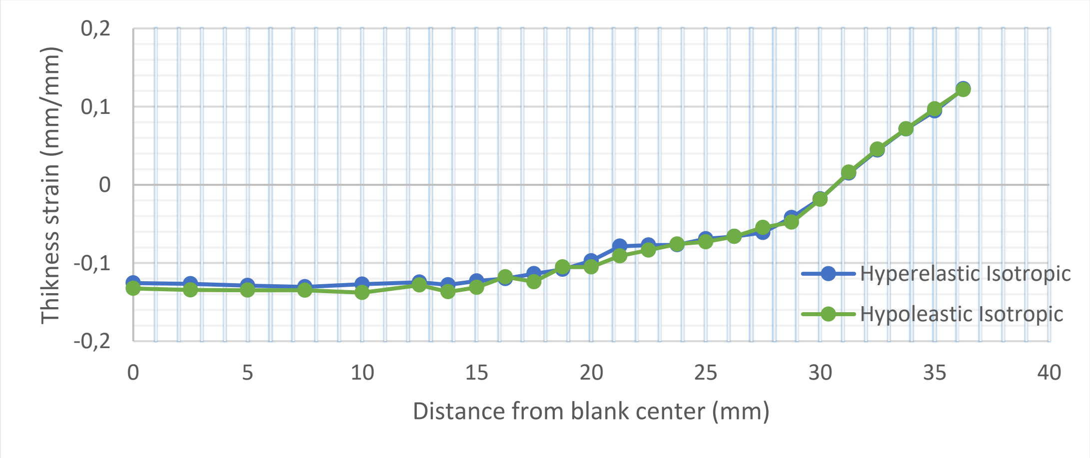

Figure 6.23. Thickness strain distributions estimated by hyperelastic and hypoelastic isotropic hardening models in rolling direction (20 mm punch displacement, square, SS304)

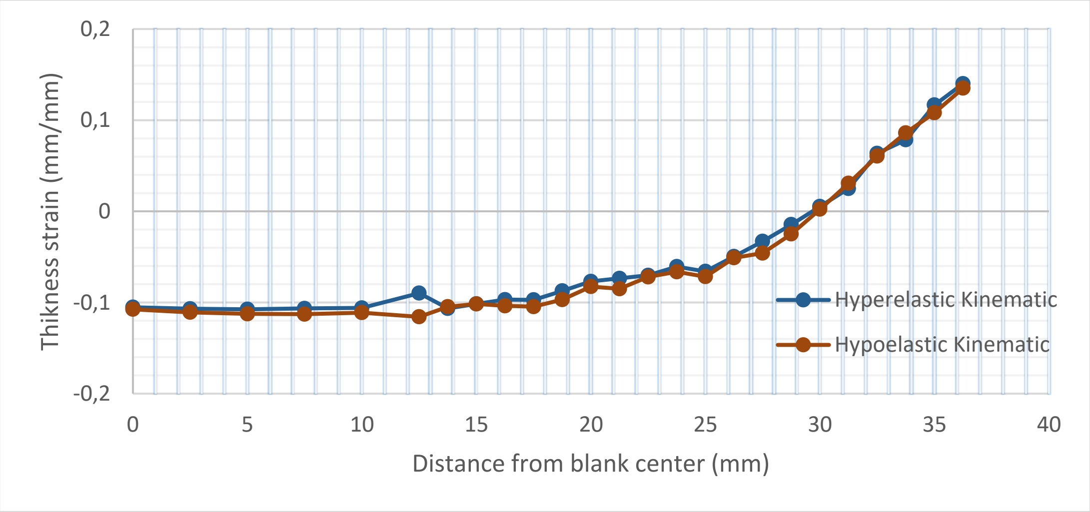

Figure 6.24 Thickness strain distributions estimated by hyperelastic and hypoelastic kinematic hardening models in rolling direction (20 mm punch displacement, square, SS304)

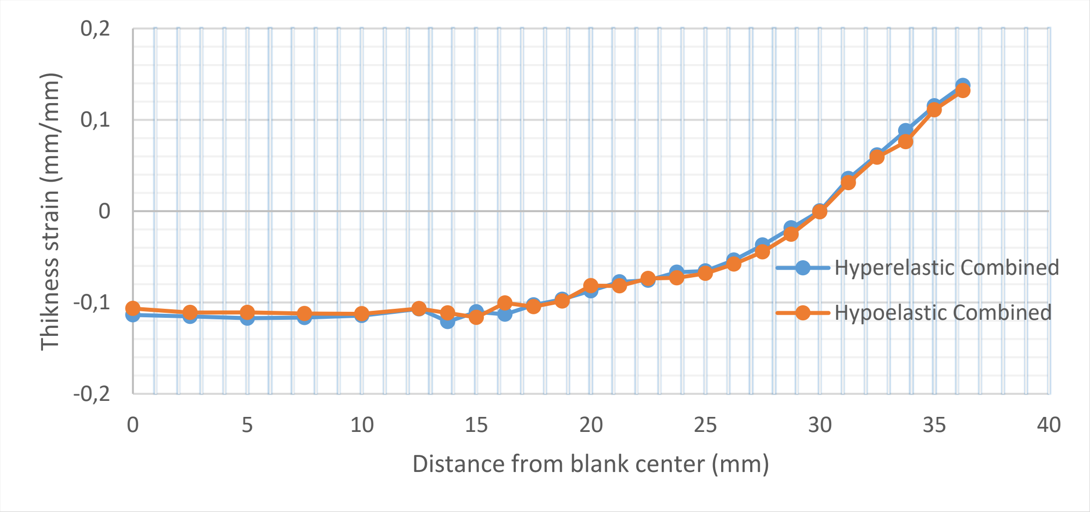

Figure 6.25. Thickness strain distributions estimated by hyperelastic and hypoelastic combined hardening models in diagonal direction (20 mm punch displacement, square, SS304)

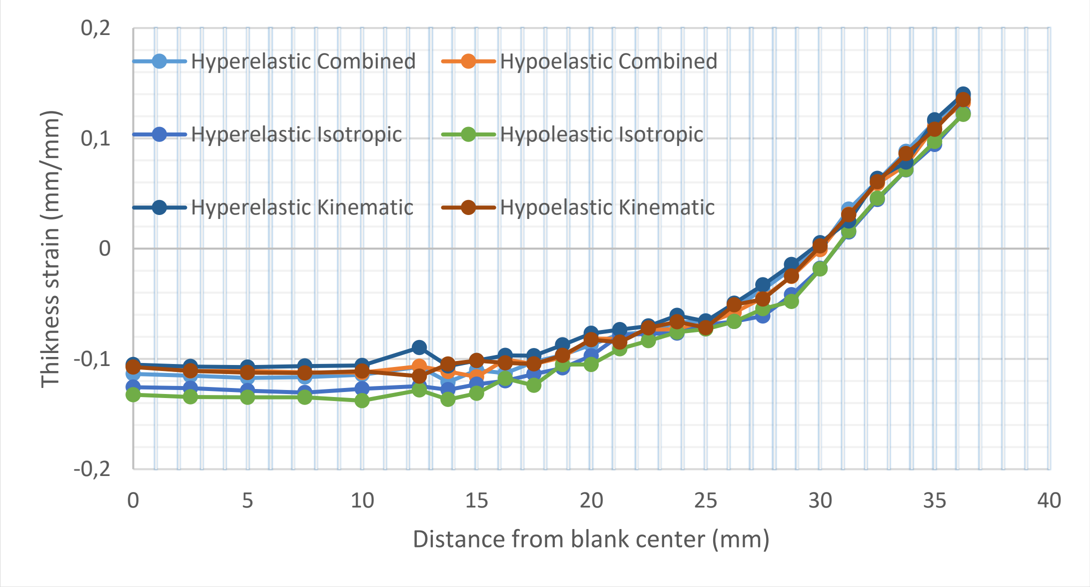

Figure 6.26 Comparison of all of the results (20 mm punch displacement, square, SS304)

At 20 mm punch displacement slightly more deviation in the simulation results of hyperelastic and hypoelastic based models are present especially for isotropic and kinematic hardening models around halfway distance from the sheet center to the edge of the sheet.

6.2.2.4. 20 mm Punch Displacement - Diagonal Direction

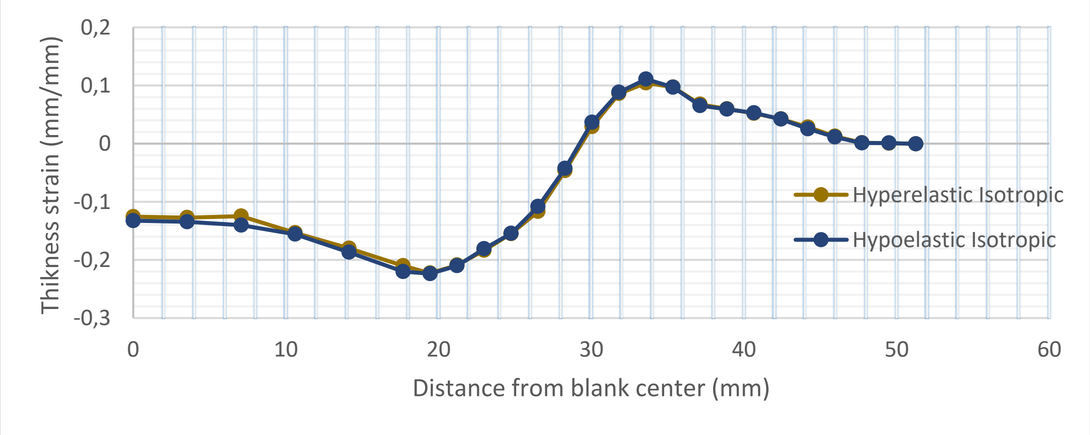

Figure 6.27 Thickness strain distributions estimated by hyperelastic and hypoelastic isotropic hardening models in diagonal direction (20 mm punch displacement, square, SS304)

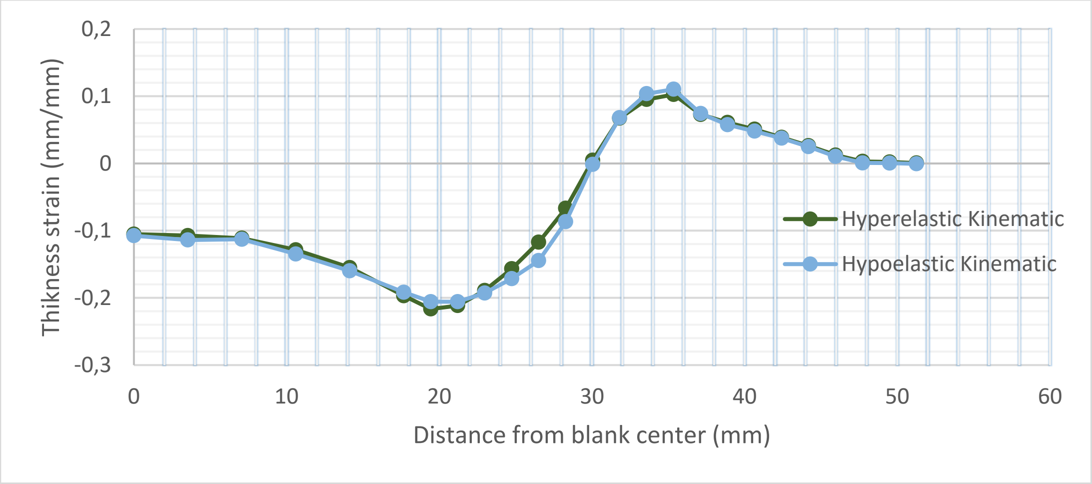

Figure 6.28 Thickness strain distributions estimated by hyperelastic and hypoelastic kinematic hardening models in diagonal direction (20 mm punch displacement, square, SS304)

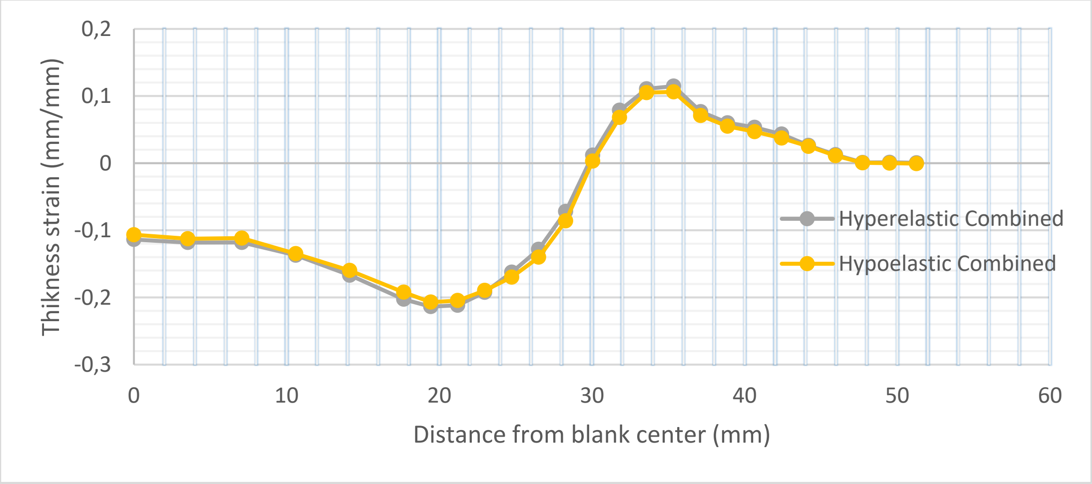

Figure 6.29. Thickness strain distributions estimated by hyperelastic and hypoelastic combined hardening models in diagonal direction (20 mm punch displacement, square, SS304)

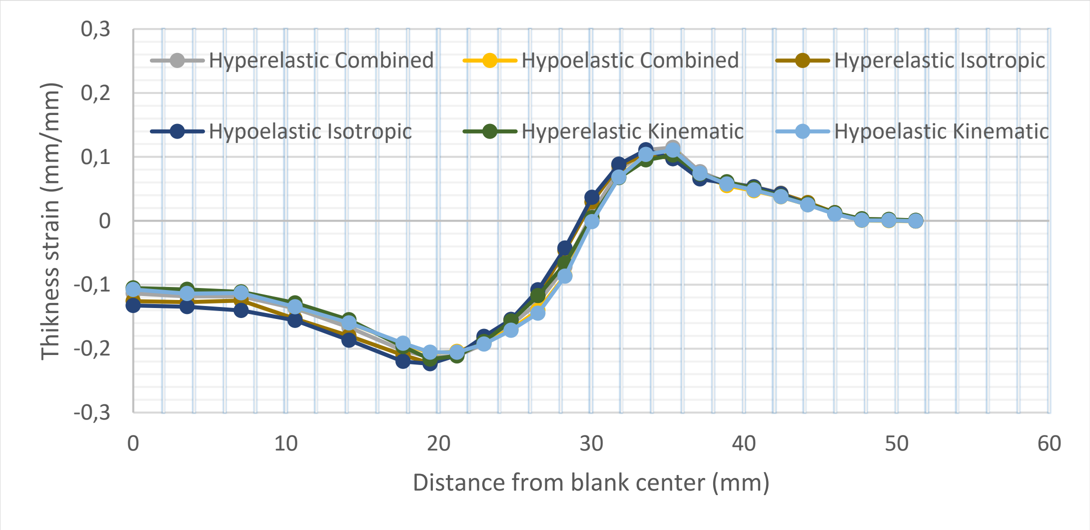

Figure 6.30. Comparison of all of the results in diagonal direction (20 mm punch displacement, square, SS304)

Again, better correlation between hyperelastic and hypoelastic based models exist in diagonal direction of the sheet. Slight local differences at points 7 mm from center for isotropic hardening models and at around 27 mm for kinematic hardening model can be seen.

6.2.2.5. 25 mm Punch Displacement - Rolling Direction

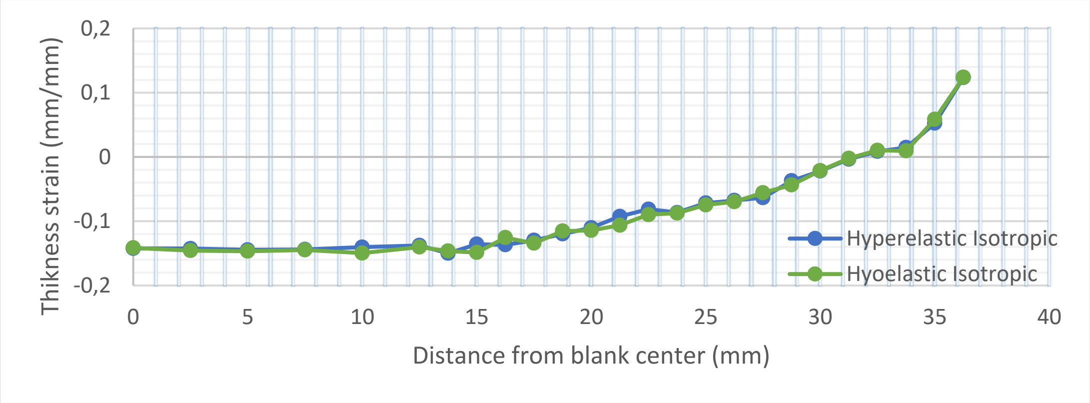

Figure 6.31 Thickness strain distributions estimated by hyperelastic and hypoelastic isotropic hardening models in rolling direction (25 mm punch displacement, square, SS304)

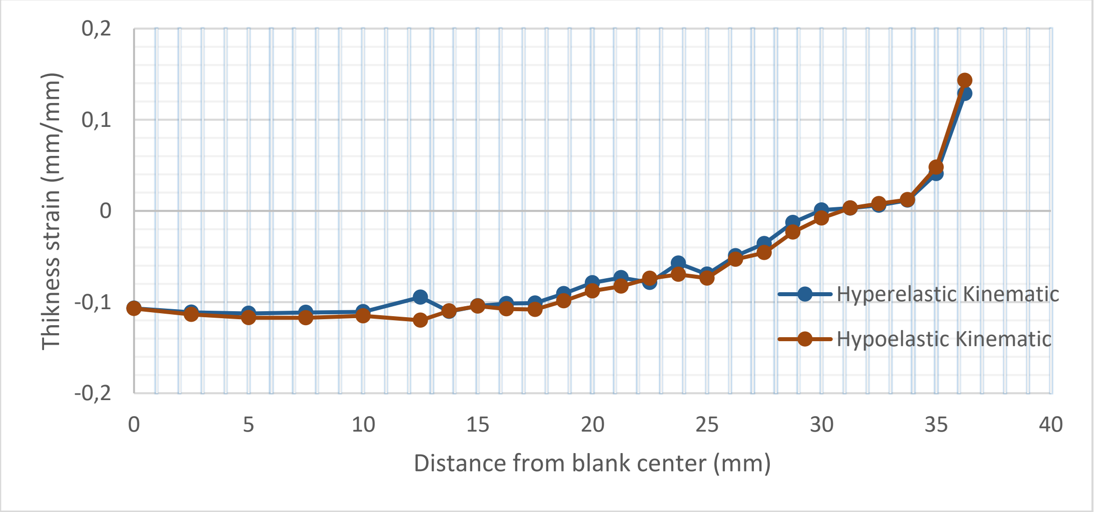

Figure 6.32 Thickness strain distributions estimated by hyperelastic and hypoelastic kinematic hardening models in rolling direction (25 mm punch displacement, square, SS304)

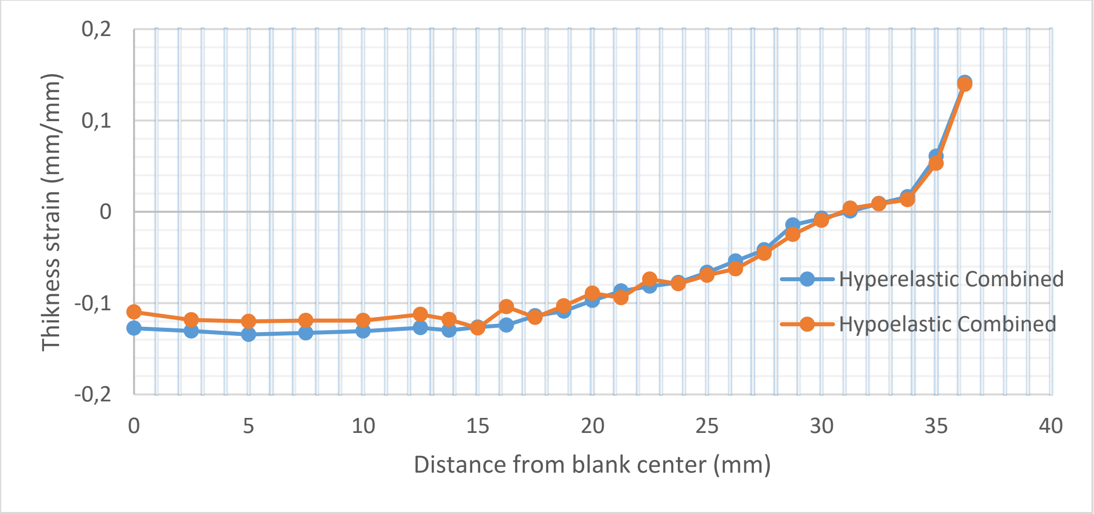

Figure 6.33 Thickness strain distributions estimated by hyperelastic and hypoelastic combined hardening models in rolling direction (25 mm punch displacement, square, SS304)

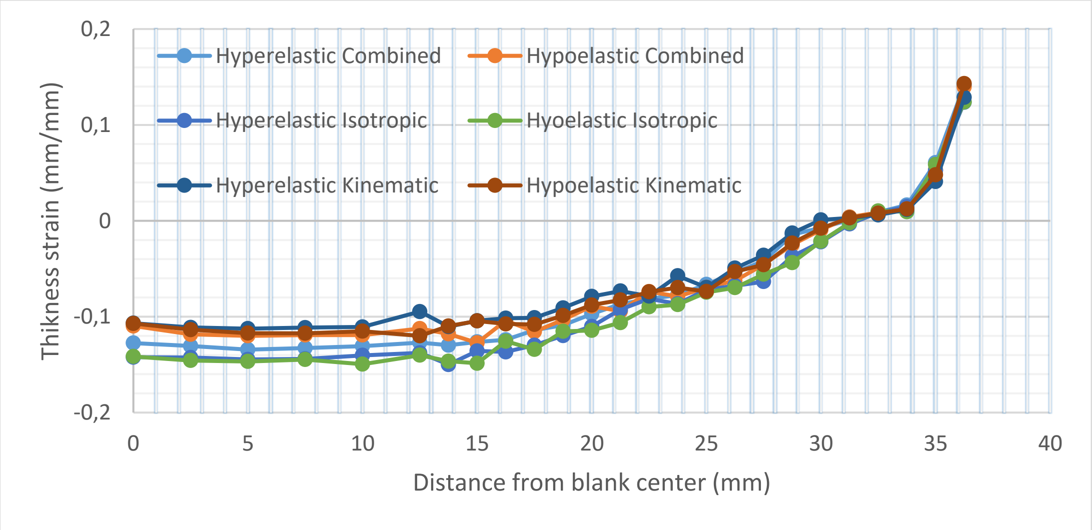

Figure 6.34 Comparison of all of the results in rolling direction (25 mm punch displacement, square, SS304)

Some little differences present for 25 mm punch displacement as well, between hyperelastic and hypoelastic based models. Differences stand out towards the center of the sheet for combined hardening models and towards the midway for isotropic and kinematic hardening models.

6.2.2.6. 25 mm Punch Displacement - Rolling Direction

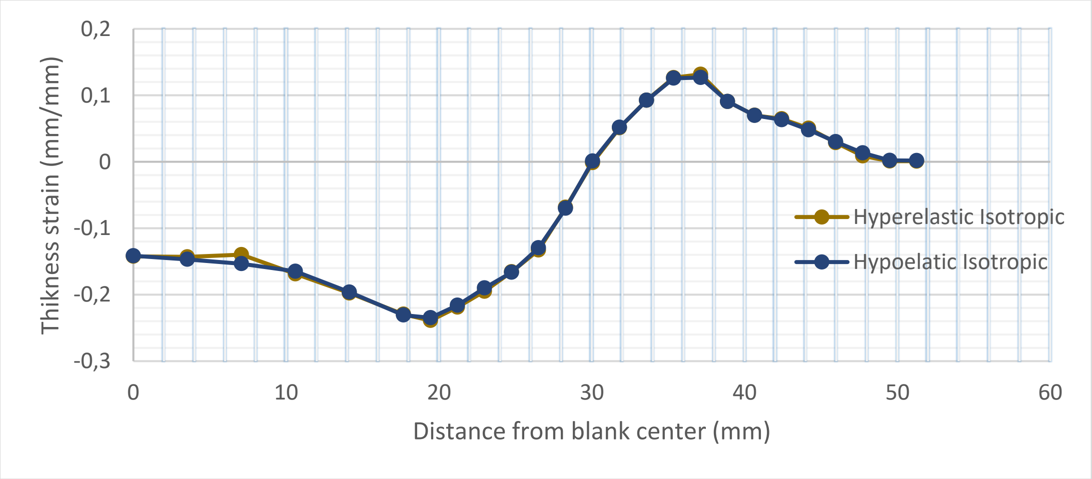

Figure 6.35 Thickness strain distributions estimated by hyperelastic and hypoelastic isotropic hardening models in diagonal direction (25 mm punch displacement, square, SS304)

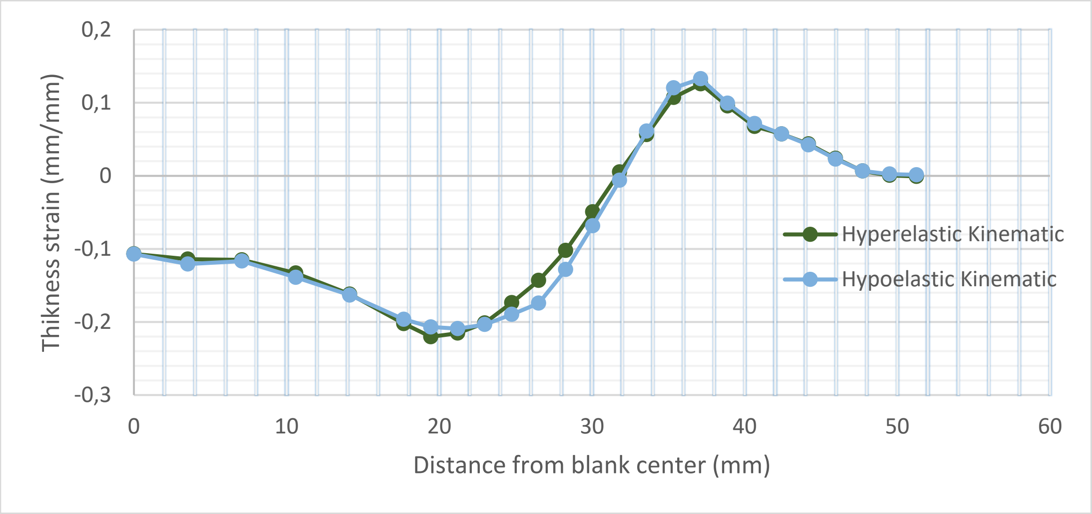

Figure 6.36 Thickness strain distributions estimated by hyperelastic and hypoelastic kinematic hardening models in diagonal direction (25 mm punch displacement, square, SS304)

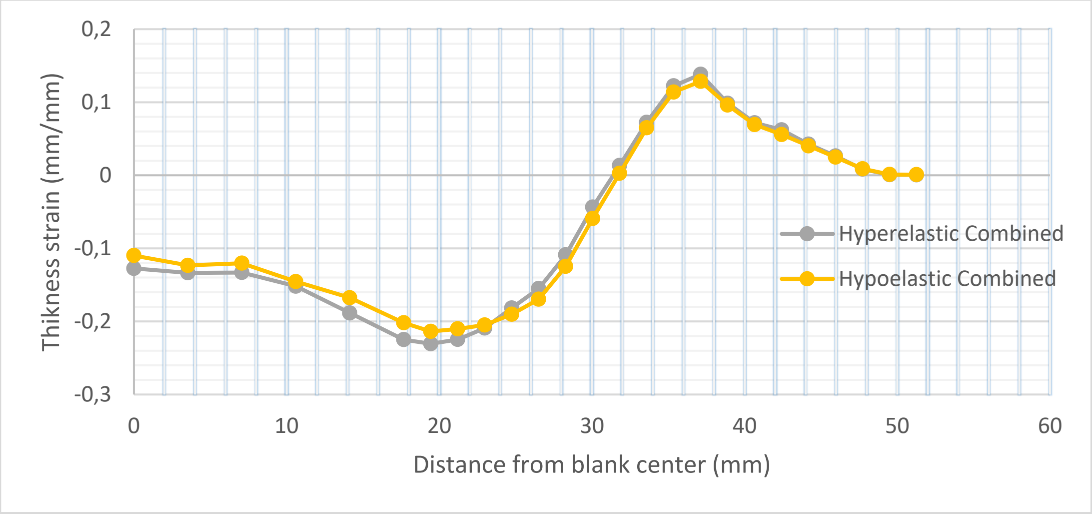

Figure 6.37 Thickness strain distributions estimated by hyperelastic and hypoelastic combined hardening models in diagonal direction (25 mm punch displacement, square, SS304)

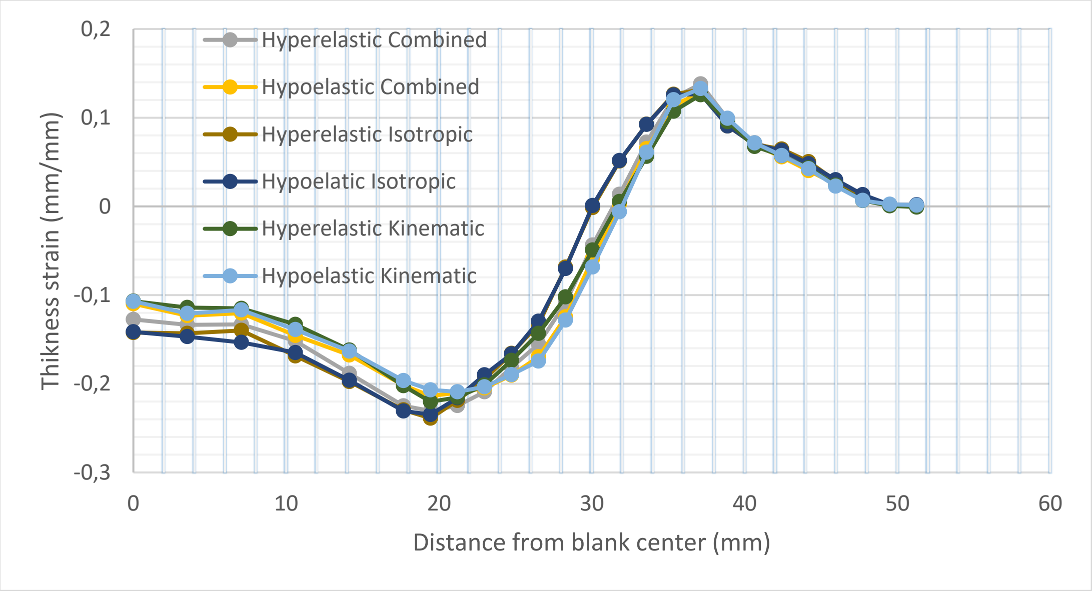

Figure 6.38 Comparison of all of the results in diagonal direction (25 mm punch displacement, square, SS304)

In diagonal direction, closer results are obtained for 25 mm punch displacement as well. Slight thickness strain differences emerge at around 15 mm distance from midpoint for combined hardening models and around 27 mm distance for kinematic hardening models.

6.2.3. Round Bottom Cup Drawing Results

In this section thickness strain distributions for round bottom cup drawing of SS304 material is presented.

6.2.3.1. 25 mm Punch Displacement

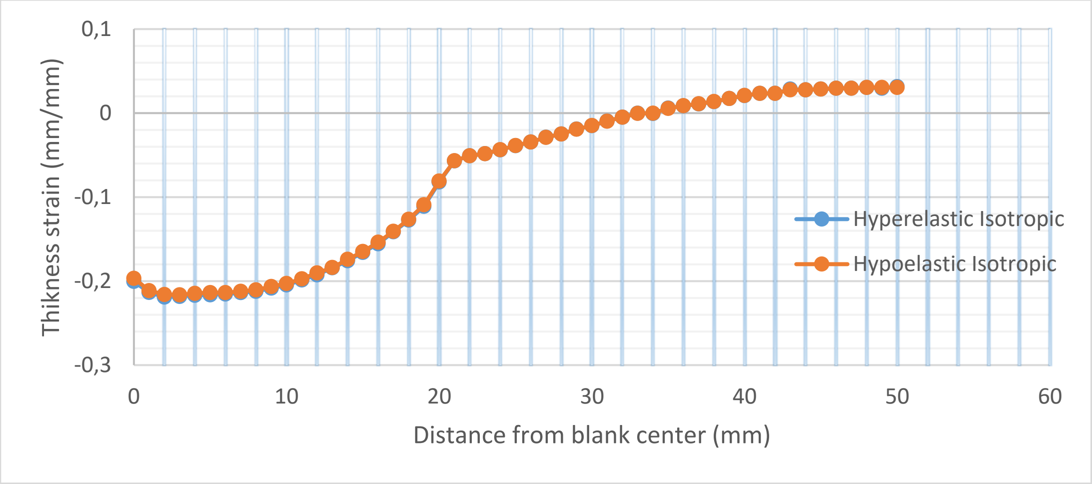

Figure 6.39 Thickness strain distributions estimated by hyperelastic and hypoelastic isotropic hardening models (25 mm punch displacement, round, SS304)

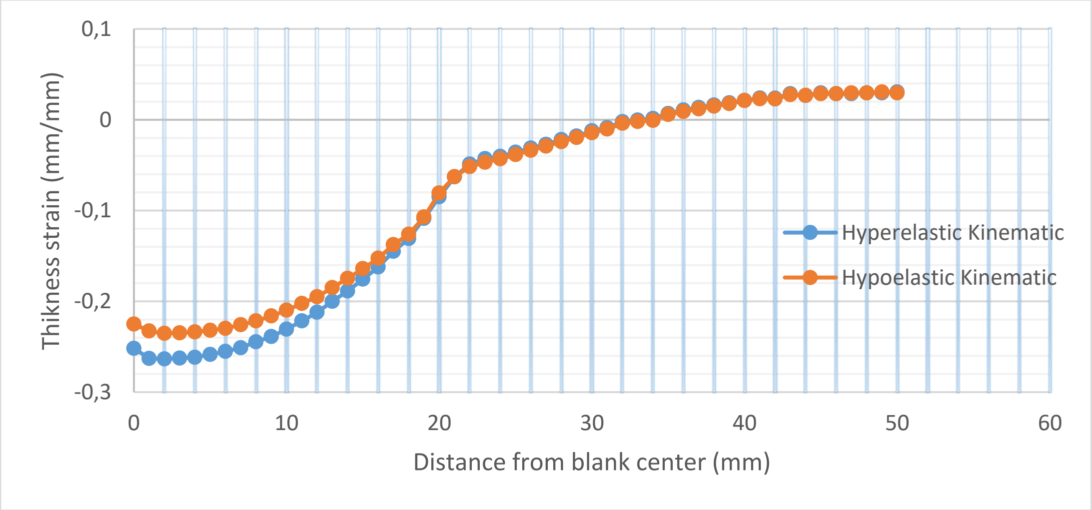

Figure 6.40 Thickness strain distributions estimated by hyperelastic and hypoelastic kinematic hardening models (25 mm punch displacement, round, SS304)

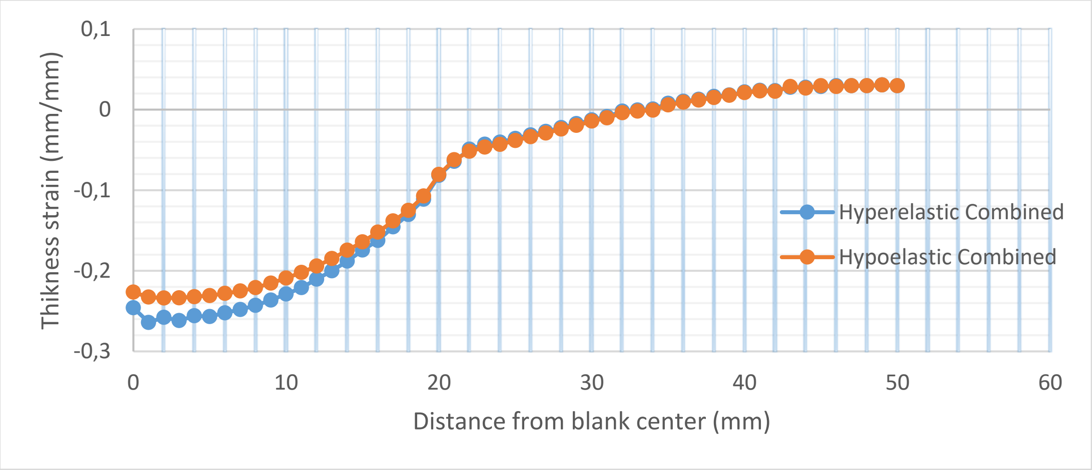

Figure 6.41 Thickness strain distributions estimated by hyperelastic and hypoelastic combined hardening models (25 mm punch displacement, round, SS304)

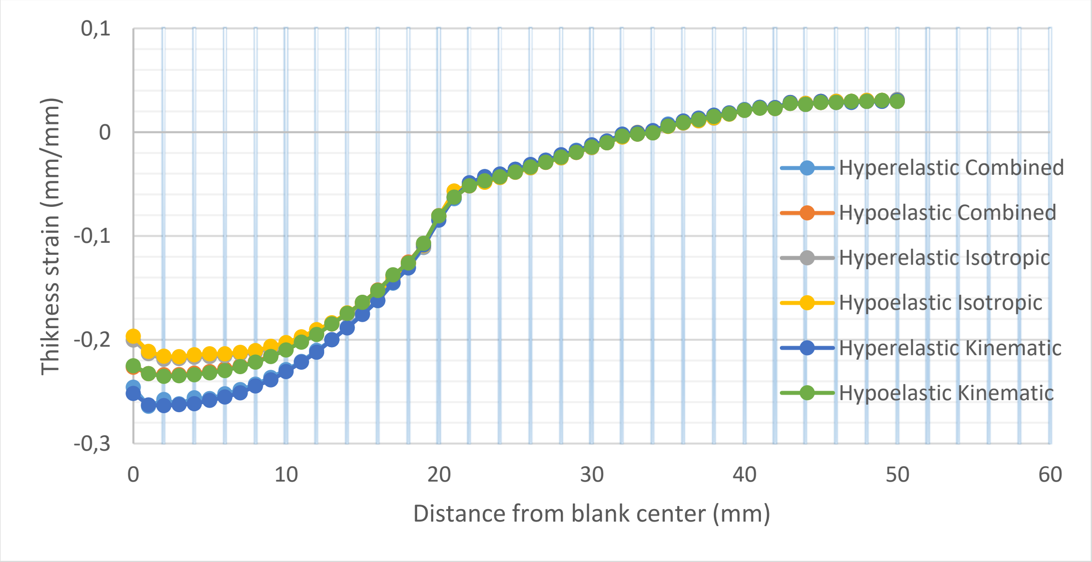

Figure 6.42 Comparison of all of the results (25 mm punch displacement, round, SS304)

Combined hardening and kinematic hardening models for hyperelastic and hypoelastic based material models show pretty large differences towards the center of the sheet for 25 mm punch displacement of round bottom cup drawing. Isotropic hardening models are in perfect agreement.

6.2.3.2. 45 mm Punch Displacement

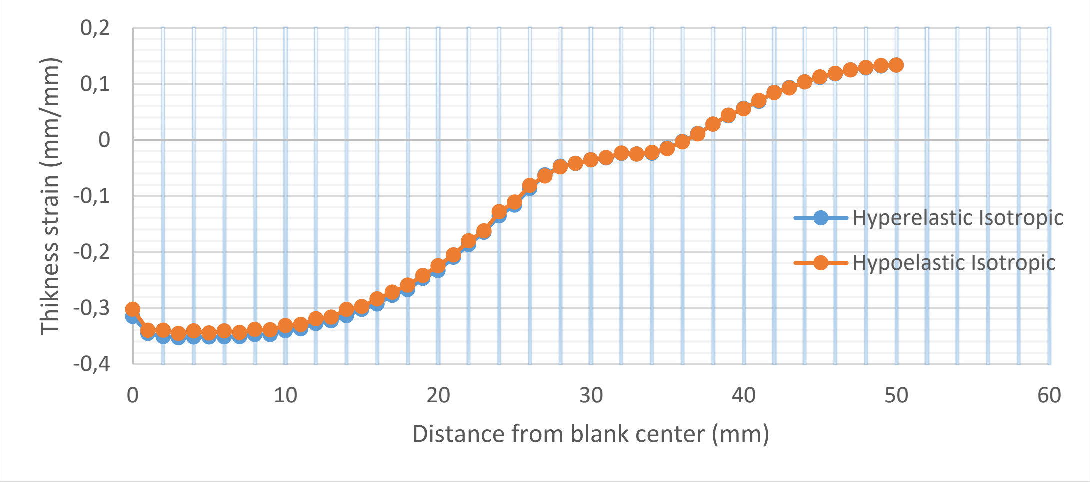

Figure 6.43 Thickness strain distributions estimated by hyperelastic and hypoelastic isotropic hardening models (45 mm punch displacement, round, SS304)

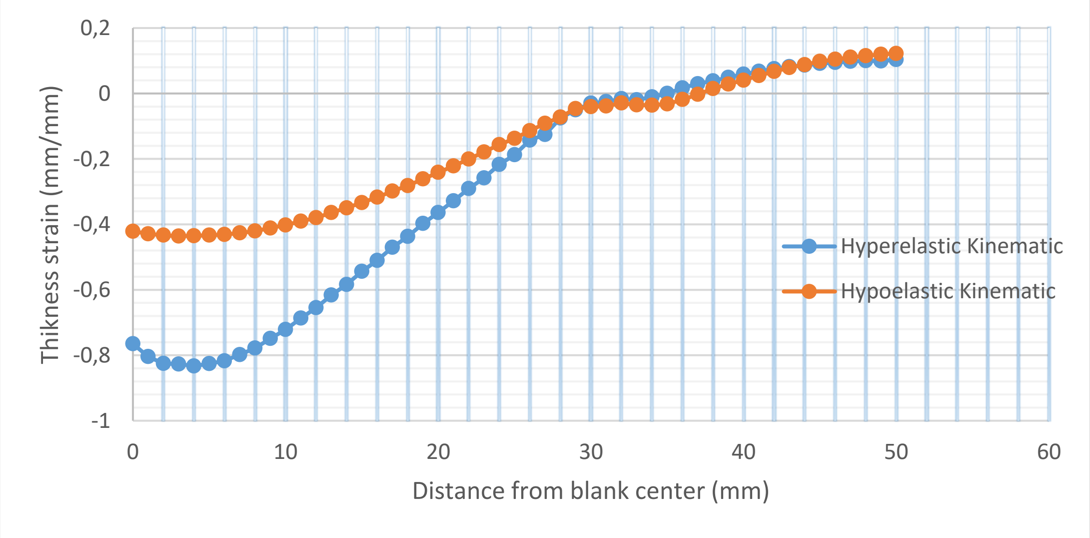

Figure 6.44 Thickness strain distributions estimated by hyperelastic and hypoelastic kinematic hardening models (45 mm punch displacement, round, SS304)

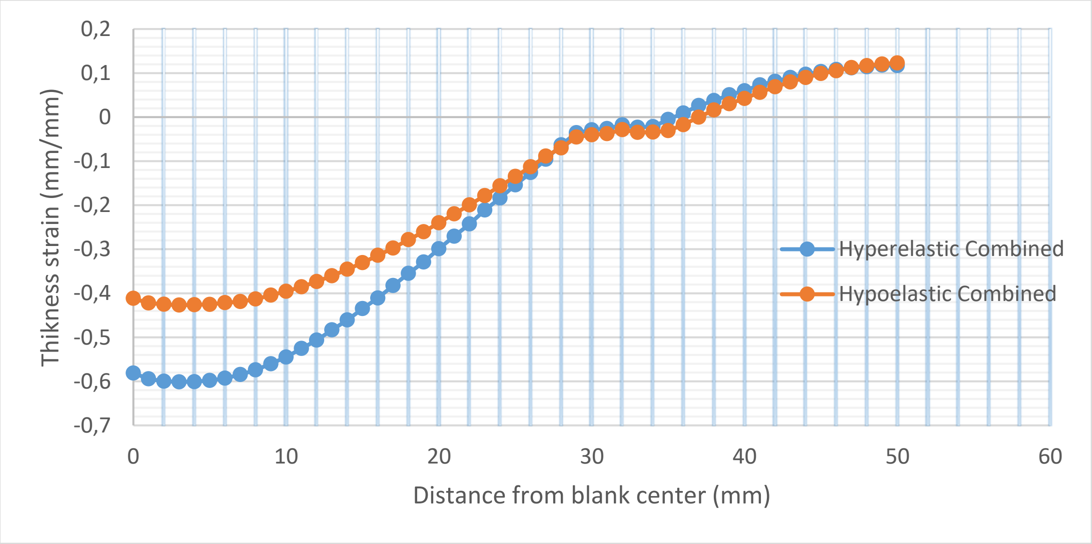

Figure 6.45 Thickness strain distributions estimated by hyperelastic and hypoelastic combined hardening models (45 mm punch displacement, round, SS304)

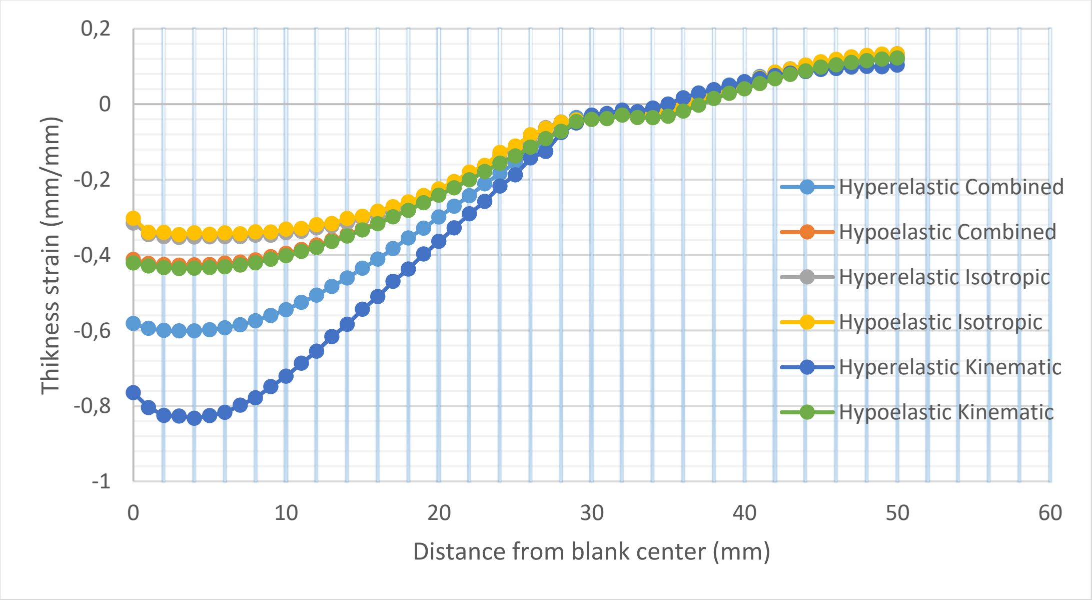

Figure 6.46 Comparison of all of the results (45 mm punch displacement, round, SS304)

Even larger differences of results for combined hardening and kinematic hardening of hyperelastic and hypoelastic based models exist at 45 mm punch displacement of round bottom cup drawing.

6.3. Results of DKP6112

In this section cylindrical, square and round bottom cup drawing results of DKP6112 material is given.

6.3.1. Cylindrical Cup Drawing Results

Thickness strain distributions for cylindrical cup drawing of DKP6112 material for 15, 25 and 35 mm punch displacements are presented here.

6.3.1.1. 15 mm Punch Displacement

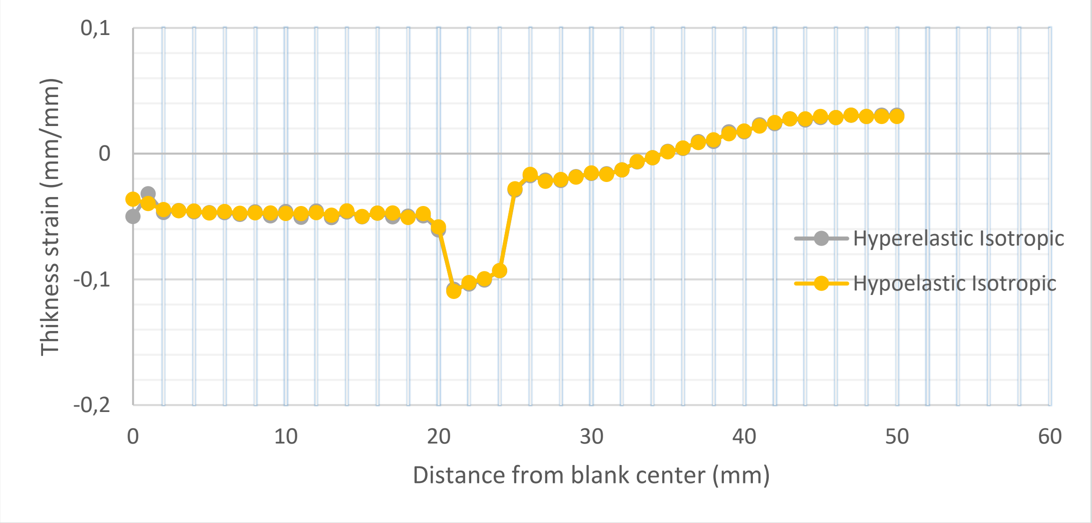

Figure 6.47 Thickness strain distributions estimated by hyperelastic and hypoelastic isotropic hardening models (15 mm punch displacement, cylindrical, DKP6112)

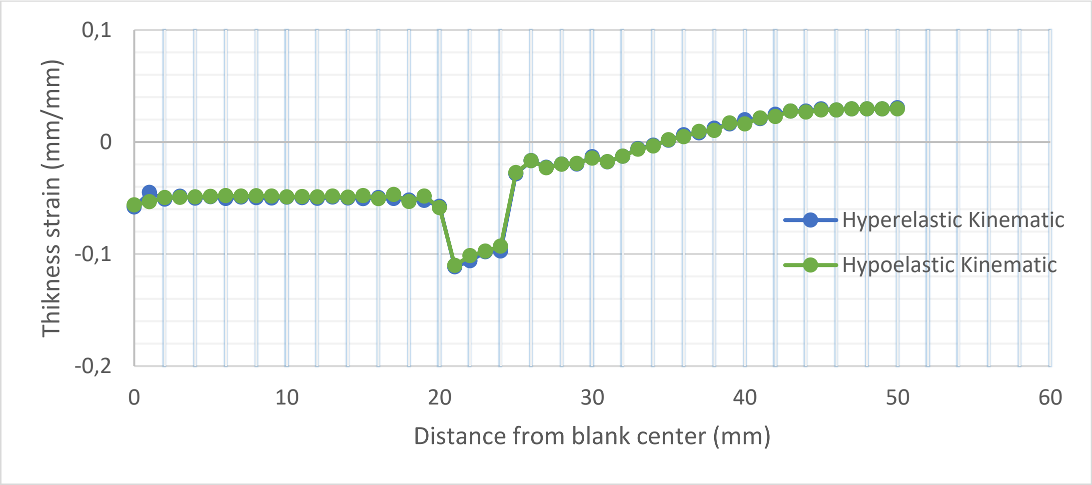

Figure 6.48 Thickness strain distributions estimated by hyperelastic and hypoelastic kinematic hardening models (15 mm punch displacement, cylindrical, DKP6112)

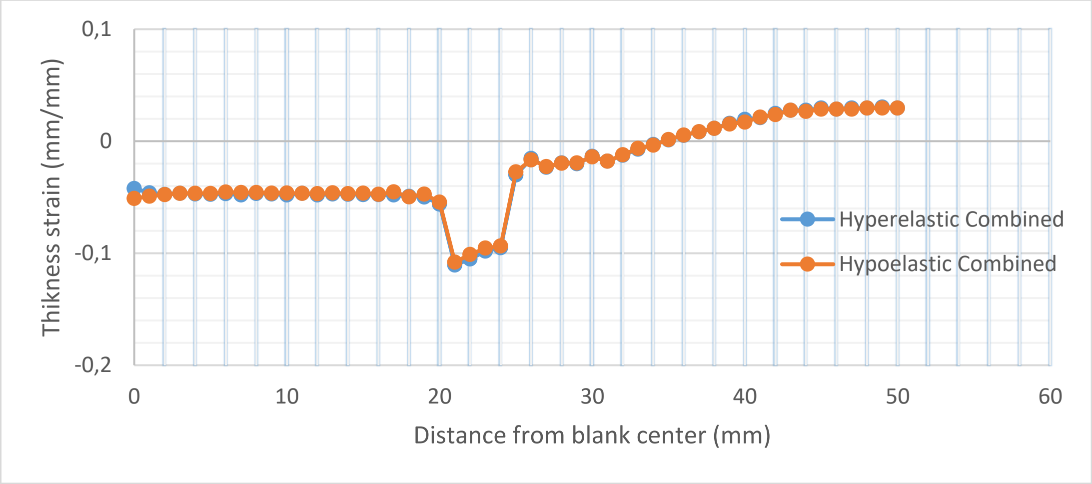

Figure 6.49 Thickness strain distributions estimated by hyperelastic and hypoelastic combined hardening models (15 mm punch displacement, cylindrical, DKP6112)

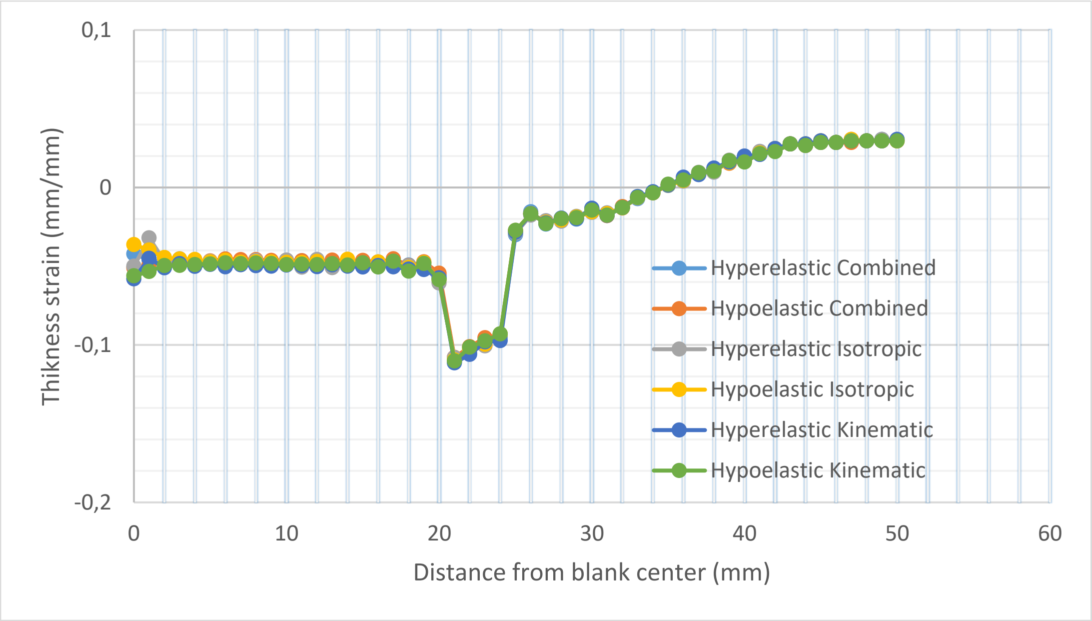

Figure 6.50 Comparison of all of the results (15 mm punch displacement, cylindrical, DKP6112)

At 15 mm results obtained for each hyperelastic and hypoelastic model seem to be in agreement with each other.

6.3.1.2. 25 mm Punch Displacement

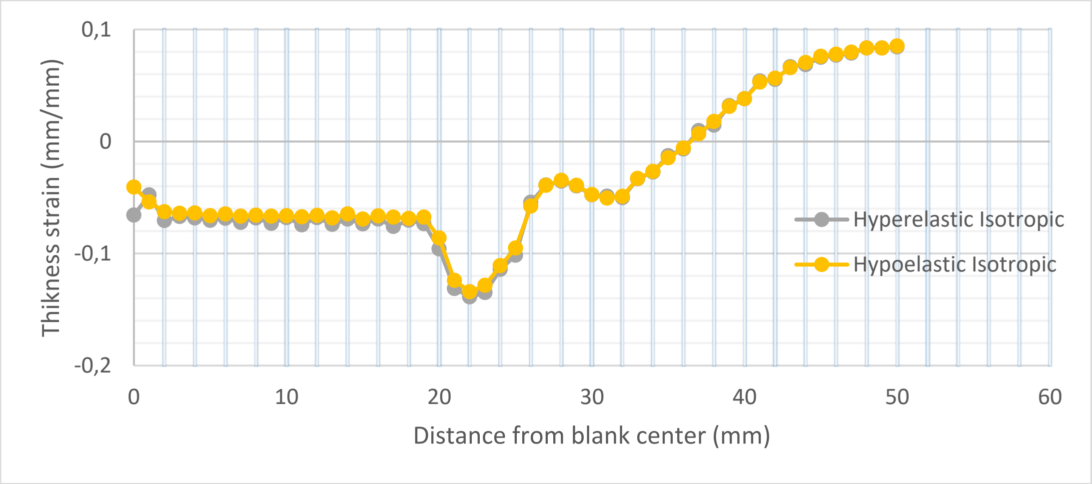

Figure 6.51 Thickness strain distributions estimated by hyperelastic and hypoelastic isotropic hardening models (25 mm punch displacement, cylindrical, DKP6112)

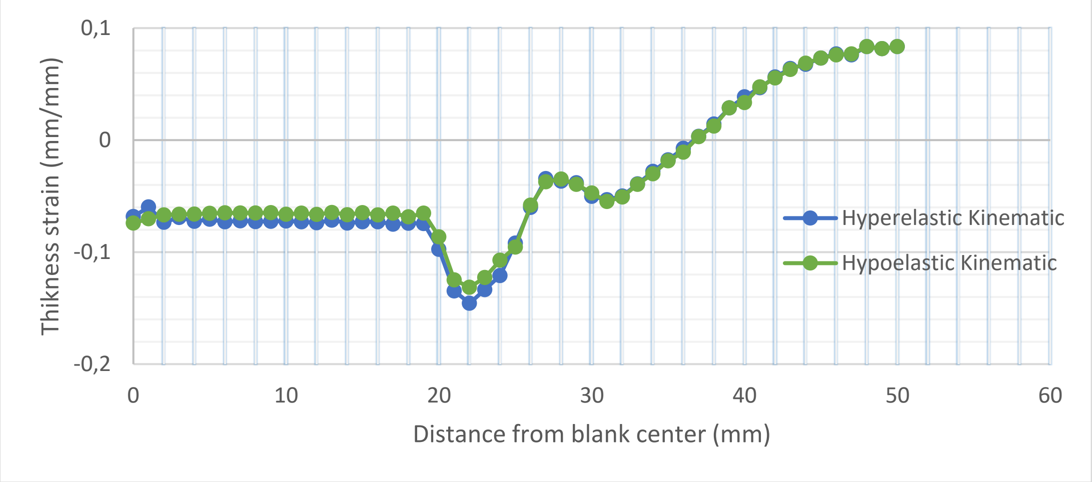

Figure 6.52 Thickness strain distributions estimated by hyperelastic and hypoelastic kinematic hardening models (25 mm punch displacement, cylindrical, DKP6112)

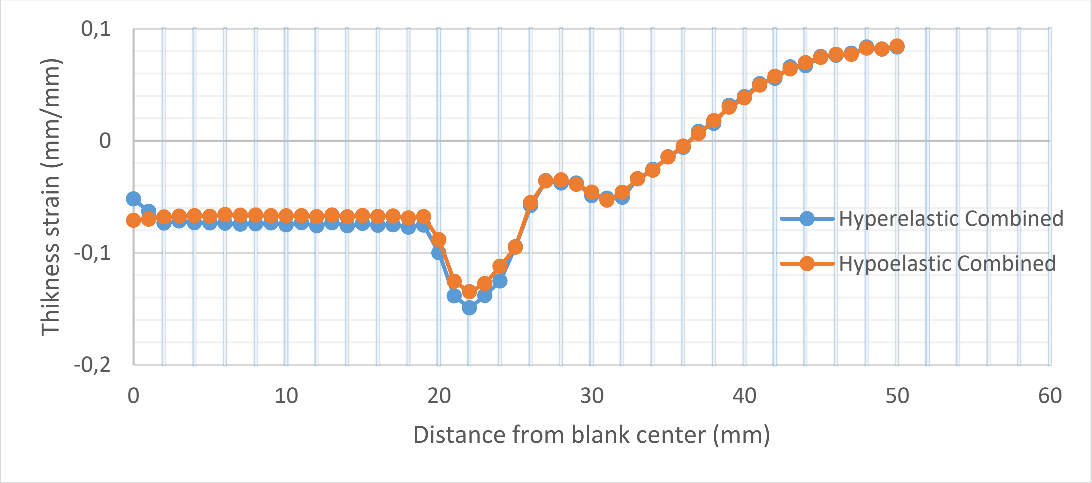

Figure 6.53 Thickness strain distributions estimated by hyperelastic and hypoelastic combined hardening models (25 mm punch displacement, cylindrical, DKP6112)

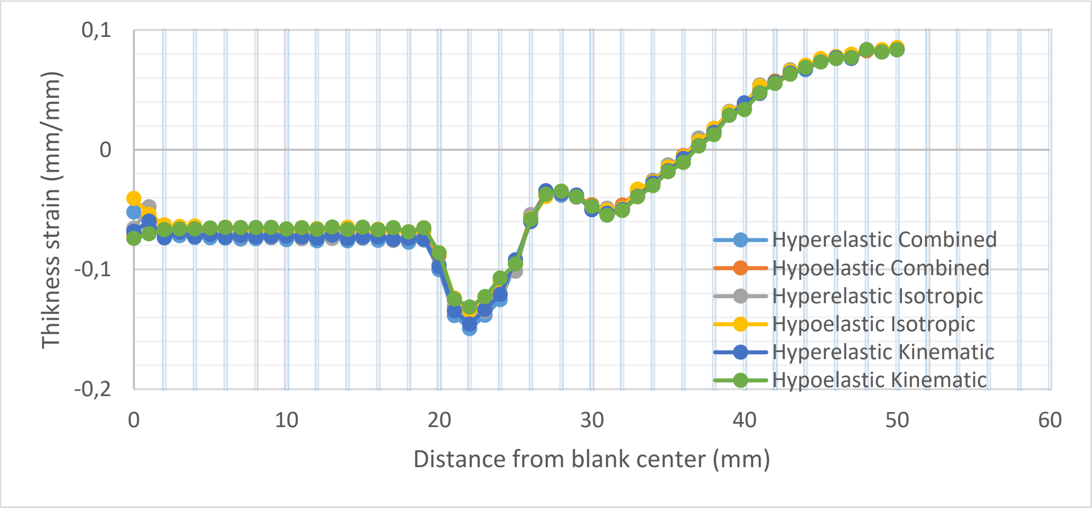

Figure 6.54 Comparison of all of the results (25 mm punch displacement, cylindrical, DKP6112)

Again, slight to no difference in the results can be seen for 25 mm punch displacement between hyperelastic and hypoealstic based models. Differences are slightly more noticeable towards the center of the blank especially for combined and kinematic hardening models.

6.3.1.3. 35 mm Punch Displacement

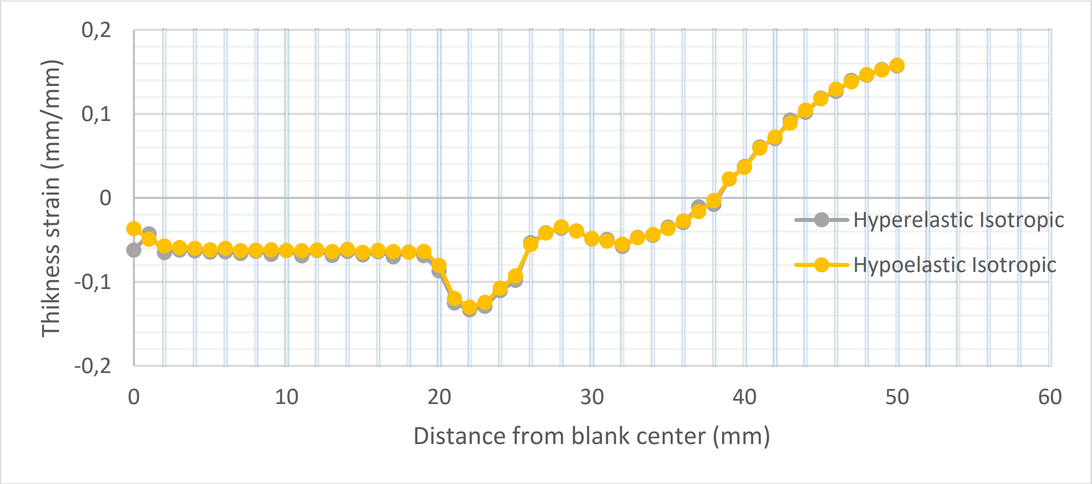

Figure 6.55 Thickness strain distributions estimated by hyperelastic and hypoelastic isotropic hardening models (35 mm punch displacement, cylindrical, DKP6112)

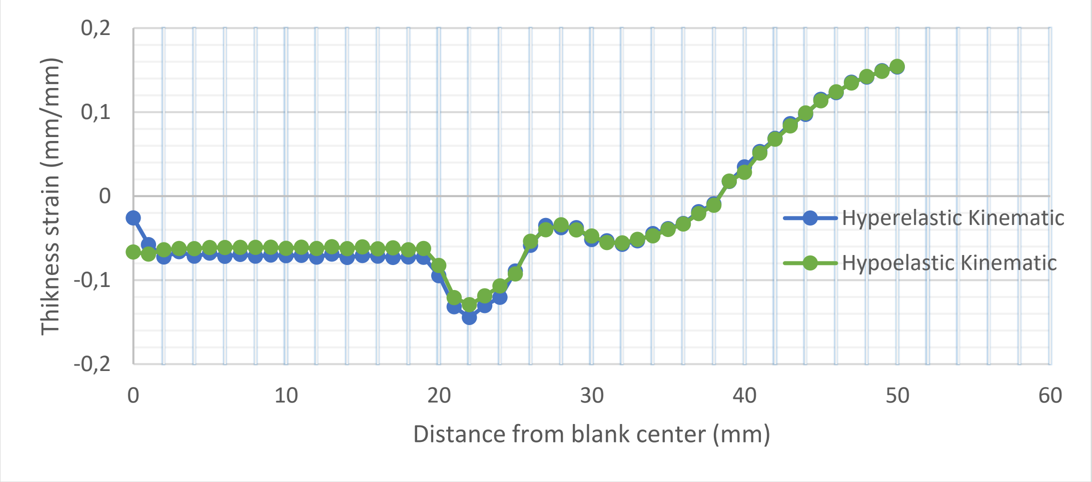

Figure 6.56 Thickness strain distributions estimated by hyperelastic and hypoelastic kinematic hardening models (35 mm punch displacement, cylindrical, DKP6112)

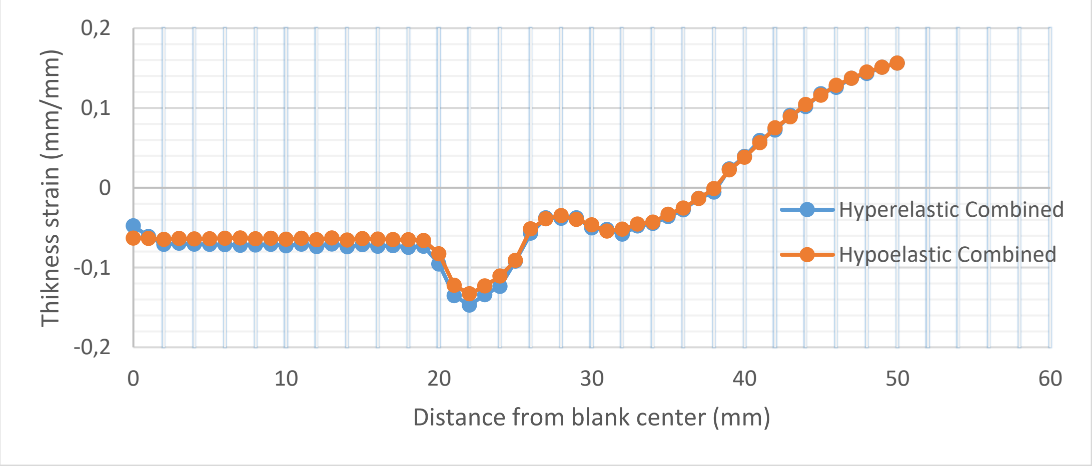

Figure 6.57 Thickness strain distributions estimated by hyperelastic and hypoelastic combined hardening models (35 mm punch displacement, cylindrical, DKP6112)

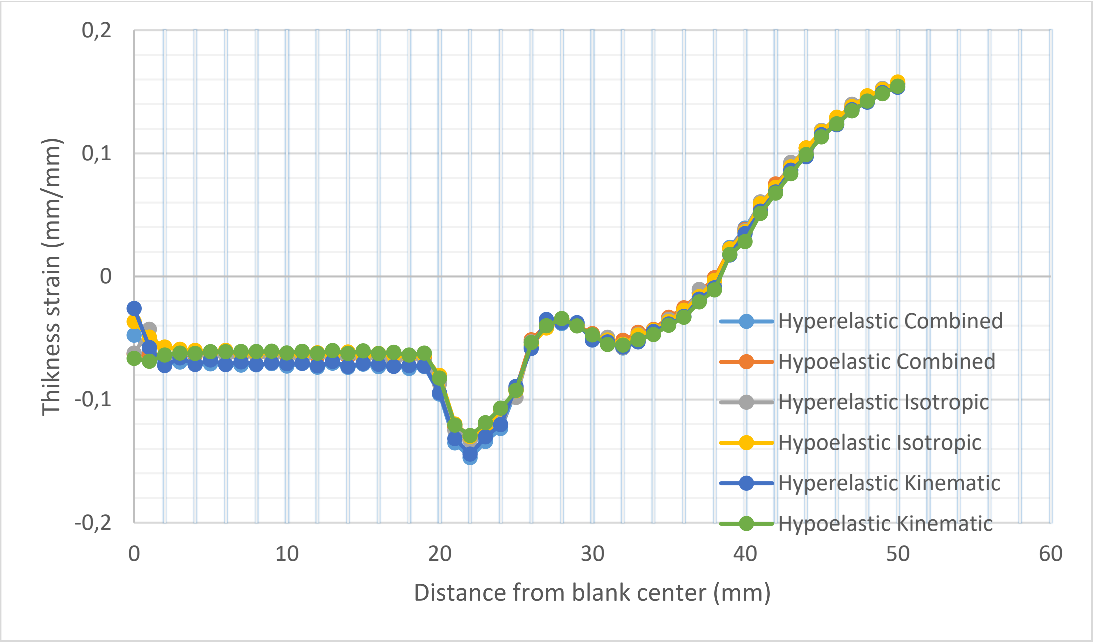

Figure 6.58 Comparison of all of the results (35 mm punch displacement, cylindrical, DKP6112)

The results at 35 mm punch displacement resembles to that of 25 mm. Again, very slight differences can be seen for combined and kinematic hardening models towards the center and halfway of the blank, better agreement seen towards the edge.

6.3.2. Square Cup Drawing Results

Thickness strain distributions for square cup drawing of DKP6112 for different punch displacements are given in this part.

6.3.2.1. 15 mm Punch Displacement - Rolling Direction

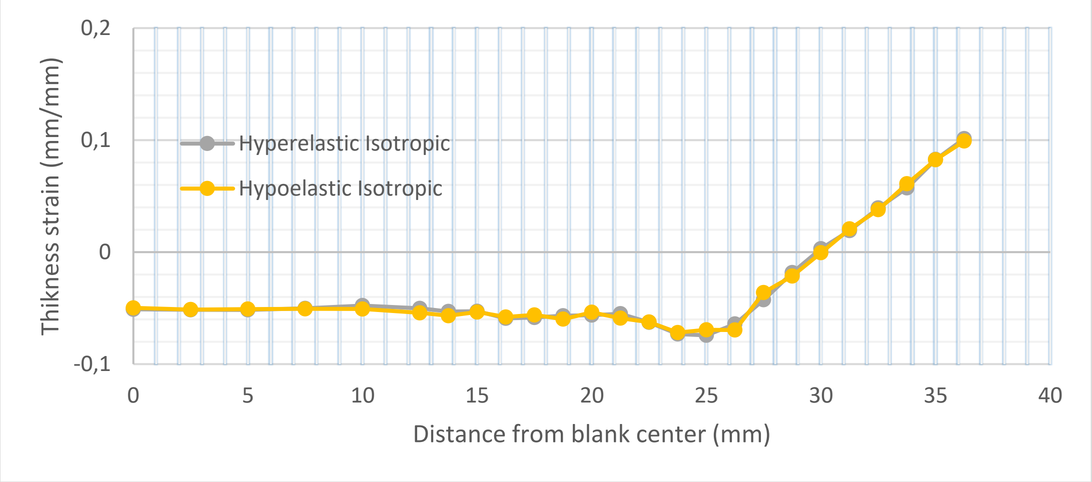

Figure 6.59 Thickness strain distributions estimated by hyperelastic and hypoelastic isotropic hardening models in rolling direction (15 mm punch displacement, square, DKP6112)

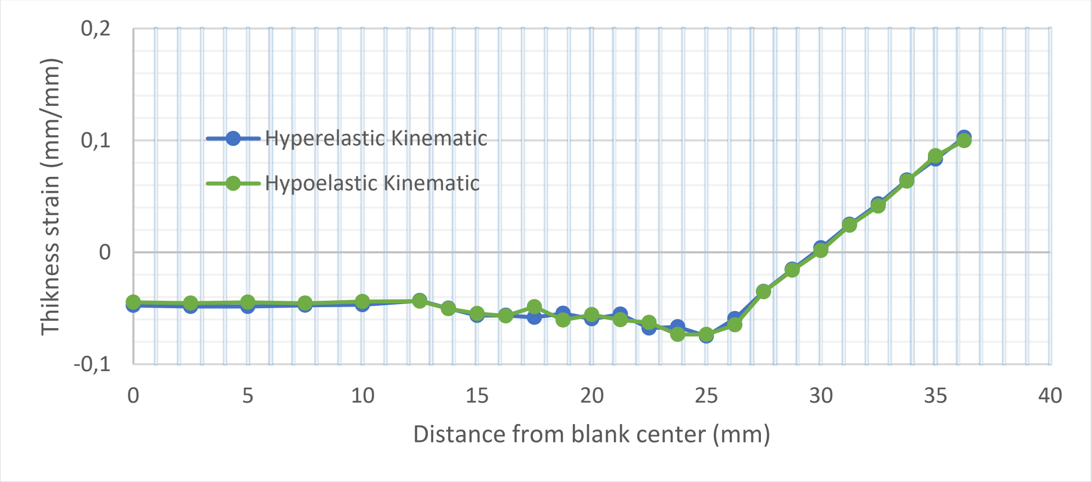

Figure 6.60 Thickness strain distributions estimated by hyperelastic and hypoelastic kinematic hardening models in rolling direction (15 mm punch displacement, square, DKP6112)

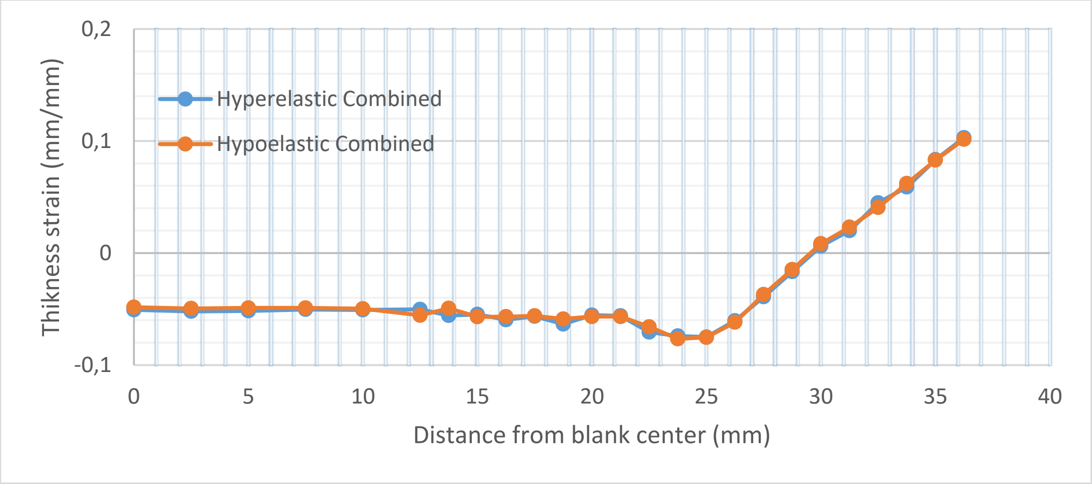

Figure 6.61 Thickness strain distributions estimated by hyperelastic and hypoelastic combined hardening models in rolling direction (15 mm punch displacement, square, DKP6112)

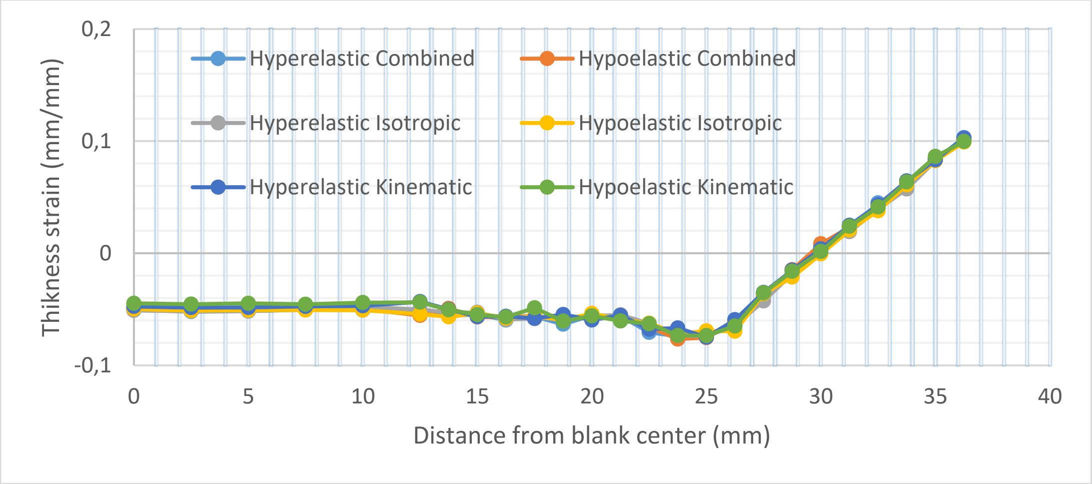

Figure 6.62 Comparison of all of the results in rolling direction (15 mm punch displacement, square, DKP6112)

All models are in almost total agreement for all six of the models considering the results for 15 mm punch displacement in rolling direction.

6.3.2.2. 15 mm Punch Displacement - Diagonal Direction

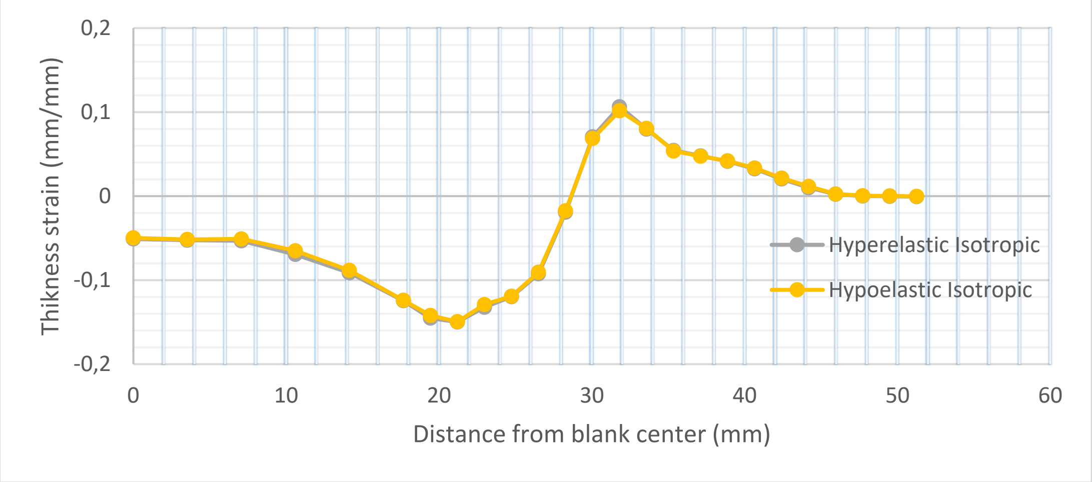

Figure 6.63 Thickness strain distributions estimated by hyperelastic and hypoelastic isotropic hardening models in diagonal direction (15 mm punch displacement, square, DKP6112)

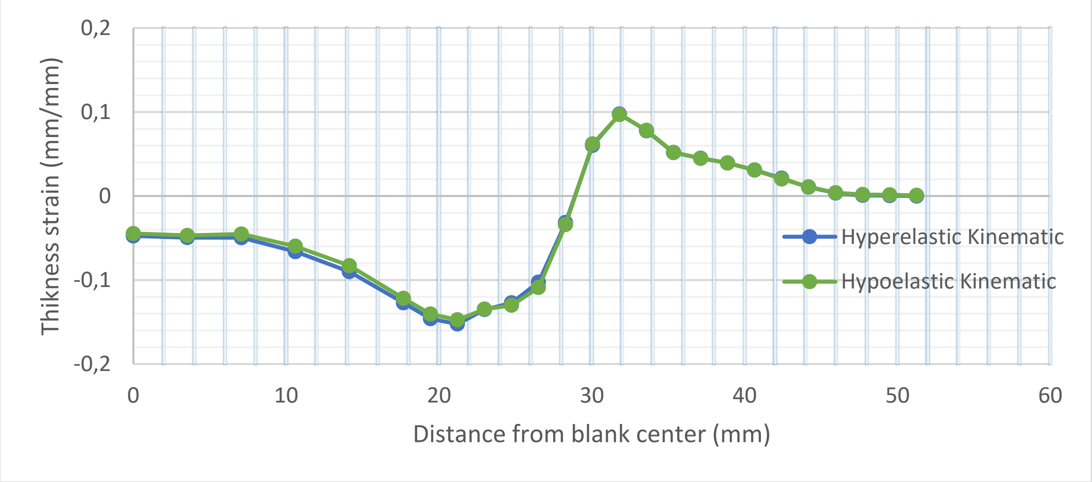

Figure 6.64 Thickness strain distributions estimated by hyperelastic and hypoelastic kinematic hardening models in diagonal direction (15 mm punch displacement, square, DKP6112)

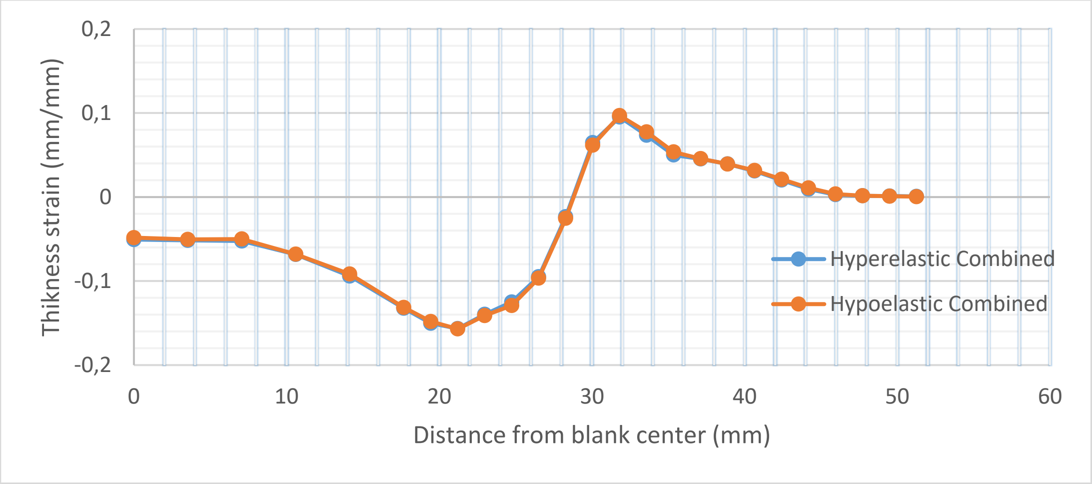

Figure 6.65 Thickness strain distributions estimated by hyperelastic and hypoelastic combined hardening models in diagonal direction (15 mm punch displacement, square, DKP6112)

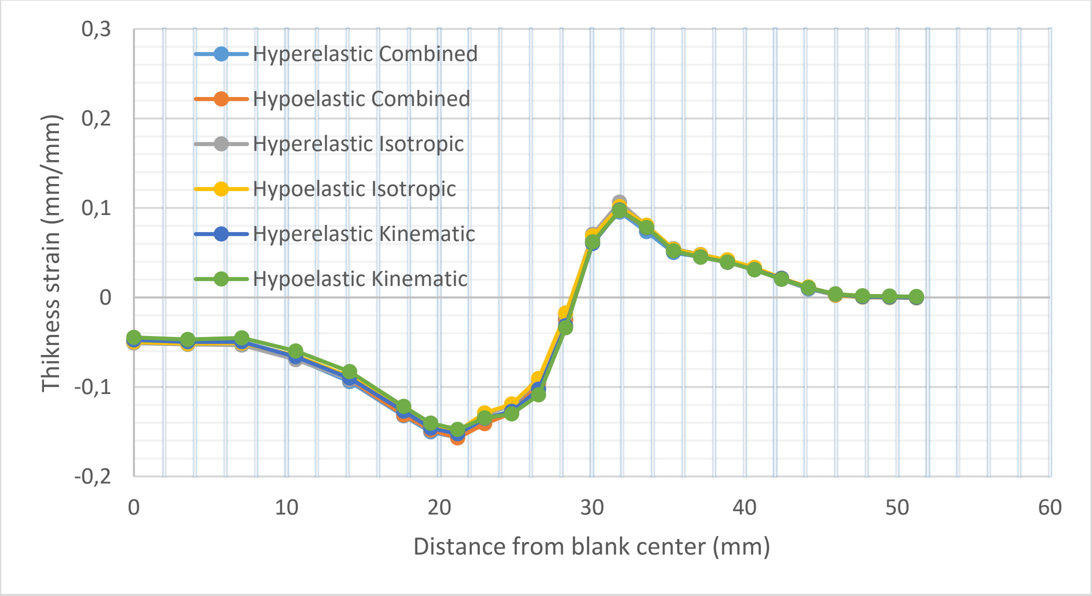

Figure 6.66 Comparison of all of the results in diagonal direction (15 mm punch displacement, square, DKP6112)

In diagonal direction again all results in almost perfect agreement.

6.3.2.3. 20 mm Punch Displacement - Rolling Direction

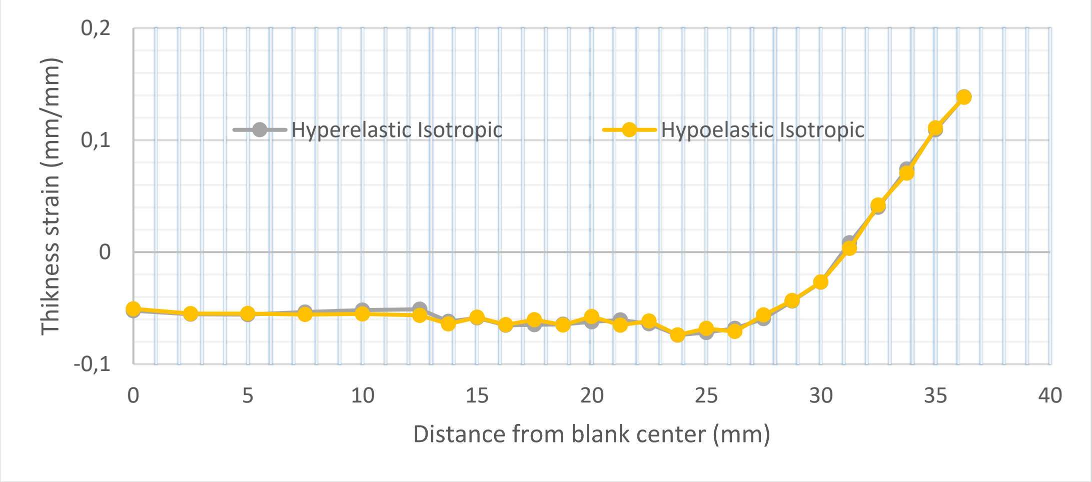

Figure 6.67 Thickness strain distributions estimated by hyperelastic and hypoelastic isotropic hardening models in rolling direction (20 mm punch displacement, square, DKP6112)

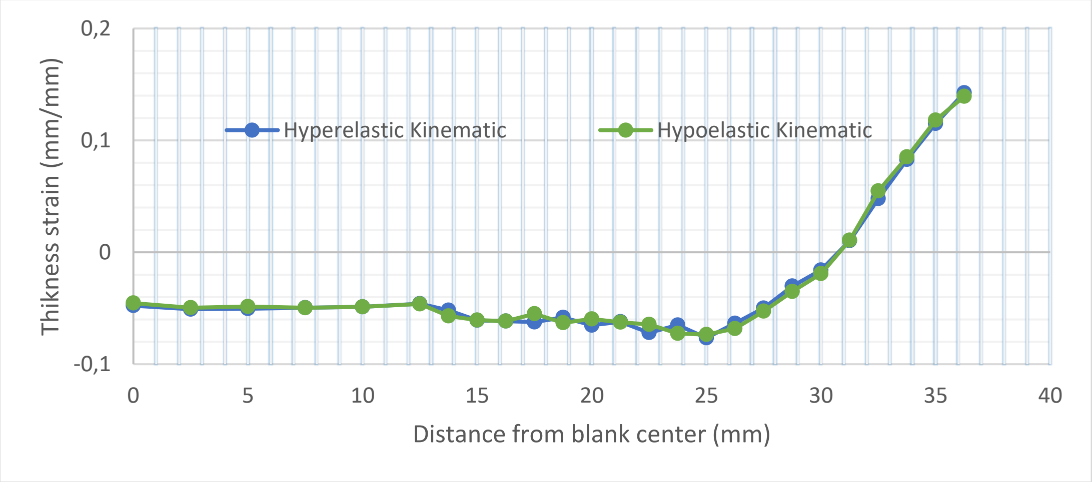

Figure 6.68 Thickness strain distributions estimated by hyperelastic and hypoelastic kinematic hardening models in rolling direction (20 mm punch displacement, square, DKP6112)

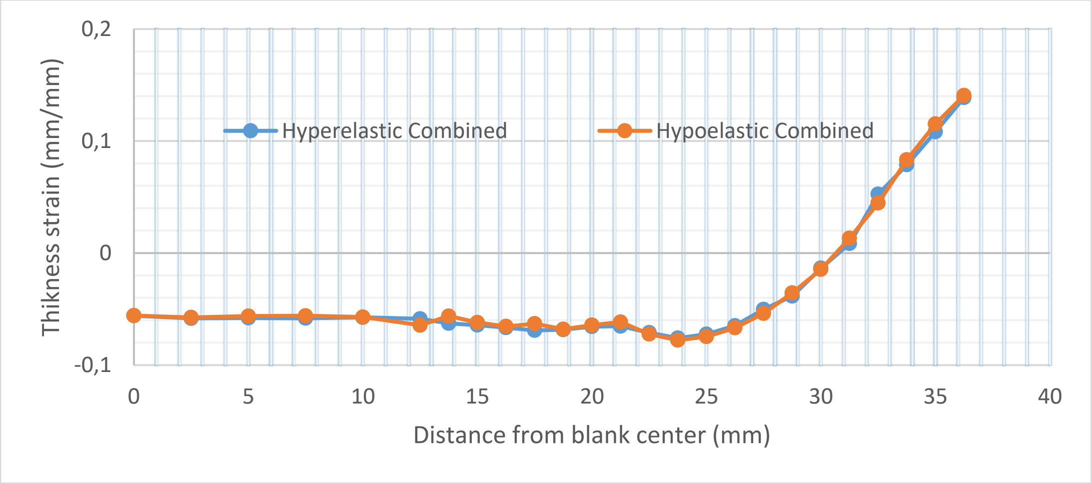

Figure 6.69 Thickness strain distributions estimated by hyperelastic and hypoelastic combined hardening models in rolling direction (20 mm punch displacement, square, DKP6112)

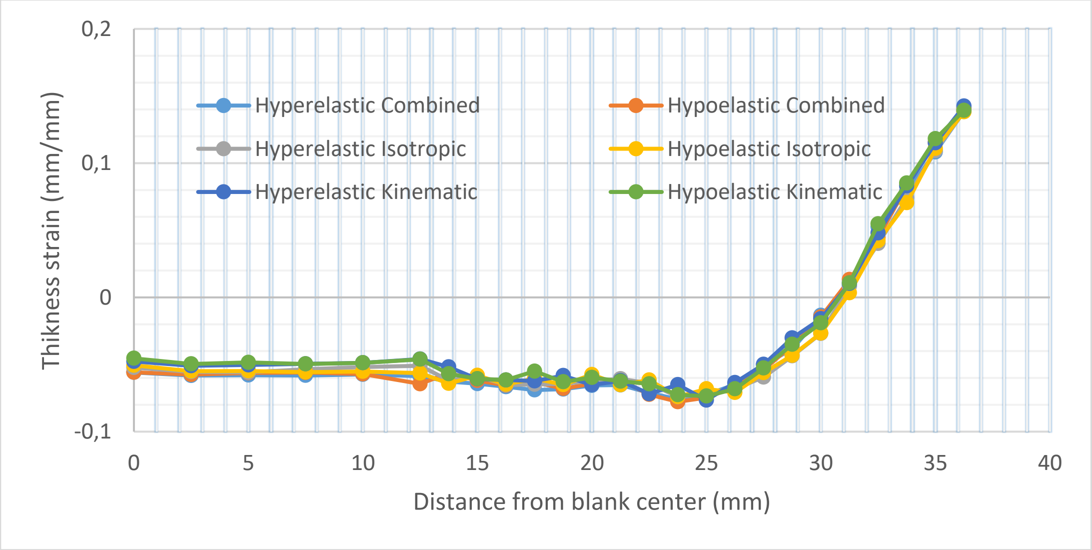

Figure 6.70 Comparison of all of the results in rolling direction (20 mm punch displacement, square, DKP6112)

Good agreement between hyperelastic and hypoelastic based models exist in rolling direction for 20 mm punch travel as well.

6.3.2.4. 20 mm Punch Displacement - Diagonal Direction

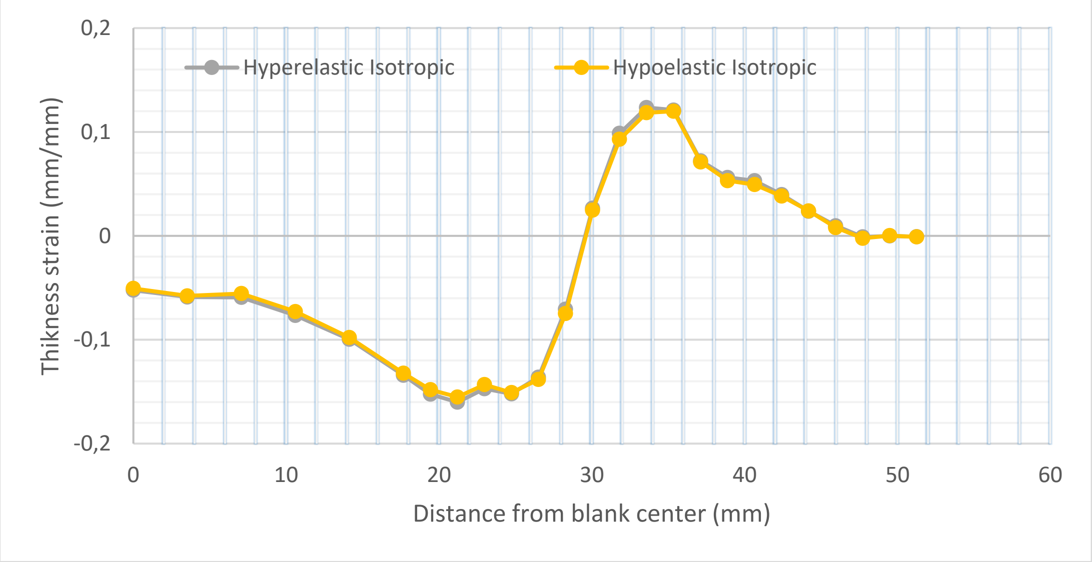

Figure 6.71 Thickness strain distributions estimated by hyperelastic and hypoelastic isotropic hardening models in diagonal direction (20 mm punch displacement, square, DKP6112)

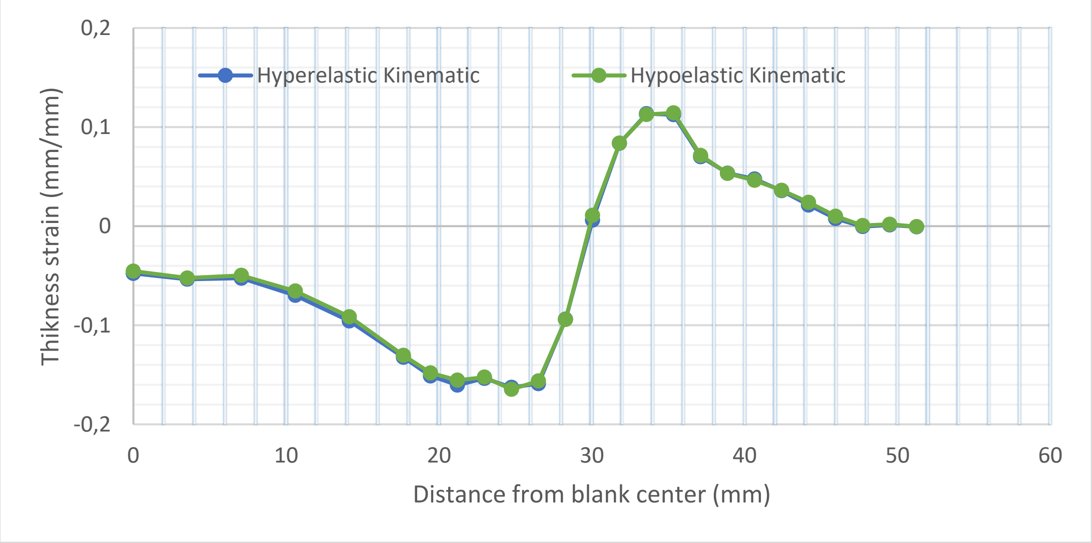

Figure 6.72 Thickness strain distributions estimated by hyperelastic and hypoelastic kinematic hardening models in diagonal direction (20 mm punch displacement, square, DKP6112)

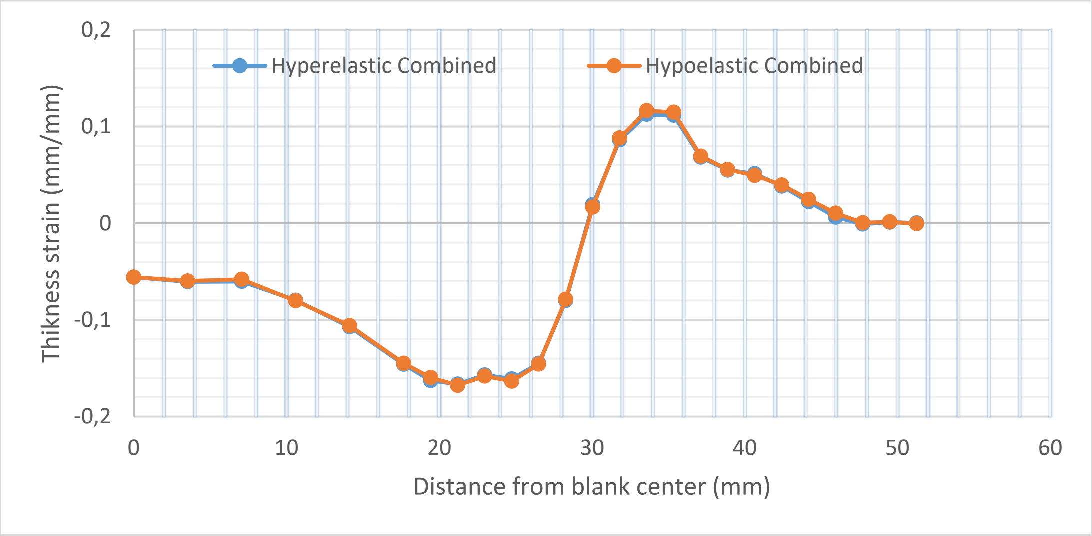

Figure 6.73 Thickness strain distributions estimated by hyperelastic and hypoelastic combined hardening models in diagonal direction (20 mm punch displacement, square, DKP6112)

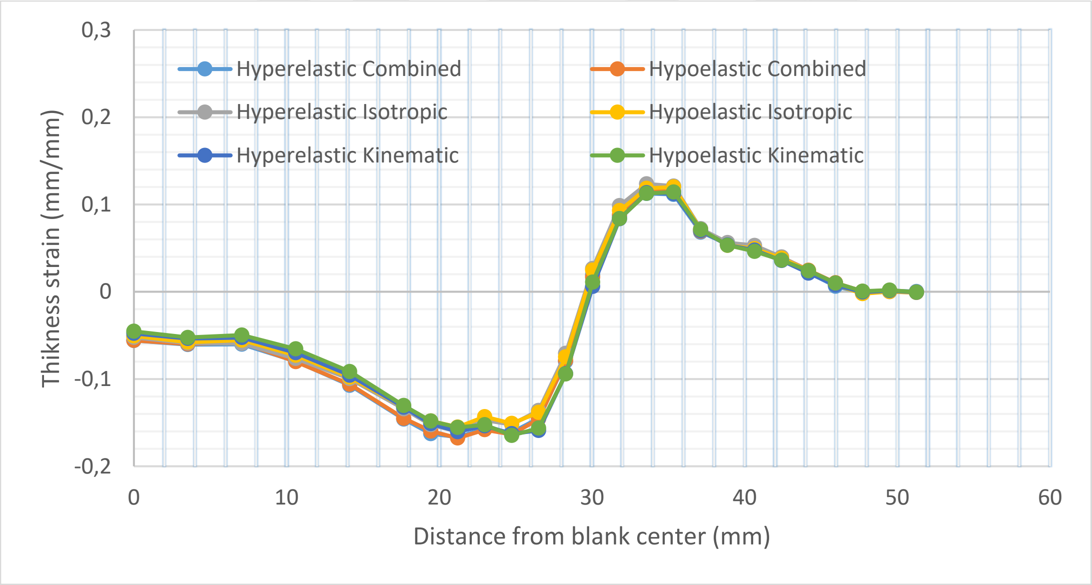

Figure 6.74 Comparison of all of the results in diagonal direction (20 mm punch displacement, square, DKP6112)

Very good agreement between hyperelastic and hypoelastic based models seen at diagonal direction of 20 mm punch displacement as well.

6.3.2.5. 25 mm Punch Displacement - Rolling Direction

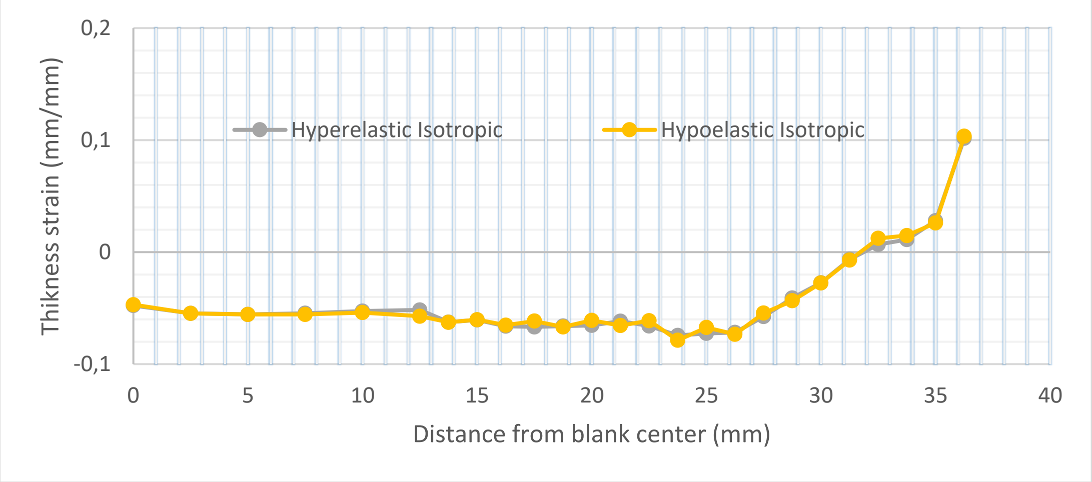

Figure 6.75 Thickness strain distributions estimated by hyperelastic and hypoelastic isotropic hardening models in rolling directions (25 mm punch displacement, square, DKP6112)

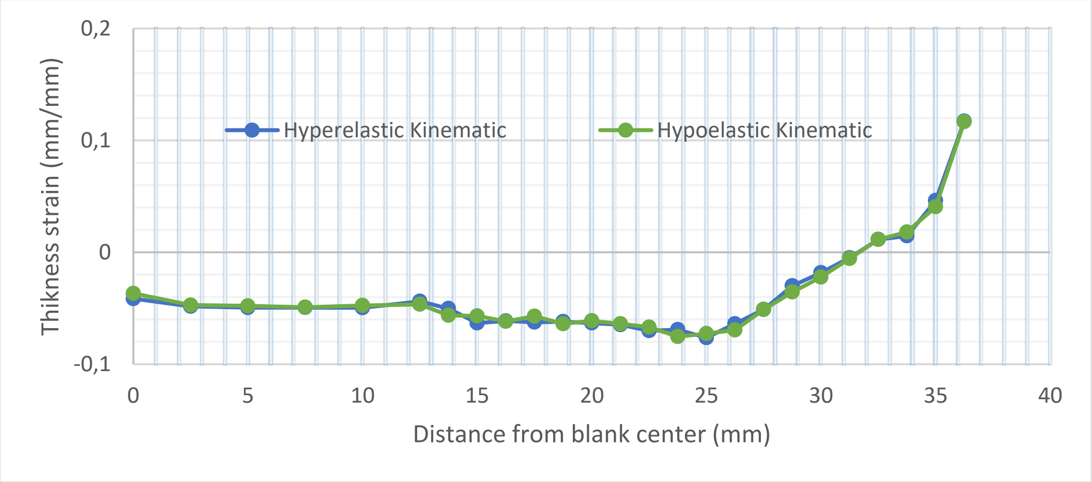

Figure 6.76 Thickness strain distributions estimated by hyperelastic and hypoelastic kinematic hardening models in rolling directions (25 mm punch displacement, square, DKP6112)

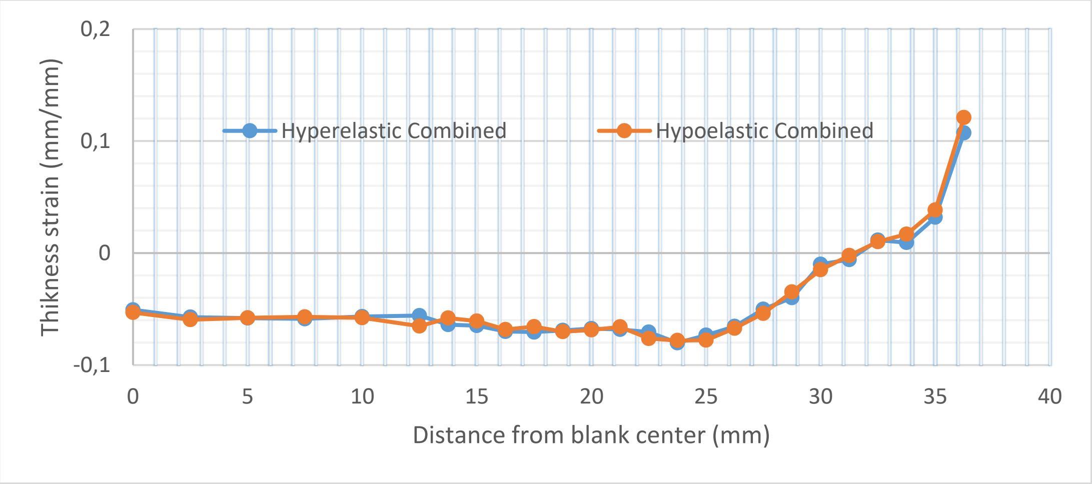

Figure 6.77 Thickness strain distributions estimated by hyperelastic and hypoelastic combined hardening models in rolling directions (25 mm punch displacement, square, DKP6112)

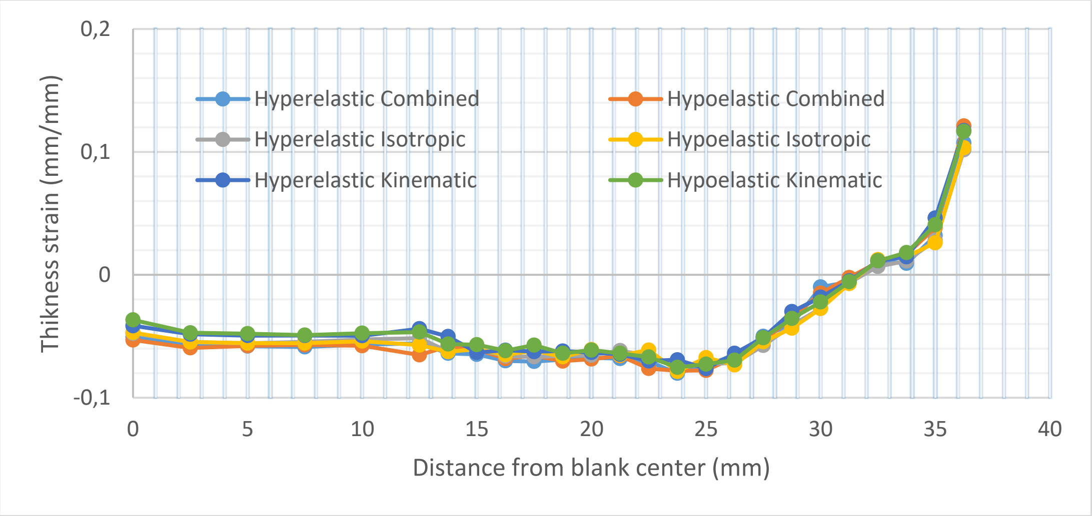

Figure 6.78 Comparison of all of the results in rolling direction (25 mm punch displacement, square, DKP6112)

Good correlation between results can be seen for 25 mm punch displacement as well except some individual local differences for all three hardening models.

6.3.2.6. 25 mm Punch Displacement - Diagonal Direction

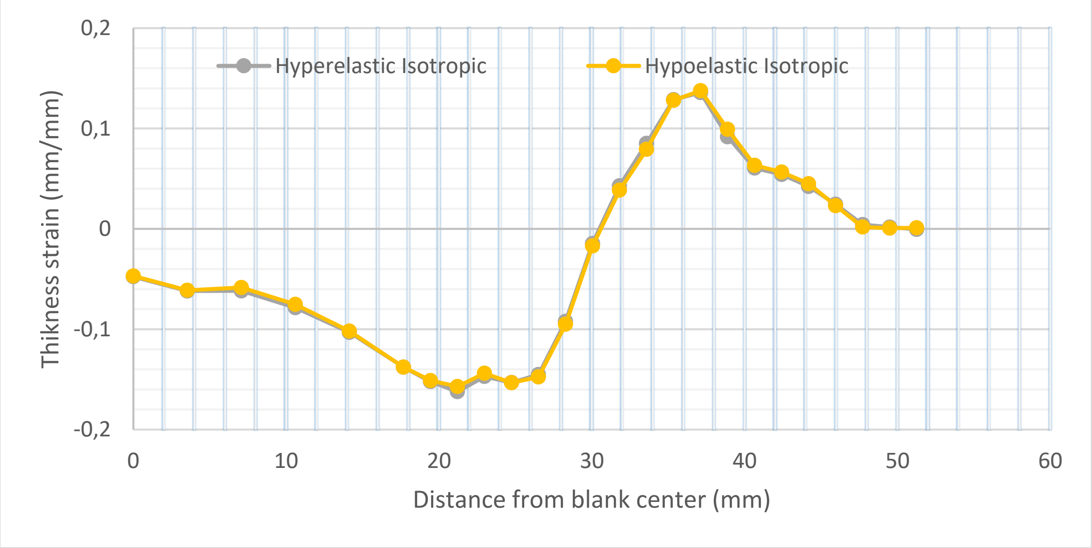

Figure 6.79 Thickness strain distributions estimated by hyperelastic and hypoelastic isotropic hardening models in diagonal direction (25 mm punch displacement, square, DKP6112)

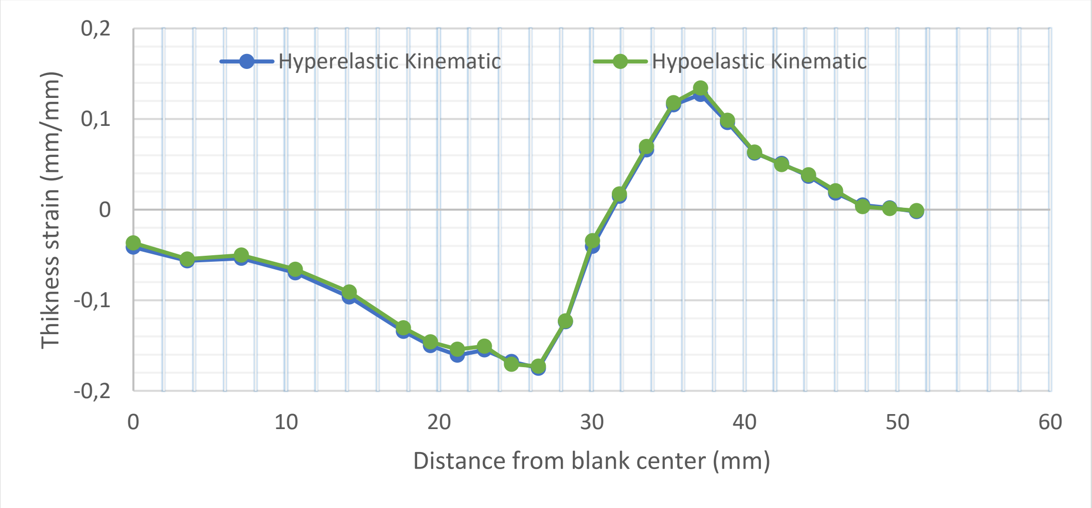

Figure 6.80 Thickness strain distributions estimated by hyperelastic and hypoelastic kinematic hardening models in diagonal direction (25 mm punch displacement, square, DKP6112)

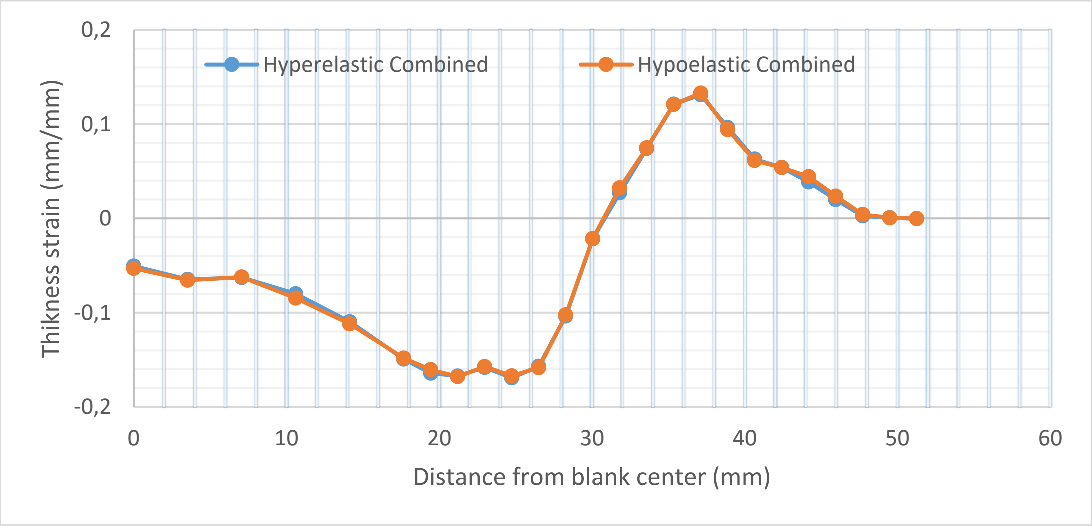

Figure 6.81 Thickness strain distributions estimated by hyperelastic and hypoelastic combined hardening models in diagonal direction (25 mm punch displacement, square, DKP6112)

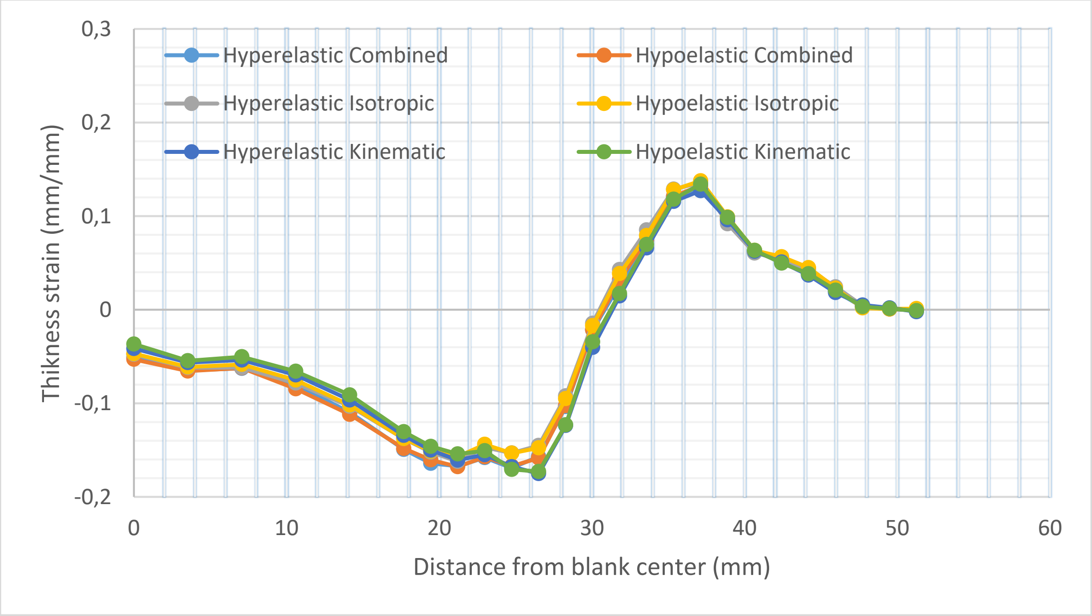

Figure 6.82 Comparison of results in diagonal direction (25 mm punch displacement, square, DKP6112)

Agreement of hyperelastic based and hypoelastic based materials continues in diagonal direction for 25 mm punch displacement as well.

6.3.3. Round Bottom Cup Drawing Results

This section gives results of round bottom cup drawing simulation of DKP6112 material.

6.3.3.1. 20 mm Punch Displacement

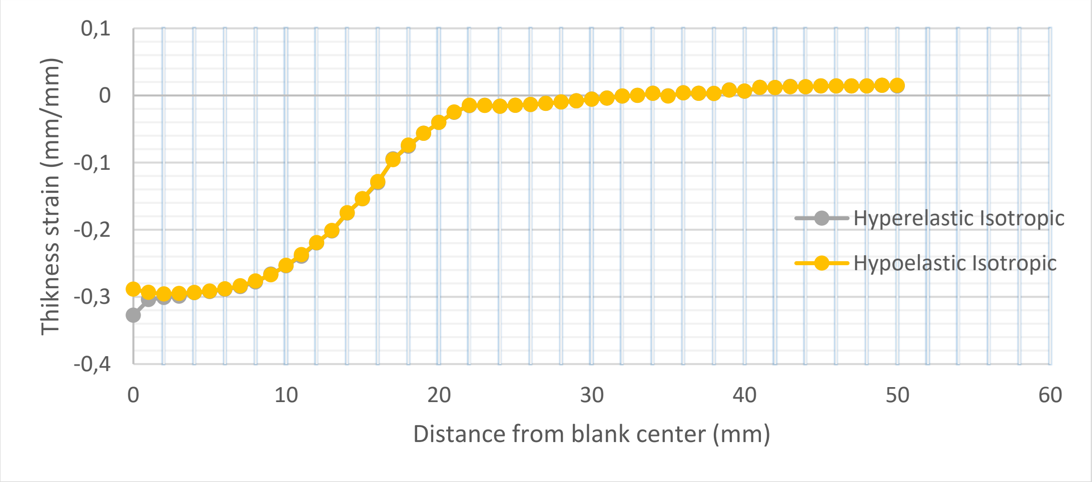

Figure 6.83 Thickness strain distributions estimated by hyperelastic and hypoelastic isotropic hardening models (20 mm punch displacement, round, DKP6112)

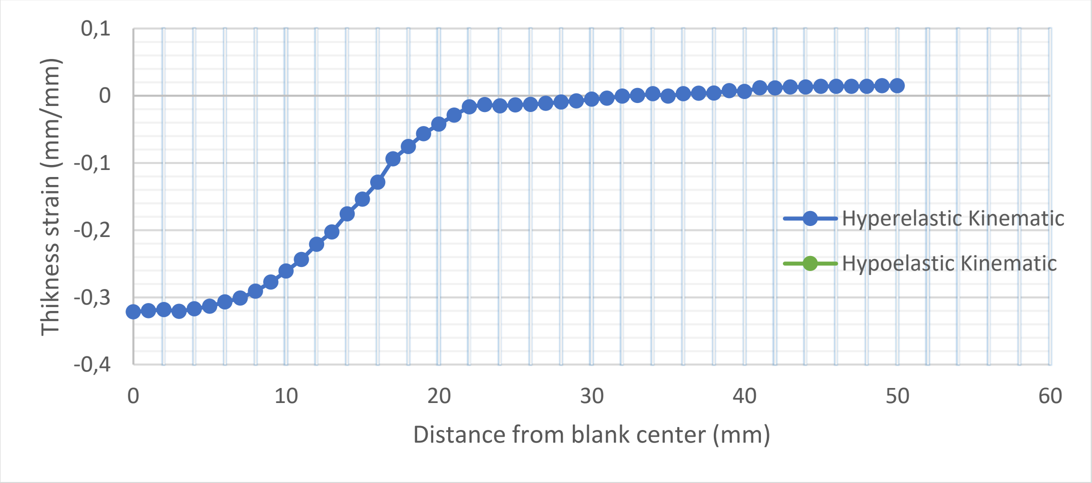

Figure 6.84 Thickness strain distributions estimated by hyperelastic and hypoelastic kinematic hardening models (20 mm punch displacement, round, DKP6112)

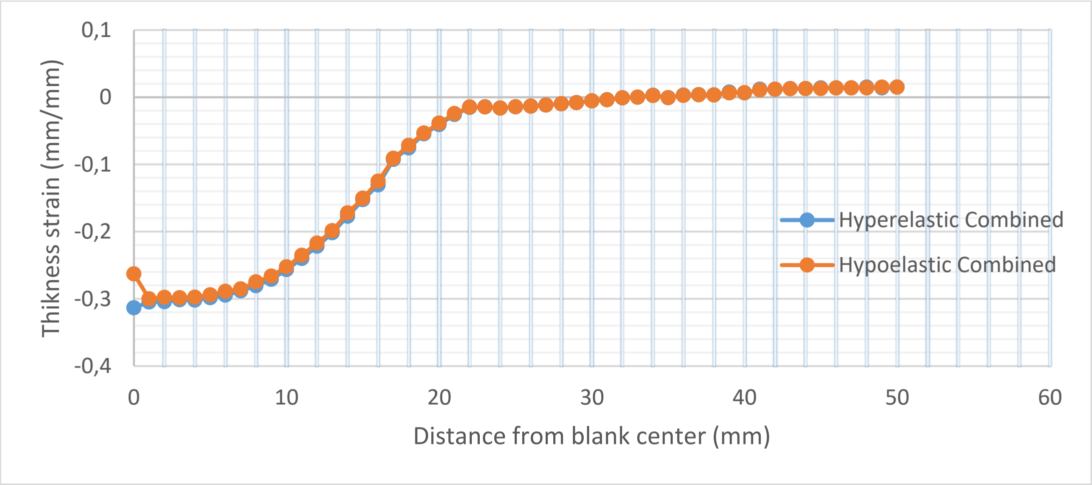

Figure 6.85 Thickness strain distributions estimated by hyperelastic and hypoelastic combined hardening models (20 mm punch displacement, round, DKP6112)

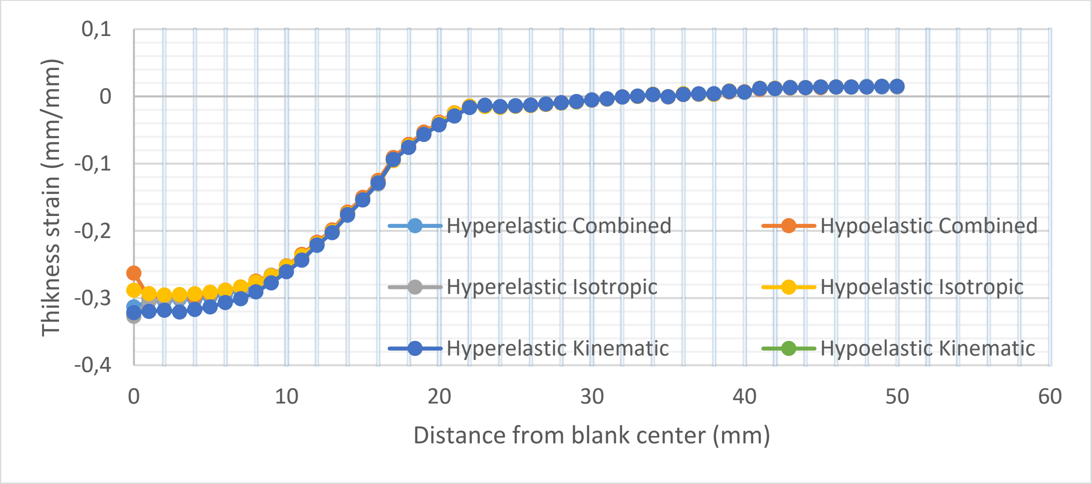

Figure 6.86 Comparison of all of the results (20 mm punch displacement, round, DKP6112)

For 20 mm punch travel in round bottom cup drawing of DKP6112 material little to no difference can be seen in the results. A difference can be seen at the exact middle of the sheet due to a numerical discrepancy.

CHAPTER 7

CONCLUSIONS AND FUTURE WORK

The study in the thesis involves numerical comparison of two constitutive relations that have distinct characteristics, namely hyperelastic and hypoelastic based plasticity models. Three different hardening rules implemented to these material types being Voce type isotropic hardening [14], Armstrong Frederick type kinematic hardening [13] and a combined hardening model together with von Mises yield criterion. DP600 material is used only for cylindrical cup drawing simulation to verify material models implemented by comparing the results to that of Brepols et al. [15] who used a similar model in their work. Two additional materials, SS304 and DKP6112, are used in simulations of cylindrical, square and round bottom cup drawing processes. Results obtained lead us to following conclusions.

1. Punch force results obtained for cylindrical cup drawing simulation of DP600 material for hyperelastic and hypoelastic based plasticity models with combined hardening show almost exact values to the ones of Brepols et al. [15] who used combined hardening in their simulation as well.
2. Voce type isotropic hardening [14] model estimates a little higher maximum punch force value, whereas Armstrong-Frederick type kinematic hardening [13] estimates smaller one. Almost exact values were seen for hypoelastic and hyperelastic based models regardless of hardening model in simulation of cylindrical cup drawing of DP600.
3. For SS304, the simulations of cylindrical and square bottom cup drawing give extremely close results for hyperelastic and hypoelastic based plasticity models for the three hardening models. However, for round bottom cup

drawing of SS304, simulation results sigificanly deviates from each other for kinematic and combined hardening especially when extreme thinning of a specimen is predicted.

4. For DKP6112 material, the results of the simulations of cylindrical and square bottom cup of hyperelastic and hypoelastic based plasticity models match for all hardening models. Round bottom cup drawing of DKP6112 produced similar results for hypoelastic and hyperelastic based material models as well.
5. It can be said that, hyperelastic and hypoelastic based plasticity models give almost the same results for isotropic hardening. However, for kinematic and combined hardening, they may result in different deformed configurations.

As future work, it would be useful to compare the obtained simulations results with experimental data and anisotropic yield criteria may be applied to further compare these two fundamentally different material models. Different integrations algorithms such as exponential map algorithm can be tried to improve results.

REFERENCES

[1] Hill, R., “A general theory of uniqueness and stability in elastic-plastic solids”, J. Mech. Phys. Solids, 6, 236–249, 1958.

[2] Hill, R., “Some basic principles in the mechanics of solids without a natural time”, J. Mech. Phys.Solids, 7, 209–225, 1959.

[3] Prager, W., “An elementary discussion of definitions of stress rate”, Quart. Appl. Math., 18, 403–407, 1960.

[4] Hibbitt, H., Marcal, P., and Rice, J., “A finite element formulation for problems of large strain and large displacement”, International Journal of Solids and Structures, 6, 1069–1086, 1970.

[5] Hughes, T. J. R. and Winget, J., “Finite rotation effects in numerical integration of rate constitutive equations arising in large-deformation analysis”, International Journal for Numerical Methods in Engineering, 15, 1862–1867, 1980.

[6] Eckart, C., “The thermodynamics of irreversible processes”, The theory of elasticity and anelasticity. Phys. Rev. 73, 373–382, 1948.

[7] Lee, E. H. and Liu, D. T., “Finite-strain elastic-plastic theory with application to plane-wave Analysis”, Journal of Applied Physics, 38, 19–27, 1967.

[8] Freund, L. B., “Constitutive equations for elastic-plastic materials at finite strain”, Int. J. Solid Structures, 6, 1193–1209, 1970.

[9] Rice, J. R., “Inelastic constitutive relations for solids: an internal-variable theory and its application to metal plasticity”, J. Mech. Phys. Solids, 19, 433–455, 1971.

[10] Simo, J., “On the computational significance of the intermediate configuration and hyperelastic stress relations in finite deformation elastoplasticity”, Mechanics of Materials, 4, 439–451, 1985.

[11] Vladimirov, I. N., Pietryga, M. P., and Reese, S., “Anisotropic finite elastoplasticity with nonlinear kinematic and isotropic hardening and application to sheet metal forming”, International Journal of Plasticity, 26, 659–687, 2010.

[12] Vladimirov, I. N., Pietryga, M. P., and Reese, S., “On the influence of kinematic hardening on plastic anisotropy in the context of finite strain plasticity”, International Journal of Material Forming, 4, 255–267, 2011.

[13] Armstrong, P.J., Frederick, C.O., "A mathematical representation of the multiaxial Bauschinger Effect", Report RD/B/N 731, Central Electricity Generating Board and Berkeley Nuclear Laboratories, Research & Development Dept., 1966.

[14] Voce, E., "A practical strain-hardening function", Metallurgica 51, 219–226, 1955

[15] Brepols, T., Vladimirov, I. N., and Reese, S., "Numerical comparison of isotropic hypo- and hyperelastic-based plasticity models with application to industrial forming processes", International Journal of Plasticity, 63, 18–48, 2014.

[16] Xiao, H., Bruhns, O. and Meyers, A., "Elastoplasticity beyond small deformations", Acta Mechanica, 182, 31-111, 2006.

[17] Chatti, S. "Effect of the elasticity formulation in finite strain on springback prediction", Computers & Structures, 88, 796–805, 2010.

[18] Jaumann, G., "Geschlossenes system physikalischer und chemischer differentialgesetze", Elektromagnetische Theorie, 386, 1908.

[19] Green, A. E. and Naghdi, P. M. "A General theory of elastic-plastic continuum", Archive for Rational Mechanics and Analysis, 18, 251–281, 1965.

[20] Bruhns, O. T., Xiao, H. and Meyers, A., "Self-consistent Eulerian rate type elasto-plasticity models based upon the logarithmic stress rate", International Journal of Plasticity, 15, 479–520, 1999.

[21] Careglio, C., Canales, C., Garino, C. G., Mirasso, A., and Ponthot, J. P., "A numerical study of hypoelastic and hyperelastic large strain viscoplastic Perzyna type models", Acta Mechanica, 227, 3177–3190, 2016.

[22] Ponthot, J.P., "Unified stress update algorithms for the numerical simulation of large deformation elasto-plastic and elastoviscoplastic processes", Int. J. Plast., 18, 91–126, 2002.

[23] García Garino, C., Ribero Vairo, M.S., Andía Fagés, S., Mirasso, A.E., Ponthot, J.P., "Numerical simulation of finite strain viscoplastic problems", J. Comput. Appl. Math., 246, 174–184, 2013

[24] Vladimirov, I. N., Pietryga, M., and Reese, S., "Prediction of springback in sheet forming by a new finite strain model with nonlinear kinematic and isotropic hardening", Journal of Materials Processing Technology, 209, 4062–4075, 2009.

[25] Vladimirov, I. N., Pietryga, M. P. and Reese, S., "On the modelling of non-linear kinematic hardening at finite strains with application to springback—

Comparison of time integration algorithms", International Journal for Numerical Methods in Engineering, 75, 1–28, 2008.

[26] Simo, J. and Miehe, C., "Associative coupled thermoplasticity at finite strains: Formulation, numerical analysis and implementation", Computer Methods in Applied Mechanics and Engineering, 98, 41–104, 1992.

[27] Simo, J., Hughes T. J. R., "Computational inelasticity", Interdisciplinary Applied Mathematics, 7, 1998.

[28] Hartmann, S., Lührs, G., and Haupt, P., "An efficient stress algorithm with applications in viscoplasticity and plasticity", International Journal for Numerical Methods in Engineering, 40, 991–1013, 1997.

[29] Vladimirov, I. N., Pietryga, M. P., Kiliclar, Y., Tini, V., and Reese, S., "Failure modelling in metal forming by means of an anisotropic hyperelastic-plasticity model with damage", International Journal of Damage Mechanics, 23, 1096–1132, 2014.

[30] Nakazima, K., Kikuma, T., and Hasuka, K., Yawata Technology Report 264: 8517–8530, 1968.

[31] Wallin, M., and Ristinmaa, M., "Deformation gradient based kinematic hardening model", International Journal of Plasticity, 21, 2025–2050, 2005.

[32] Sanz, M. A., Nguyen, K., Latorre, M., Rodríguez, M., and Montáns, F. J., "Sheet metal forming analysis using a large strain anisotropic multiplicative plasticity formulation, based on elastic correctors, which preserves the structure of the infinitesimal theory", Finite Elements in Analysis and Design, 164, 1–17, 2019.

[33] Zhang, M., and Montáns, F. J., "A simple formulation for large-strain cyclic hyperelasto-plasticity using elastic correctors. Theory and algorithmic implementation", International Journal of Plasticity, 113, 185–217, 2019.

[34] Truesdell, C. and Noll, W., "The non-linear field theories of mechanics", Berlin: Springer, 2010.

[35] Truesdell, C., "The simplest rate theory of pure elasticity", Communications on Pure and Applied Mathematics, 8, 123–132, 1955.

[36] Khan, A. S., and Huang, S., Continuum theory of plasticity, Estados Unidos: John Wiley & Sons, 1995.

[37] Bonet, J., and Wood, R. D., Nonlinear Continuum Mechanics for Finite Element Analysis, 2nd ed. New York: Cambridge University Press, 2008.

[38] L. L. C. Engineers Edge, "Von Mises Criterion (Maximum Distortion Energy Criterion) - Strength (Mechanics) of Materials", Engineers Edge. [Online].

Available: https://www.engineersedge.com/material_science/von_mises.htm., Accessed: 30-Apr-2019

[39] Bertarelli, A., “Beam-induced damage mechanisms and their calculation”, CERN in the Proceeding of the Joint International, 5–14, 2014.

[40] Lehmann, T., “Some remarks on the decomposition of deformations and mechanical work”, International Journal of Engineering Science, 20, 281–288, 1982.

[41] Kelly, P., Solid mechanics part I: An introduction to solid mechanics. Solid mechanics lecture notes, University of Auckland, 2013.

[42] “Abaqus 2016 Theory Manual”, Dassault Systemes Simulia Corporation, 2016.

[43] Lee, E. H., “Elastic-Plastic Deformation at Finite Strains”, Journal of Applied Mechanics, 1969.

[44] Lion, A., “Constitutive modelling in finite thermoviscoplasticity: a physical approach based on nonlinear rheological models”, International Journal of Plasticity, 16, 469–494, 2000.

[45] Pepper, D. W. and Heinrich, J. C., The Finite Element Method, 3rd ed. Taylor & Francis Group, 2017.

[46] Koutromanos, I., Fundamentals of Finite Element Analysis: Linear Finite Element Analysis, John Wiley and Sons Ltd, 2018.

[47] Cogun, F. and Darendeliler, H., “Comparison of different yield criteria in various deep drawn cups”, International Journal of Material Forming, 10, 85–98, 2015.

APPENDICES

A. NEWTON RAPHSON METHOD

A system of n number of nonlinear equations $(f_1, f_2, f_3 \dots f_n)$ which have n number of unknowns $(x_1, x_2, x_3 \dots x_n)$ can be solved using Newton Raphson method

$$f(x_1, x_2, x_3 \dots x_n) = \begin{bmatrix} f_1(x_1, x_2, \ldots, x_n) = 0 \\ f_2(x_1, x_2, \ldots, x_n) = 0 \\ \vdots \\ f_n(x_1, x_2, \ldots, x_n) = 0 \end{bmatrix} \tag{A.1}$$

Defining Jacobian of the system as:

$$J(x_1, x_2, x_3 \dots x_n) = \begin{bmatrix} \frac{\partial f_1}{\partial x_1} & \frac{\partial f_1}{\partial x_2} & \cdots & \frac{\partial f_1}{\partial x_n} \\ \frac{\partial f_2}{\partial x_1} & \frac{\partial f_2}{\partial x_2} & \cdots & \frac{\partial f_2}{\partial x_n} \\ \vdots & \vdots & \ddots & \vdots \\ \frac{\partial f_n}{\partial x_1} & \frac{\partial f_n}{\partial x_2} & \cdots & \frac{\partial f_n}{\partial x_n} \end{bmatrix} \tag{A.2}$$

Let y_0 be initial set of guesses for the solution then improved set of guesses for solution y_1 can be found using:

$$y_1 = y_0 - \left(J(y_1, y_2, y_3 \dots y_n)\right)^{-1} f(y_1, y_2, y_3 \dots y_n) \tag{A.3}$$

Solution can be found through this equation in an iterative manner to reach a desired precision.